PHOTON LIMITED IMAGE PROCESSING IN THE SPACE-TIME DOMAIN

Final Technical Report

January 1988

United States Army
European Research Office of the US Army
London England

Contract Number DAJA-45-85-C-0028

Blackett Laboratory, Imperial College
London SW7 2BZ

PHOTON LIMITED IMAGE PROCESSING IN THE SPACE-TIME DOMAIN

Final Technical Report

January 1988

United States Army
European Research Office of the US Army
London England

Contract Number DAJA-45-85-C-0028

Blackett Laboratory, Imperial College
London SW7 2BZ

Approved for Public Release; distribution unlimited

REPRODUCTION QUALITY NOTICE

This document is the best quality available. The copy furnished to DTIC contained pages that may have the following quality problems:

- Pages smaller or larger than normal.
- Pages with background color or light colored printing.
- Pages with small type or poor printing; and or
- Pages with continuous tone material or color photographs.

Due to various output media available these conditions may or may not cause poor legibility in the microfiche or hardcopy output you receive.

☑ If this block is checked, the copy furnished to DTIC contained pages with color printing, that when reproduced in Black and White, may change detail of the original copy.

SECURITY CLASSIFICATION OF THIS PAGE

REPORT DOCUMENTATION PAGE

Form Approved OMB No. 0704-0188 Exp. Date: Jun 30, 1986

1a. REPORT SECURITY CLASSIFICATION: Unclassified	1b. RESTRICTIVE MARKINGS
2a. SECURITY CLASSIFICATION AUTHORITY	3. DISTRIBUTION/AVAILABILITY OF REPORT: Approved for public release; distribution unlimited
2b. DECLASSIFICATION/DOWNGRADING SCHEDULE	
4. PERFORMING ORGANIZATION REPORT NUMBER(S)	5. MONITORING ORGANIZATION REPORT NUMBER(S): R&D 4611-PH-01
6a. NAME OF PERFORMING ORGANIZATION: Blackett Laboratory, Imperial College; 6b. OFFICE SYMBOL (If applicable)	7a. NAME OF MONITORING ORGANIZATION: USARDSG-UK
6c. ADDRESS (City, State, and ZIP Code): London, SW7 2BZ, England	7b. ADDRESS (City, State, and ZIP Code): Box 65, FPO NY 09510-1500
8a. NAME OF FUNDING/SPONSORING ORGANIZATION: USARDSG-UK ARO-E; 8b. OFFICE SYMBOL (If applicable)	9. PROCUREMENT INSTRUMENT IDENTIFICATION NUMBER: DAJA45-85-C-0028
8c. ADDRESS (City, State, and ZIP Code): Box 65, FPO NY 09510-1500	10. SOURCE OF FUNDING NUMBERS: PROGRAM ELEMENT NO. 61102A; PROJECT NO. 1L161102BH57; TASK NO. 07; WORK UNIT ACCESSION NO

11. TITLE (Include Security Classification)

(U)Photon Image Processing In The Space-Time Domain

12. PERSONAL AUTHOR(S)

Professor J.C. Dainty

13a. TYPE OF REPORT	13b. TIME COVERED	14. DATE OF REPORT (Year, Month, Day)	15. PAGE COUNT
Final	FROM 85 TO 87	1988 January	135

16. SUPPLEMENTARY NOTATION

17. COSATI CODES: FIELD	GROUP	SUB-GROUP

18. SUBJECT TERMS (Continue on reverse if necessary and identify by block number)

(U) Triple Correlation; (U) Bispectrum; (U) Atmospheric Turbulence; (U) Image Processing; (U) Photon Correlation

19. ABSTRACT (Continue on reverse if necessary and identify by block number)

This report is principally concerned with the use of the triple correlation function and its Fourier transform, the bispectrum, for the imaging of randomly translating objects or objects viewed through atmospheric turbulence. The triple correlation has significant advantages over the second order correlation, although it does involve additional computational complexity. Specific consideration is given to algorithms for computing the triple correlation, the use of a moving time window and centroiding procedures.

The Appendix contains copies of the 9 publications that resulted from this research.

20. DISTRIBUTION/AVAILABILITY OF ABSTRACT	21. ABSTRACT SECURITY CLASSIFICATION
☒ UNCLASSIFIED/UNLIMITED ☒ SAME AS RPT ☒ DTIC USERS	Unclassified
22a. NAME OF RESPONSIBLE INDIVIDUAL: Dr. Gerald R. Andersen	22b. TELEPHONE (Include Area Code): 01-409 4423; 22c. OFFICE SYMBOL: AMXSN-UK-RP

DD FORM 1473, 84 MAR — 83 APR edition may be used until exhausted. All other editions are obsolete.

SECURITY CLASSIFICATION OF THIS PAGE

SUMMARY

This report is principally concerned with the use of the triple correlation function and its Fourier transform, the bispectrum, for the imaging of randomly translating objects or objects viewed through atmospheric turbulence. The triple correlation has significant advantages over the second order correlation, although it does involve additional computational complexity. Specific consideration is given to algorithms for computing the triple correlation, the use of a moving time window and centroiding procedures. The Appendix contains the nine publications and conference papers that resulted from this research.

Keywords

Triple Correlation
Image Processing
Bispectrum
Photon Correlation
Atmospheric Turbulence

Contents

1 INTRODUCTION

This report describes the application of *triple correlation* signal processing techniques to photon-limited data. Such data will typically arise at low light levels associated with night time viewing, but it should be borne in mind that, as detectors get faster in their response, photon-limited data will also arise at high light levels (and very short exposures). The type of data we are considering is distorted in some way, either by random translations (as in a tracking system) or by atmospheric turbulence and thus simple long-exposure imaging is not applicable, as a blurred image would result.

The triple correlation $i^{(3)}(x_1,x_2)$ and its Fourier transform, the bispectrum $I^{(3)}(u_1,u_2)$, of a one-dimensional function $i(x)$ are definec by

$$i^{(3)}(x_1,x_2) = \int_{-\infty}^{\infty} i^*(x)\, i(x+x_1)\, i(x+x_2)\, dx \qquad (1)$$

and

$$I^{(3)}(u_1,u_2) = I(u_1)\, I(u_2)\, I^*(u_1+u_2), \qquad (2)$$

where $I(u)$ is the Fourier transform of $i(x)$. The triple correlation (and bispectrum) have a number of useful properties:

- they are invariant on translation (this is clear from the definitions above)
- they can be propagated through turbulence with little loss of information
- the original signal can be recovered uniquely from either function with no ambiguity.

The triple correlation and bispectrum have recently been re-discovered in optics by Lohmann's group in Erlangen[10-15] and this present study was motivated by their results. This report describes four aspects of the triple correlation

- application to randomly moving objects (§2)
- application to imaging through turbulence (§3)
- use of a moving time window to improve signal-to-noise ratio (§4)
- algorithms (§5).

In addition, we have investigated the use of centroiding for photon-limited imaging and demonstrated a new technique of imaging for randomly translating objects (§6).

The achievements on the above five topics are summarised in §2 to §6 on the following pages. References 1-9 are the publications resulting from this research and are reproduced in the Appendix. For further details on each topic, the references should be consulted.

2 TRIPLE CORRELATION OF RANDOMLY TRANSLATING OBJECTS

It is clear from Eq (1) that the triple correlation of a function i(x) is invariant on translation (random or otherwise) and thus the triple correlation of a randomly translating object is simply equal to that of the stationary object. Thus, provided one can recover i(x) from its average triple correlation, we have a simple way of imaging which is particularly relevant to optical systems involved in tracking[14].

We have applied this to both real and computer-simulated data in one and two dimensions[2-4]. Typical results for the one-dimensional case are shown in Figs 2 & 3 of Ref 3: for an object function consisting of 128 sample points, unambiguous imaging at photon levels as low as <4 detected photons per frame has been demonstrated using real data gathered by a resistive anode imaging photon detector (IPD). In this case the dark count was ≈0.5 detected photons per frame and ≈30,000 frames were required (this would represent a data collection time of ≈5 mins at 100 frames/s). Simple-minded centroiding does not work well at this photon level (but see §6 below). The presence of a uniform background in the one-dimensional case was also studied: signal-to-background ratios >1 did not significantly affect the reconstructed image quality.

The two-dimensional case was studied in Ref 4. For real photon data, a simple object consisting of ≈5x5 resolution cells and ≈2000 frames, a photon rate of ≈15 per frame was sufficient to give an adequate reconstruction (Fig 2 of Ref 4), although computer simulated data of the same object showed that under these conditions the reconstruction should be almost perfect. It is believed that imperfections in the IPD were responsible for the reduced quality in the real data case. For computed simulated data, a more complex object consisting of ≈8x15 resolution cells and ≈2000 frames, a photon rate of ≈15 per frame gave an excellent quality reconstruction, comparable to, and arguably better than, the original stationary object imaged with ≈30,000 photons.

The conclusion of this study was that the triple correlation is an extremely powerful technique for high resolution imaging of randomly translating objects at *very* low light levels ≈1-20 photons per frame. We are considering extensions of the technique to randomly rotated and/or scaled objects: some progress on this has been made by Lohmann[15] in the high light level case, but the practical feasibility in the photon limited case has not yet been explored.

3 TRIPLE CORRELATION IMAGING THROUGH TURBULENCE

Since the invention of stellar speckle interferometry by Labeyrie in 1970, a variety of techniques for speckle *imaging* have been suggested[16,17]. Of these, triple correlation imaging appears to provide the highest quality reconstructions. Our research has focussed on a detailed study of the signal-to-noise ratio of the photon-limited triple correlation (or bispectrum) and a comparison of the Knox-Thompson and triple correlation methods[5,7].

When imaging through turbulence, the average bispectrum of the image, $\langle I^{(3)}(u_1,u_2)\rangle$, is related to the object bispectrum $O^{(3)}(u_1,u_2)$ by

$$\langle I^{(3)}(u_1,u_2)\rangle = O^{(3)}(u_1,u_2)\ \langle P^{(3)}(u_1,u_2)\rangle\ , \qquad (3)$$

where $\langle P^{(3)}(u_1,u_2)\rangle$ is the average bispectrum of the atmosphere/telescope. The phase of $\langle P^{(3)}(u_1,u_2)\rangle$ is zero and thus the phase of the average image bispectrum (which is crucial for the reconstruction process) simply equals that of the object bispectrum.

Our calculations and computer simulations show that, although the whole atmospheric bispectrum contains diffraction-limited information, the only useful parts *in the photon limited case* are those for which $u_1 \approx u_2$. In this region, the signal-to-noise is dominated by power-spectrum-like terms, yielding an SNR $\propto$ n , the average number of photons per frame. The behaviour at intermediate and high light levels, and at other parts of the (u_1,u_2) space, is considerably more complex[7]. As a simple guide, fairly complicated objects with ≈8x15 resolution cells can be imaged with near-diffraction-limited resolution at a level of ≈200 detected photons per frame and ≈20,000 frames, in good seeing (≈1 ").

A comparison of the Knox-Thompson and triple correlation techniques has shown them to be remarkably similar, provided each method is implemented in the optimum way. The triple correlation method is always superior to the Knox-Thompson method because centroiding is allowed for *exactly* in the triple correlation, whereas it is only approximately corrected for in the K-T algorithm. The triple correlation does not involve any more complicated or time-consuming processing than the K-T method - both are equally computer-intensive.

4 USE OF A MOVING TIME WINDOW

Historically, spatio-temporal imaging and image processing has used *frames* of data, with the implicit assumption that the exposure time of each frame is sufficiently short to "freeze" any motion within the scene. When dealing with photon-limited data of a dynamic nature, the concept of data frames becomes less useful and a more valuable approach is to consider the data as a set of space-time {x,y,t} coordinates of photon events. A time "frame" may then move through this data set *continuously* and the window itself may be of variable length.

As a first step in this direction, we have evaluated the improvement in the signal-to-noise ratio of an Nth-order correlation when a continuously moving, but fixed width, time window is used, compared to the normal discrete frame window of the same length[8]. The detailed argument is given in Appendix A of Ref 8. To illustrate the method, consider the photons to arrive at a uniform rate of N per time window and evaluate the number of independent photon difference vectors possible in the estimation of the autocorrelation function (2nd order correlation). When the window moves discretely to its next position, the total number of new difference vectors is N(N-1)/2 (forward and reverse vectors are redundant). Moving the window continuously we pick up (N-1) new differences for every new photon included in the window, thus accumulating a total of N(N-1) new differences in all. In this case, there is thus an increase in the SNR of $\sqrt{2}$ compared to the discrete case. For the Nth-order correlation, the improvement is $\approx \sqrt[N]{N}$.

The concept of treating the image information as a set of photon coordinates is a very important one. We propose to extend triple correlation analysis to the space-time domain using this approach. For example, the length of the time window may be different for different spatial frequencies, reflecting the knowledge that, in many cases, higher spatial frequencies decorrelate more quickly in time than lower frequencies.

5 ALGORITHMS

Calculation of the complete triple correlation or bispectrum is computationally intensive and requires a large computer memory. For example, a 512x512 image has a bispectrum consisting of $(512)^4$ elements, each element being the product of three Fourier transforms. For applications such as real-time imaging through turbulence, one may wish to calculate and average ≈100 bispectra per second.

We have implemented three algorithms for computing the bispectrum of two-dimensional photon-limited data. Although all three give similar results and have similar computational complexity[8], algorithm (iii) (below) is preferred, as it enables the moving time window concept described in §4 to be implemented efficiently. In all three algorithms, only a fraction of the total bispectrum is computed, either that close to the axes as in (i) and (iii), or using a limited number of sections as in (ii).

Algorithm (i) involves direct implementation of Eq(2) and is thus not limited to photon-limited data. A key step in this algorithm (and (iii)) is deciding what bispectrum locations to compute: this is based on considerations of signal-to-noise ratio. Algorithm (ii) uses the Radon transform or projection-slice theorem of Fourier transforms: the two dimensional data is projected onto a series of one dimensional vectors (36 in our case[8]) and for each vector the average triple correlation or bispectrum is calculated. The corresponding slice in the object spectrum is found from each bispectrum and the (36) slices are combined to form the object spectrum and the object map, as in computed tomography. This approach may be suited to highly parallel processors. Algorithm (iii) uses a photon differencing approach to calculate only those parts of the bispectrum that are necessary for the reconstruction and is similar to the photon differencing implementation of the Knox-Thompson algorithm.

All three algorithms have a similar computing time on our hardware (SUN 3/160 with Sky 'Warrior' array processor, purchased under this Contract), ≈12 s per frame of 128x128 pixels at ≈200 photons per frame (algorithm (i) uses the array processor, (ii) and (iii) do not). The algorithms are programmed in 'C' and could probably be improved in speed by a factor of up to 2.

6 CENTROIDING OF RANDOMLY MOVING OBJECTS

During the study of triple correlation imaging of randomly moving objects, a comparison was made with centroided photon coordinate data[3]. The simplest type of centroid is that of the photon coordinates of each frame, without regard to the number of photons in each frame: this is not very useful, as the results reported in Ref 3 show. We have studied another type of centroid, that of the N-photon image. To compute this, the data is divided into sets, each set containing only those images with exactly N detected photons. A centroided 'image' is found *for each set* and, denoting its spectrum by $Q_N(u)$, we have shown that[6,9]

$$Q_N(u) = I(u[1-1/N])\,[I^*(u/N)]^{N-1} \qquad (4)$$

where I(u) is the spectrum of the original object. Note that the spectrum of the N-photon centroided 'image' is non-linearly related to that of the original object. For example, if N = 2, $Q_N(u)$ is equal to the *power spectrum* of the object, and if N = 3, it is equal to a particular section of the bispectrum.

A high quality reconstruction of the original can be found by combining all of the $Q_N(u)$ using a recursive algorithm[6,9]. Using computer-simulated one-dimensional data, we have reconstructed a two-point object at an average photon level of ≈3 photons per frame and ≈80,000 frames (see Fig 3 of Ref 6). The algorithm has the interesting property that to reconstruct the *n*th discrete spatial frequency, one requires an image with at least *n* detected photons. This method is currently being studied for the application of imaging through turbulence. It has the advantage that it is extremely fast to compute.

7 CONCLUSIONS

This research has demonstrated the potential usefulness of the triple correlation and its Fourier transform, the bispectrum, in the analysis of photon-limited images. The invariance of the triple correlation upon translation or propagation through turbulence, coupled with the fact that a signal can be reconstructed uniquely from its triple correlation, make it a powerful tool for imaging in unfavourable circumstances.

We have demostrated the application of the triple correlation to the imaging of a randomly translating object and objects viewed through atmospheric turbulence. In both cases, diffraction-limited imaging is possible at very low photon rates, <10 per frame for certain cases of random translation and ≈200 per frame for typical situations of imaging through turbulence. The signal-to-noise ratio of the triple correlation has been evaluated in detail and three algorithms for computing the bispectrum have been written and compared. A photon-differencing algorithm is perferred as use can be made of a moving time window, yielding a higher signal-to-noise ratio.

Centroiding has been studied as a means of diffraction-limited imaging of randomly translating objects and a new algorithm for object reconstruction based on centroiding has been developed.

8 REFERENCES

1 J C Dainty et al, "Photon correlation experiments on dynamic speckle using a multipoint detector", Proceedings of the 6th International Conference on Photon Correlation and Other Optical Techniques in Fluid Mechanics, July 10-12, 1985, Cambridge, England.

2 J C Dainty and M J Northcott, "Imaging a randomly translating object using the triple correlation", Technical Digest of the OSA Topical Meeting on Quantum Limited Imaging and Image Processing, March 31-April 2, 1986, Hawaii, USA.

3 J C Dainty and M J Northcott, "Imaging a randomly translating object at low light levels using the triple correlation", Opt Commun, **58**, 11-14 (1986)

4 G R Ayers, J C Dainty and M J Northcott, "Photon limited imaging through turbulence", Proc SPIE, **808**, 19-25 (1987)

5 J C Dainty, "Speckle imaging techniques", Proc SPIE, **828**, paper 1 (in press, 1987)

6 L C de Freitas, M J Northcott, B J Brames and J C Dainty, "Object reconstruction from photon-limited centroided data of randomly translating images", Proc SPIE, **828**, paper 9 (in press, 1987)

7 G R Ayers, M J Northcott and J C Dainty, "Knox-Thompson and triple correlation imaging through atmospheric turbulence", JOSA A (accepted for publication)

8 M J Northcott, G R Ayers and J C Dainty, "Algorithms for image reconstruction from photon-limited data using the triple correlation", submitted to JOSA A.

9 L C de Freitas and J C Dainty, "Object reconstruction from photon-limited centroided data of randomly translating images", submitted to Opt Lett.

10 A W Lohmann, G Weigelt and B Wirnitzer, "Speckle masking in astronomy: triple correlation theory and applications", Appl Opt, **22**, 4028-4037 (1983)

11 A W Lohmann and B Wirnitzer, "Triple correlations", Proc IEEE, **72**, 889-901 (1984)

12 H Bartelt, A W Lohmann and B Wirnitzer, "Phase and amplitude recovery from bispectra", Appl Opt, **23**, 3121-3129 (1984)

13 B Wirnitzer, "Bispectral analysis at low light levels and astronomical speckle masking", JOSA A, **2**, 14-21 (1985)

14 H Bartelt and B Wirnitzer, "Shift-invariant imaging of photon-limited data using bispectral analysis", Opt Commun, **53**, 13-16 (1985)

15 A W Lohmann, Optik, **73**, 127-131 (1986)

16 J C Dainty, "Stellar speckle interferometry", in *Laser Speckle and Related Phenomena*, Edited by J C Dainty, Springer-Verlag, 2nd Ed, 1984

17 J C Dainty and J R Fienup, "Phase retrieval and image reconstruction for astronomy", in *Image Recovery: Theory and Application*, Edited by H Stark, Academic Press, 1987

9 APPENDIX

References 1 to 9 are reproduced on the following pages.

Paper presented at VI Int. Conf. Photon Correlation and Other Techniques in Fluid Mechanics

Photon correlation experiments on dynamic speckle using a multipoint detector

J C Dainty, D Newman, M J Northcott and K A O'Donnell

Blackett Laboratory, Imperial College, London SW7 2BZ, UK.

Abstract. An imaging photon detector has been used to measure the spatio-temporal correlation function of dynamic speckle simultaneously at many spatial and temporal lags.

1. Introduction.

Photon correlation experiments usually involve measurements at either one or two points in space. Temporal correlation at a single point yields dynamic time scales of processes and can give velocities if a reference beam or other coding scheme (eg a grating) is used. Temporal cross-correlation at two points in space yields time-of-flight and hence velocity information. However, for a complete description of the second order correlation properties of the intensity of a scattering pattern or image, we need to know the spatio-temporal correlation function (ie the temporal cross-correlation for all possible pairs of spatial lags).

2. Imaging Photon Detector.

One possible way of measuring the spatio-temporal correlation would be to use an array of photomultipliers, say 100 x 100, with a vast number (many thousands) of conventional correlator channels. Such a device would have a similar signal-to-noise ratio to that of the current one- and two-channel systems, but would be prohibitively expensive at present. Another way is to use a two-dimensional image intensifier, such as a microchannel plate device, together with a means of photon position readout, and use the photon coordinates (x,y,t) to compute the space-time correlation by means of a histogram of coordinate differences.

Two detectors based on the latter principle are commercially available at the moment. The Imaging Photon Detector (IPD) [1-3] uses a resistive anode for the position readout and is the device used in this work. In the Precision Analog Photon Address (PAPA) detector [4], a set of binary masks and photomultipliers provide the photon coordinates. Both the IPD and PAPA use a microchannel plate as the primary detector. The limiting factor of both detectors as far as photon correlation is concerned is the long deadtime which limits the maximum permissable photon rate and, ultimately, the signal-to-noise ratio.

In the configuration used in our experiments, the IPD digitises the x and y coordinates with a resolution of 256 x 256 corresponding to a

pixel size of 70 x 70 μm. An electronic module adds the time coordinate of detected events and sends the (x,y,t) coordinates as a 32-bit word to a Hewlett Packard 9836 desktop computer. In a typical experiment, the photon rate is approximately 10^4 per second over the whole image area.

3. Calculation of the Correlation Function.

A photon coordinate differencing algorithm, similar to that in routine use in stellar speckle interferometry [5], is carried out in near real-time by the HP 9836. The correlation $C(\Delta x,\Delta y,\tau)$ is simply equal to the histogram of coordinate differences,

$$C(\Delta x,\Delta y,\tau) = \sum_{i=0}^{max} \sum_{j=0}^{i} \delta(X_i-X_j-\Delta x)\,\delta(Y_i-Y_j-\Delta y)\,\delta(T_i-T_j-\tau)$$

where X_i, Y_i and T_i are the coordinates of the ith detected photon. Correction has to be made for the triangular correlation window due to the finite spatial size of the detector, and for dark count (approx. 200 per second at room temperature). An analysis of the effect of detector deadtime [6] gives the unusual result that, to first order, the scale value of the correlation (variance) is not influenced by the deadtime provided that the baseline of the correlation is used for normalisation.

4. Measurements of Dynamic Speckle.

In order to demonstrate the potential, and limitations, of the IPD for space-time photon correlation, we have carried out a simple measurement on dynamic speckle from a rotating diffuser [7]. The experimental arrangement is shown in Figure 1. The IPD is in the far-field of the illuminated area. The speckle pattern is the x,y plane of the IPD

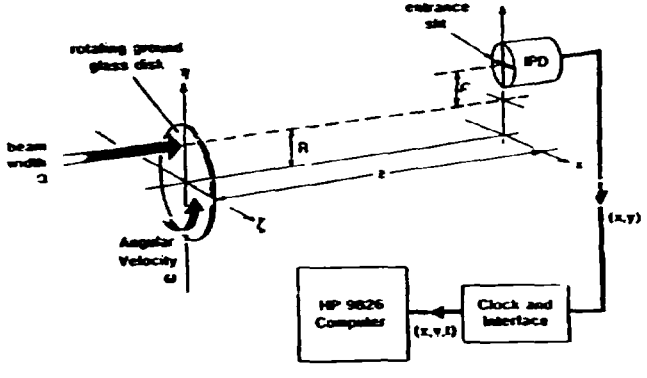

Figure 1

appears to rotate about the rotation axis of the diffuser and simultaneously evolves in a random manner: the detector, which covers only a few speckle correlation areas, therefore sees translating and boiling speckle. The space-time intensity correlation is evaluated in detail in references [7] and [8].

Because of the limitations of the graphics devices at our disposal, the measurements were only for $\Delta x - \tau$ correlations. The increments of Δx and τ were 70 μm and 12.8 ms respectively. Approximately 5×10^4 photon coordinates were recorded over a few seconds and the correlation calculated for Δx from +90 to -90 lags and τ from 0 to 9 lags: the calculation took a few minutes when machine-coded on the HP 9836.

The results of this measurement are shown in Figure 2(a)-(b). Each curve shows the spatial correlation for different time lags of 0 (a) to 7 (b) and is corrected for the systematic bias due to the finite spatial window. Figure 2(a) is the spatial intensity correlation function of the dynamic speckle. It is well known that this equals the squared modulus of the Fourier transform of the intensity of the illumination spot on the diffuser [9] and our measurement agrees with the theoretical prediction. (The normalised contrast is less than unity because of spatial integration effects in the y-direction.)

Curves 2(b)-(h) show the spatio-temporal evolution of the dynamic speckle. The peak of the curve moves to the left indicating that the speckle is translating in that direction: the decreasing height of the peak indicates that the speckle is also boiling or evolving. Both characteristics agree quantitatively with theory [7]. The complete set of curves were obtained from only 5×10^4 detected photons and the total number of correlation lags was approximately 1800 (180 in Δx and 10 in τ).

5. Limitation of the Present Equipment.

The space-time correlation system described above has two main limitations. First, the deadtime of the detector, $\sim 10^{-5}$ s, limits the photon rate, which means that (i) only relatively slow phenomena can be studied (timescales of milliseconds) and (ii) only a restricted number of correlation lags (a few hundred) can be measured with a reasonable signal-to-noise ratio. This number is, of course, an enormous improvement on the conventional two-photomultiplier technique. The PAPA detector has a deadtime of approximately 1/10th that of the IPD and is probably more suitable for this kind of study. Multichannel photomultipliers [9] may also have better deadtime characteristics.

The second limitation of the existing equipment is its slow computation speed. Data gathered over a few seconds takes a few minutes to analyse, even though the time-critical part of the calculation is machine-coded. We propose to construct a hard-wired correlator to do this calculation in real time for the present IPD photon rate. Using CMOS technology it should be possible to calculate a single vector coordinate difference (a single contribution to the histogram) in approximately 50 ns.

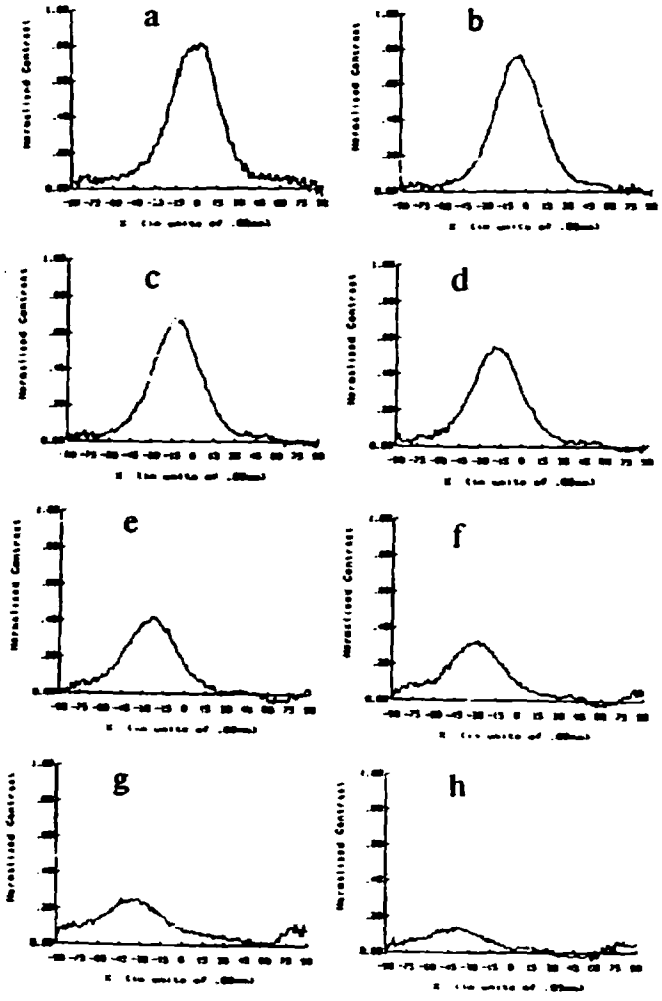

Figure 2

6. Triple Correlations.

Recently, Lohmann and collaborators [10-12] have demonstrated the power of the spatial triple correlation for imaging through turbulence and for the imaging of randomly moving objects. The triple correlation of an intensity distribution I(g) is defined by

$$C(\Delta x_1, \Delta x_2) = \int_{-\infty}^{\infty} I(g)\, I(g+\Delta x_1)\, I(g+\Delta x_2)\, dg \quad .$$

It can be implemented using a photon coordinate differencing algorithm with the IPD. The real-time correlator described in Section 5 will be able to compute the triple correlation online for image sizes of 25 x 25 provided that the photon rate is less than 65 per 10 ms time-window. This should be adequate for stellar imaging.

Acknowledgements

We are grateful to Dr A A D Camus for assistance with the electronics. This work was supported by the UK Science Research Council and the US Army European Research Office.

References

1 D Rees et al. J Phys E, 14, 229-233 (1981)

2 C Firmani et al. Rev Sci Instr, 53, 570-574 (1982)

3 The IPD is manufactured by Instrument Technology Ltd, 29 Castlehaz Rd, St Leonards-on-Sea, East Sussex, TN38 9NS, UK.

4 C Papaliolios, P Nisenson and S Ebstein, Appl Opt, 24, 287-292 (1985)

5 P R Vokac, Proc SPIE, 119, 223-231 (1977)

6 K A O'Donnell and D Newman, in preparation

7 D Newman, A A D Camus and J C Dainty, Appl Opt (in press)

8 J H Churnside, J Opt Soc Am, 72, 1464-1469 (1982)

9 K Oba et al, IEEE Trans Nucl Sci, NS-26, 346-355 (1979)

10 A W Lohmann and B Wirnitzer, Proc IEEE, 72, 889-901 (1984)

11 H Bartelt, A W Lohmann and B Wirnitzer, Appl Opt, 23, 3121-3129 (1984)

12 H Bartelt and B Wirnitzer, Opt Commun, 53, 13-17 (1985)

TOPICAL MEETING ON

QUANTUM-LIMITED IMAGING & IMAGE PROCESSING

TECHNICAL DIGEST

SPRING '86
MARCH 31-APRIL 2, 1986
HONOLULU, HAWAII

IMAGING A RANDOMLY TRANSLATING OBJECT USING THE TRIPLE CORRELATION

J C Dainty and M J Northcott
Blackett Laboratory,
Imperial College,
London SW7 2BZ, UK.

Introduction

The triple correlation function $I^{(3)}(x_1, x_2)$ and its Fourier transform, the bispectrum $\tilde{I}^{(3)}(u_1, u_2)$, of a one dimensional intensity distribution $I(x)$ are defined by [1],

$$I^{(3)}(x_1, x_2) = \int_{-\infty}^{\infty} I(x)\, I(x+x_1)\, I(x+x_2)\, dx \qquad (1)$$

and

$$\tilde{I}^{(3)}(u_1, u_2) = \tilde{I}(u_1)\, \tilde{I}(u_2)\, \tilde{I}(-u_1-u_2) \quad . \qquad (2)$$

where $\tilde{I}(u)$ is the Fourier transform of $I(x)$. Lohmann and Wirnitzer [1] have shown that it is possible to recover a signal $I(x)$ from its triple correlation or bispectrum. The recovered signal is unique except in certain cases of no practical significance in the present study.

It is clear from Eqs.(1) and (2) that the triple correlation and bispectrum are invariant with object displacement and Bartelt and Wirnitzer [2] demonstrated, in a computer simulation, that a sharp reconstruction of a randomly moving object on a dark background could be obtained at very low light levels using the triple correlation. In this paper we present a practical demonstration of this using photons recorded by an Imaging Photon Detector (IPD) [3] and have included a uniform background in some of the experiments.

Experiments and Results

Random displacement of a one dimensional object was achieved by viewing the object reflected off a mirror attached to a randomly driven loadspeaker coil. The IPD was masked by a preslit in the one dimensional experiments and photon events were digitised into an array I_j, $j = 0,1,...127$ during each time window (frame) of length approximately 6 ms. The average detected photon rates in the experiments were in the range 1-40 per frame or 150-6000 s^{-1}. The lower rates were comparable to the dark count rate (~75 s^{-1}) and the highest rates were probably influenced by the dead-time effects that occur with this kind of detector.

In a typical run, 2×10^4 - 5×10^4 photon coordinates were recorded in 10^3 - 10^4 frames and stored on disc. An HP 9836 computer was programmed to calculate the triple correlation of the photon events using a machine-coded coordinate differencing algorithm, which could calculate the triple correlation at a rate of 100 s^{-1} for an average of 10 detected photons per frame.

A long exposure image (~5×10^4 photons) of the stationary object (a double slit) is shown in Fig. 1(a). With the object moving randomly in the frame, a long exposure produces the extremely blurred result shown in Fig. 1(b). Centroiding of each frame prior to averaging ('shift-and-add') gives an improved result, as shown in Figs. 1(c), (d) and (e) for average photon rates of 7.6, 4.4 and 1.1 per frame respectively, but the presence of the second slit is only apparent at the highest photon rates and even then is highly distorted. Using the triple correlation method following the reconstruction algorithm of Bartelt et al [4] (which uses one complete octant of the bispectrum), the reconstructions shown in Figs. 1(f), (g) and (h) are obtained. Note that both slits are clearly distinguishable in all cases. In the case of Fig. 1(h), the average detected photon rate of 1.1 per frame (of which 0.5 is dark count) meant that only 7% of frames contained the necessary 3 or more photons for evaluation of the triple correlation and the reconstruction was obtained using only 2089 usable frames.

Figure 2 shows the effect of a uniform background superimposed upon the double slit image, for background to signal ratios of approximately 1:1 (column 1) and 6:1 (column 2) and a signal rate of approximately 4.4 photons s^{-1}. Figures 2(e) and (f) show the reconstruction obtained using a single line of the bispectrum, whereas 2(g) and (h) are found from a complete octant. Satisfactory reconstruction is obtained when the background rate does not substantially exceed the signal rate.

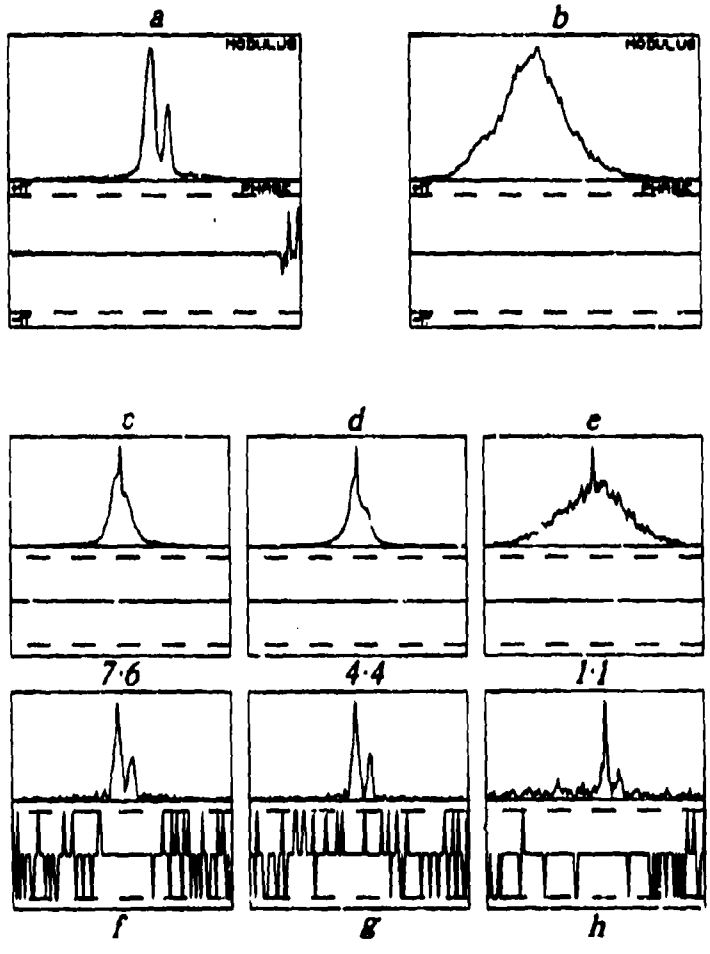

Figure 1

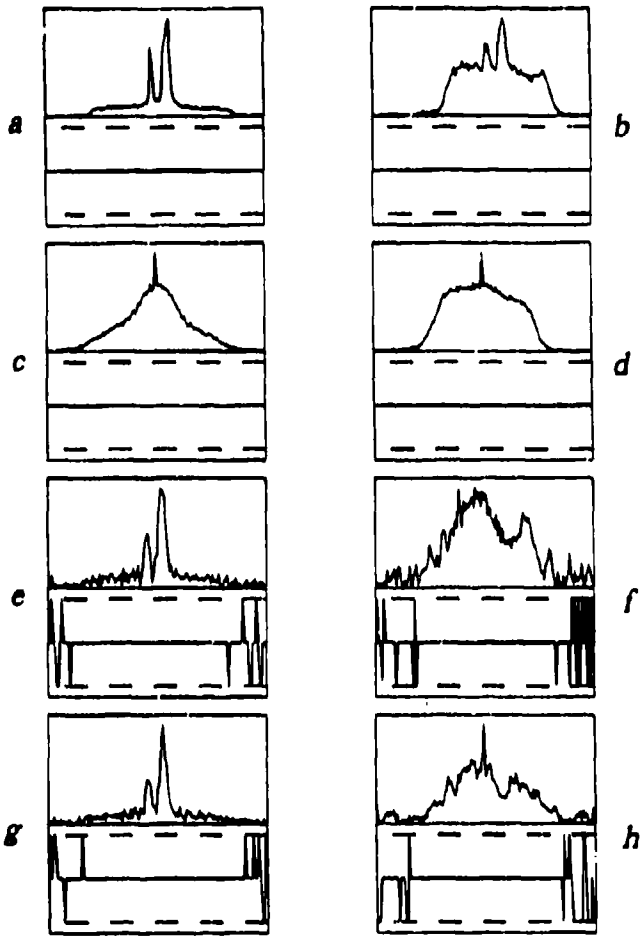

Figure 2

Acknowledgements This work is supported by grants from the UK SERC (GR/C 78940) and the US Army (DAJA45-85-C-0028).

References

1. A W Lohmann, Proc. IEEE, 72, 889-901 (1984).
2. H Bartelt and B Wirnitzer, Opt. Commun., 51, 13-17 (1985).
3. D Rees et al, J Phys. E, 13, 765-770 (1980).
4. H Bartelt et al, Appl. Opt., 23, 3121-3129 (1984).

REF 3

Volume 58, number 1 OPTICS COMMUNICATIONS 1 May 1986

IMAGING A FANDOMLY TRANSLATING OBJECT AT LOW LIGHT LEVELS USING THE TRIPLE CORRELATION

J.C. DAINTY and M.J. NORTHCOTT

Blackett Laboratory, Imperial College, London SW7 2BZ, UK

Received 6 January 1986

An imaging photon detector has been used to reconstruct an image of a randomly translating one-dimensional object at average photon rates of less than one signal photon per frame. The method used relies on the shift-invariance and Fourier-phase preserving properties of the triple correlation function.

1. Introduction

The triple correlation function $I^{(3)}(x_1, x_2)$ and its Fourier transform, the bispectrum $\mathcal{T}^{(3)}(u_1, u_2)$, of a one-dimensional intensity distribution $I(x)$ are defined by [1],

$$I^{(3)}(x_1, x_2) = \int_{-\infty}^{\infty} I(x) I(x + x_1) I(x + x_2)\, dx, \qquad (1)$$

and

$$\mathcal{T}^{(3)}(u_1, u_2) = \mathcal{T}(u_1)\mathcal{T}(u_2)\mathcal{T}(-u_1 - u_2), \qquad (2)$$

where $\mathcal{T}(u)$ in the Fourier transform of $I(x)$. It has been shown [1–3] that a signal $I(x)$ can be recovered from its triple correlation or bispectrum and that the recovered signal is unique except for certain cases of no practical significance in the present study.

It is clear from eqs. (1) and (2) that the triple correlation and bispectrum are invariant with object displacement. Bartelt and Wirnitzer [4] demonstrated, in a computer simulation, that a sharp reconstruction of a randomly shifted object on a dark background could be obtained at very low light levels using the bispectrum. In this paper we present a practical demonstration of this using photons recorded by an Imaging Photon Detector (IPD) [5] and have included a uniform background in some of the experiments.

2. Method

A large number (typically 3×10^6) of frames of a randomly translating object were recorded and their average triple correlation computed using photon differencing algorithm. The average bispectrum was found from the average triple correlation by Fourier transformation and an estimate of the modulus and phase of the object spectrum was extracted from the average bispectrum. Finally an inverse Fourier transform yielded an estimate of the original object.

Random displacement of the one dimensional object was achieved by viewing it reflected off a mirror attached to a randomly driven loudspeaker coil. The IPD is a microchannel plate/resistive anode device [5] with 256×256 pixel coordinates, which in this experiment was masked by a pinhole and software so that the photon events were digitised into a one-dimensional array D_I, $I = 0, 1, \ldots, 127$ during each time-window (frame) of approximately 6 ms duration. The average dark count rate corresponded to 0.5 detected photons per frame.

In a typical run, 3×10^6 frames are recorded and stored on disc. An HP 9836 computer was programmed to calculate the triple correlation using a machine-coded coordinate differencing algorithm. It is straightforward to show [6,7] that a histogram of vector differences of photon coordinates exactly equals the required average triple correlation $\langle D^{(3)}_{lm} \rangle$ of the data. The average bispectrum $\langle \bar{D}^{(3)}_{jk} \rangle$ of the data is formal-

0 030-4018/86/$03.50

ly related to that of the sampled intensity, $\langle \tilde{I}^{(3)}_{jk} \rangle$, by [8],

$$\langle \tilde{\mathcal{D}}^{(3)}_{jk} \rangle = N + N^2 [\langle |\tilde{I}_j|^2 \rangle + \langle |\tilde{I}_k|^2 \rangle + \langle |\tilde{I}_{-j-k}|^2 \rangle] + N^3 \langle \tilde{I}^{(3)}_{jk} \rangle, \quad (3)$$

where N is the average number of photons per frame.

In fact, the correction terms in eq. (3) that have to be applied to the triple correlation $\langle \mathcal{D}^{(3)}_{lm} \rangle$ to estimate $\langle I^{(3)}_{lm} \rangle$ simply correspond to *self-correlation* of photon events. Thus an unbiased estimate of $\langle I^{(3)}_{lm} \rangle$ is obtained if all self-correlation terms are ignored in the direct calculation of $\langle \mathcal{D}^{(3)}_{lm} \rangle$: there is no need to make the correction via the bispectrum of eq. (3). Using our existing machine-coded software, the unbiased triple correlation can be computed at a rate of approximately 100 s^{-1} for an average of 10 photons per frame.

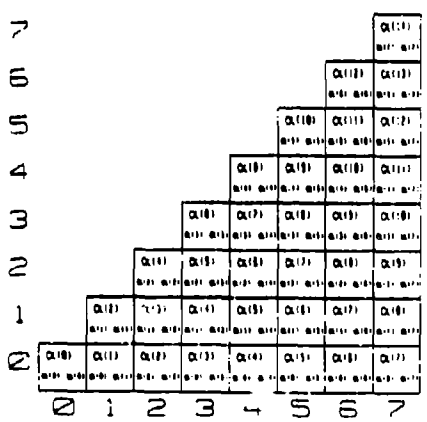

Fig. 1. Phase retrieval from the bispectrum. The boxes represent values of the bispectrum, for example, the box at (3,2) represents β_{32}. The upper value of α in each box is the value of the object spectrum recoverable from that value of β and the two earlier values of α given in the lower part of the box. For example, from β_{32} we can find α_5 if we already know α_2 and α_3.

The bispectrum is obtained by two dimensional Fourier transformation of the triple correlation. Our method of modulus and phase reconstruction of the object spectrum from the bispectrum essentially follows that of Bartelt et al. [2] except that, in determining the phase, a weighted average is used to allow for the varying modulus of the bispectrum. If α_l denotes the phase of the object spectrum and β_{lm} denotes the phase of the bispectrum, then, for a real object,

$$\beta_{lm} = \alpha_l + \alpha_m - \alpha_{-l+m}. \quad (4)$$

If both α_0 and α_1 are set to zero, then the resulting object is centred at the origin. The phases $\alpha_2, \alpha_3, \ldots$, etc. can be found by setting $m = 1$ and $l = 2, 3, \ldots$, etc. Fig. 1 illustrates how averaged estimates of the phases α_l can be found by averaging the values obtained along diagonals of the bispectrum.

3. Results

A long exposure image ($\sim 5 \times 10^4$ photons) of the stationary object (a double slit) is shown in fig. 2(a). With the object moving randomly, a long exposure produces the extremely blurred result shown in fig. 2(b). Centroiding of each frame prior to averaging ("shift-and-add") gives an improved result as shown in figs. 2(c), (d) and (e) for average detected photon rates of 7.6, 4.4 and 1.1 per frame respectively (of which 0.5 per frame is dark count). Centroiding barely reveals the presence of the second slit, even at the highest photon rates. Using the triple correlation and bispectrum, the reconstructions shown in figs. 2(f), (g) and (h) are obtained. Note that both slits are clearly distinguished in all cases. In fig. 2(h), the average detected photon rate of 1.1 per frame, of which 0.5 is dark count, meant that only 7% of frames contained the necessary 3 or more photons required for the evaluation of the triple correlation and the reconstruction was obtained using only 2089 frames.

Fig. 3 shows the effect of a uniform background superimposed upon the double slit image for background-to-signal ratios of approximately 1.4 : 1 (col 1), 2.8 : 1 (col 2) and 5.4 : 1 (col 3) and a signal photon rate of 3.1 per frame. In each case, row 3 shows the reconstructions obtained using simply a single line of the bispectrum and row 4 uses the complete octant.

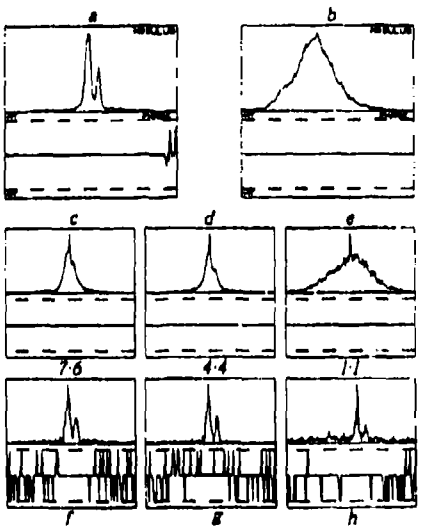

Although the reconstruction is improved when the full octant of the bispectrum is used, the improvement does not appear to be as great as simple reasoning suggests [8]. For the example shown in fig. 3 background-to-signal ratios up to 3 still permit reconstruction of the object from the bispectrum.

4. Conclusions and future work

We have demonstrated that a sharp image of a randomly moving object can be reconstructed at remarkably low light levels (less than one signal photon per frame) using the triple correlation and bispectrum. A machine-coded vector correlation algorithm can compute 100 triple correlations per second

Fig. 2. (a) Long exposure image of stationary object. (b) long exposure image of randomly moving object, (c)–(e) centroided short exposure images with 7.6, 4.4 and 1.1 detected photons per frame respectively (of which 0.5 is dark count), (f)–(h) corresponding reconstruction using the triple correlation. (The spike at the origin of (c)–(e) is a computer error and is not present in (d)–(f) of fig. 3)

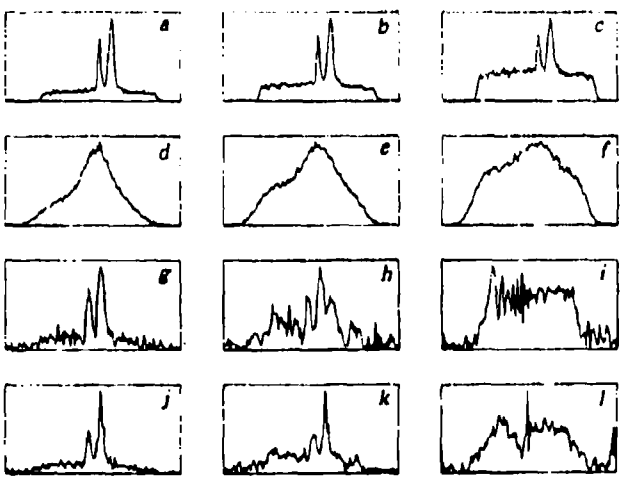

Fig. 3. Effect of a uniform background in triple correlation reconstructions. (a)–(c) long exposure images of stationary object with an average of 3.1 photons/frame in the signal (double slit) and 4.3, 8.7 and 16.7 photons/frame in the uniform background in (a), (b) and (c) respectively, (d)–(f) centroided short exposure images, (g)–(f) triple correlation reconstructions using one line of the bispectrum, (j)–(l) triple correlation reconstructions using the complete bispectrum.

(one- or two-dimensional) for 10 photons per frame and a relatively straightforward hard-wired correlator based on CMOS logic could achieve the same rate for 50–100 photons per frame, thus allowing on-line computation of the triple correlation. The principal problem in extending this to two dimensions lies in the storage capacity required for one complete octant of the bispectrum (~32 Mwords for a 128 × 128 image). It may be possible to use a selection of planes in the bispectrum to reconstruct the object with only a small loss in signal-to-noise ratio compared to a reconstruction using the complete octant.

Acknowledgement

This work was supported by grants from the UK SERC (GR/C 78940) and US Army (DAJA 45-85-C-0028). We thank Dr. K. O'Donnell for helpful discussions and D. Newman for assistance with the Image Photon Detector.

References

[1] A.W. Lohmann and B. Wirnitzer, Proc. IEEE 72 (1984) 889.
[2] H. Bartelt, A.W. Lohmann and B. Wirnitzer, Appl. Optics 23 (1984) 3121.
[3] T. Matsuoka and T.J. Ulrich, Proc. IEEE 72 (1984) 1403.
[4] H. Bartelt and B. Wirnitzer, Optics Comm. 53 (1985) 13.
[5] D. Rees et al., J. Phys. E 13 (1980) 763.
[6] A. Blazit, L. Koechlin and A. Labeyrie, in: Image processing techniques in astronomy, eds. C. De Jager and H. Nieuwenhuijzen (D. Reidel, Holland, 1975).
[7] D. Newman, A.A.D. Canas and J.C. Dainty, Appl. Optics (January, 1986).
[8] B. Wirnitzer, J. Opt. Soc. Am. A2 (1985) 14.

REF 4

A Reprint from the

PROCEEDINGS

Of SPIE-The International Society for Optical Engineering

SPIE Volume 808

Inverse Problems in Optics

31 March-1 April 1987
The Hague, The Netherlands

Photon limited imaging through turbulence

G. R. Ayers, J. C. Dainty, M. J. Northcott
Optics Section, Blackett Laboratory,
Imperial College, London SW7 2BZ, UK

Photon limited imaging through turbulence

G. R. Ayers, J. C. Dainty and M. J. Northcott

Optics Section, Blackett Laboratory, Imperial College, London SW7 2BZ, UK

Abstract

The imaging of objects through atmospheric turbulence has been studied for two particular cases: (i) when the telescope diameter D is much smaller than the atmospheric coherence scale r_o and (ii) when $D >> r_o$. Case (i) produces randomly moving images and case (ii) results in speckled images. In both cases, triple correlation techniques are investigated and compared with possible alternative methods, such as centroiding for (i) and the Knox-Thompson method for (ii). The triple correlation technique appears to be the most satisfactory one for both problems at low light levels.

Introduction

The image of a small object viewed through atmospheric turbulence shows, in general, two characteristic features: it randomly translates and is broken up into a speckle pattern. A detailed description of the effect of turbulence in imaging is given in Ref. 1, but the two characteristics can be understood in simple terms by considering the cases where the telescope diameter D is very much smaller than the atmospheric coherence scale r_o or very much greater than it. In the former case ($D << r_o$) a point source object appears as a randomly tilted wavefront in the telescope pupil and thus gives rise to a randomly translating image of the object. In fact, randomly translating images can also arise if the object itself is randomly translating or if the telescope is doing so, for example, because of guiding errors or wind buffeting the support structure. The method of object reconstruction described in this paper does not depend on the cause of the random shift in the image.

In the second case ($D >> r_o$), it is well-known that a speckled image is produced by a point source object as a result of interference of randomly phased areas in the telescope pupil. The technique of speckle interferometry[2,3] recovers a diffraction limited auto-correlation of the object intensity and it works at very low light levels, as low as a few detected photons per frame for simple structures such as binary stars. A multitude of speckle imaging techniques have been suggested[4]. The Knox-Thompson technique[5,6] calculates phase differences in the Fourier plane, the phase itself being found, in effect, by integration of the differences[4]. The triple correlation method[7-13], which is related to the technique of phase closure[14], is apparently more difficult to implement than the Knox-Thompson technique but possesses inherent advantages[15] discussed below.

In this paper we present experimental results and computer simulations for the two-dimensional imaging of a randomly translating object and computer simulation results for speckle imaging, in both cases at very low light levels. The details of the computational techniques[16] and detailed comparisons of different methods[15] are presented elsewhere. We start with a brief summary of the triple correlation and its relation to other correlation functions.

The triple correlation

The triple correlation $i^{(3)}(\underline{x}_1,\underline{x}_2)$ of a real function $i(\underline{x})$ is defined by[8]

$$i^{(3)}(\underline{x}_1,\underline{x}_2) = \int_{-\infty}^{\infty} i(\underline{x})\, i(\underline{x}+\underline{x}_1)\, i(\underline{x}+\underline{x}_2)\, d\underline{x} \qquad (1)$$

and its four dimensional Fourier transform, the bispectrum $I^{(3)}(\underline{u}_1,\underline{u}_2)$ by

$$I^{(3)}(\underline{u}_1,\underline{u}_2) = I(\underline{u}_1)\, I^*(\underline{u}_1+\underline{u}_2)\, I(\underline{u}_2)\,, \qquad (2)$$

SPIE Vol. 808 Inverse Problems in Optics (1987) / 19

where $I(\underline{u})$ is the two dimensional Fourier transform of $i(\underline{x})$. Note that, for two dimensional functions $i(\underline{x})$, the triple correlation and bispectrum are four dimensional and this causes an immediate problem regarding computer storage. Even taking account of the known symmetries[8], one would require 500 Mwords of memory for the bispectrum of a 256 x 256 function.

For comparison, the autocorrelation function $i^{(2)}(\underline{x}_1)$ and its Fourier transform, the energy spectrum $I^{(2)}(\underline{u}_1)$ are defined for real $i(\underline{x})$ by

$$i^{(2)}(\underline{x}_1) = \int_{-\infty}^{\infty} i(\underline{x})\, i(\underline{x} + \underline{x}_1)\, d\underline{x} \tag{3}$$

and

$$I^{(2)}(\underline{u}_1) = I(\underline{u}_1)\, I^*(\underline{u}_1) \tag{4}$$

The Knox-Thompson correlation $i^{(KT)}(\underline{x}_1, \Delta\underline{u})$ and its Fourier transform (with respect to $\underline{x}_1$) $I^{(KT)}(\underline{u}_1, \Delta\underline{u})$ are defined by

$$i^{(KT)}(\underline{x}_1, \Delta\underline{u}) = \int_{-\infty}^{\infty} i(\underline{x})\, i(\underline{x} + \underline{x}_1)\, \exp(2\pi\Delta\underline{u}.\underline{x})\, d\underline{x} \tag{5}$$

and

$$I^{(KT)}(\underline{u}_1, \Delta\underline{u}) = I(\underline{u}_1)\, I^*(\underline{u}_1 + \Delta\underline{u}) , \tag{6}$$

where $\Delta\underline{u}$ is a fixed, small vector.

If Eq.(2) is rewritten with $\underline{u}_2 = \Delta\underline{u}$, then

$$I^{(3)}(\underline{u}_1, \Delta\underline{u}) = I(\Delta\underline{u})\, I^{(KT)}(\underline{u}_1, \Delta\underline{u}) . \tag{7}$$

Thus, a single plane of the bispectrum for a small fixed value of $\Delta\underline{u}$, is equal to the Knox-Thompson cross-spectrum multiplied by an object-dependent quantity $I(\Delta\underline{u})$.

There are several different techniques that can be used to compute the various correlation functions and their Fourier transforms at low light levels[6]. For direct calculation of correlation, a vector differencing algorithm is the most efficient at low light levels[7]. However, reconstruction algorithms that require the bispectrum would necessitate taking the four-dimensional Fourier transform of this triple correlation and this is not practical on grounds of speed or computer memory for large arrays. In such cases we either compute selected sub-planes of the bispectrum or use tomographic techniques. Selected planes of the bispectrum, Eq.(7), are found by calculating their inverse Fourier transform directly using a weighted photon differencing algorithm[8] and then Fourier transforming the result, or by direct Fourier transforming using Eq.(3). In the tomographic method, the two dimensional photon data is projected onto a line at angle θ, thus reducing the dimensionality of the calculation. This is repeated for several angles (36 in the results below). In all cases of photon differencing, bias terms due to self-correlation of photons are avoided by excluding from the calculations all vector differences between a photon event and itself.

The method of reconstruction of the object spectrum from the bispectrum essentially followed that described in Refs 9 and 10, with some speed improvement. The object intensity was found by simple inverse Fourier transformation. Both of these reconstruction steps have scope for improvement; e.g. the inverse Fourier transformation is not positive-constrained

Randomly moving objects

Laboratory experiments and computer simulations have been carried out on imaging a randomly moving two dimensional object at very low light levels. Earlier experiments[18] on a one dimensional object indicated that object reconstruction can be achieved at average signal levels on the order of 1 detected photon per frame and 30,000 frames.

Figure 1 shows a schematic of the experimental apparatus. The random motion was achieved by tilting a mirror linked by a lever to randomly driven loudspeaker coils. The Imaging Photon Detector (IPD) is a microchannel plate/resistive anode device[19] with 256 x 256 pixel coordinates, although in the experiment the pixel area was restricted to 32 x 32.

To image a randomly translating object we clearly must average some quantity that is translation-invariant. The autocorrelation, Eq.(3), (or energy spectrum) satisfies this condition, but it is not, in general, possible to reconstruct an object unambiguously from its autocorrelation function[4]. The triple correlation is also translation-invariant and is therefore ideally suited to this problem as first pointed out by Bartelt and Wirnitzer[20].

All calculations were carried out on an HP9836 desktop computer: the total time taken to complete the bispectrum of 2000 frames with an average of 15 detected photons per frame was approximately 20 hours and the reconstruction from the bispectrum was accomplished in a few minutes. The results are shown in Figure 2. Simple centroiding prior to averaging yields a blurred result, as in Fig.2(b) - in fact, centroiding can possibly be done in a more intelligent way by grouping together all frames with the same number of detected photons[21], but this has not been attempted yet. The result derived from the triple correlation, Figure 2(c), using 2000 frames and an average of 15 detected photons per frame (approximately 0.1 photons per object pixel) compares favourably with the original. However, the reconstruction is not perfect and it is believed that this was due to imperfections in the flat-field response of the IPD. A computer simulation for this case gave almost perfect reconstruction with 2000 frames.

A computer simulation study was carried out for a second object, comprising approximately 150 pixels with a pixel area of 128 x 128 (see Figure 3). Again, 2000 frames at an average photon rate of 15 photons per frame (~ 0.1 photons per object pixel) were used. A sun3/160 computer and Sky "Warrior" array processor were used to generate the data, calculate the bispectrum and reconstruct the object from the bispectrum. Two methods of calculating the bispectrum were used: in the first (reconstruction shown in Fig.3(c)),selected planes were computed and in the second (Fig 3(d)) a tomographic technique using 36 angles was used. Despite the very low photon flux of approximately 0.1 per object pixel on average, the reconstructions are of high quality. The computing time for Fig 3(c) was approximately 50 min (compared to approx 20 hr for the 32 x 32 array in Fig.2), i.e. approx 1.5s per frame.

Speckle imaging

Speckle interferometry gives a good estimate of the Fourier modulus $|O(\underline{u})|$ of an object, but does not provide the Fourier phase. The Knox-Thompson method gives estimates of phase differences in the Fourier plane of the image as can be seen by taking the argument of Eq.(16):

$$\varphi_I^{(KT)}(\underline{u}_1, \Delta\underline{u}) = \varphi_I(\underline{u}_1) - \varphi_I(\underline{u}_1 + \Delta\underline{u}), \tag{8}$$

where φ_I is the phase of the image spectrum and $\Delta\underline{u}$ is a fixed (small) vector. The Knox-Thompson transfer function is purely real (to first order[4]) and thus the phase of the object spectrum $\varphi_O(\underline{u})$ is simply equal to that of the image spectrum $\varphi_I(\underline{u})$.

Taking the argument of Eq.(7), it is clear that, for a single image, the phase $\varphi_I^{(3)}(\underline{u}_1, \Delta\underline{u})$ of the bispectrum is equal to that given by the Knox-Thompson method plus $\varphi_I(\Delta\underline{u})$:

$$\varphi_I^{(3)}(\underline{u}_1, \Delta\underline{u}) = \varphi_I^{(KT)}(\underline{u}_1, \Delta\underline{u}) + \varphi_I(\Delta\underline{u}). \tag{9}$$

For a single image, $\varphi_I(\Delta\underline{u})$ is a constant and may be taken to be zero. Thus, the Knox-Thompson quantity is equivalent to a single plane of the bispectrum.

Consider now the measurement of the ensemble average of Eqs.(2) and (6) for the triple

correlation and Knox-Thompson methods respectively, where the images have random displacements due to random tilts in the incident wavefront. The triple correlation is invariant to translation, whereas it is necessary to exactly centroid the image intensity to obtain translation invariance in the Knox-Thompson technique[17]. In principle, this can be done at high light levels but not when there are only a few detected photons per frame. However, the results of computer simulations indicate that > 100 detected photons per frame are probably required for imaging all but the very simplest objects and thus, in practice, the Knox-Thompson method is effectively translation invariant provided the data is centroided prior to processing.

The signal-to-noise ratio of a measurement of a single plane of the bispectrum, Eq.(7), is less than that on the Knox-Thompson cross-spectrum, Eq.(6)[15]; lower order moments can always be estimated more accurately than higher order ones. On the other hand, additional phase estimates can be obtained from other planes in the bispectrum. These phase estimates are not all statistically independent and their error increases as one moves off the main diagonal $u_1 = -u_2$ of the bispectrum; this fact should be taken into account in the reconstruction algorithm. Results of computer simulations indicate that the two techniques give approximately the same signal-to-noise ratio for point-like objects.

The principal advantage of reconstruction from the bispectrum is that it avoids the problems caused by small values of the modulus in the Knox-Thompson method. These occur at points in the Fourier plane where the modulus is zero or small, and the fixed value $\Delta\underline{u}$ does not allow simple ways around this problem. The effect in practice is to limit the upper spatial frequency of phase recovery and is object-dependent.

Computer simulations of speckle imaging have been carried out to compare the Knox-Thompson and triple correlation techniques. In a typical simulation, 20,000 photon-limited 128 x 128 speckle frames are generated in the following way: (a) generate a correlated Gaussian phase process of appropriate variance and correlation length in the pupil, (b) Fourier transform and take square modulus to generate intensity point spread function (speckle image of point source), (c) convolve with object intensity, (d) generate photons via a Poisson random number generator. Using the Sun3/160 and array processor, it takes approximately 1s to generate one set of photon coordinates (i.e. one image). Figure 4 shows some computer-generated stellar speckle patterns, for a D = 2m telescope, r_o = 10 cm, λ = 500 nm, spatial frequency cut-off = 19.4 arc sec^{-1}.

Figure 5 compares reconstructions of an asteroid-like object via the two techniques for 12,000 frames with an average of 100 detected photons per frame: assuming a wavelength bandwidth $\delta\lambda$ = 20 nm, exposure time of 10^{-2}s and a D = 2m telescope, this corresponds to an integrated magnitude of $m_v \sim 15$ for the asteroid, whose extent is approximately 0.5 arc sec by 1.0 arc sec.

Acknowledgments

This work was supported by the UK Science and Engineering Research Council (GR/D 92332) and the US Army (DAJA45-85-C-0028).

References

1. Roddier, F., in Progress in Optics, Vol XIX, edited by E Wolf, North Holland 1981, pp. 281-376.
2. Labeyrie, A., Astron. and Astrophys., Vol. 6, pp. 85-87. 1970.
3. Dainty, J. C., in Laser Speckle and Related Phenomena, edited by J. C. Dainty, Springer-Verlag, 1984, pp. 255-320.
4. Dainty, J. C. and Fienup, J. R., in Image Recovery: Theory and Applications, edited by H. Stark, Academic Press 1987.
5. Knox, K. T. and B. J. Thompson, Astrophys J., Vol. 193, pp. L45-48. 1974.
6. Fontanella, J. C. and Seve, A., J. Opt. Soc. Am. A, Vol. 4, pp. 438-448. 1987.
7. Weigelt, G. P., Opt. Commun., Vol. 21, pp. 55-59. 1977.
8. Lohmann, A. W. and Wirnitzer, B., Proc. IEEE, Vol. 72, pp. 59-59. 1977.
9. Bartelt, H., Lohmann, A. W. and Wirnitzer, B., Appl Opt., Vol. 23, pp. 3121-3129. 1984.
10. Lohmann, A. W., Weigelt, G. and Wirnitzer, B., Appl. Opt., Vol. 22, pp. 4028-4037. 1983.
11. Wirnitzer, B., J. Opt. Soc. Am. A, Vol. 2, pp. 14-21. 1985.
12. Hofmann, K-H and Weigelt, G., Astron Astrophys., Vol. 167, pp. L15-L16. 1986.
13. Hofmann, K-H and Weigelt, G., Appl. Opt., Vol. 25, pp. 4280-4286. 1986.
14. Roddier, F., Opt. Commun., Vol. 60, pp. 145-148. 1986.
15. Ayers. G. R., Dainty, J. C. and Northcott, M. J., in preparation for J. Opt. Soc. Am.A
16. Northcott, M. J. and Ayers, G. R., in preparation for J. Opt. Soc. Am. A.
17. Blazit, A., Koechlin, L. and Oneto, J. L., in Image Processing Techniques in Astronomy, edited by H. van Schooneveld, D. Reidel, 1975.

18. Dainty, J. C. and Northcott, M. J., Opt. Commun., Vol. 58, pp. 11-14. 1986.
19. Rees, D., et al, J. Phys. E., Vol. 13, pp. 763-774. 1980.
20. Bartelt, H. and Wirnitzer, B., Opt. Commun., Vol. 53, pp. 13-16. 1985.
21. de Freitas, L. C. et al, in preparation for SPIE 31st Annual Technical Symposium, August 1987.

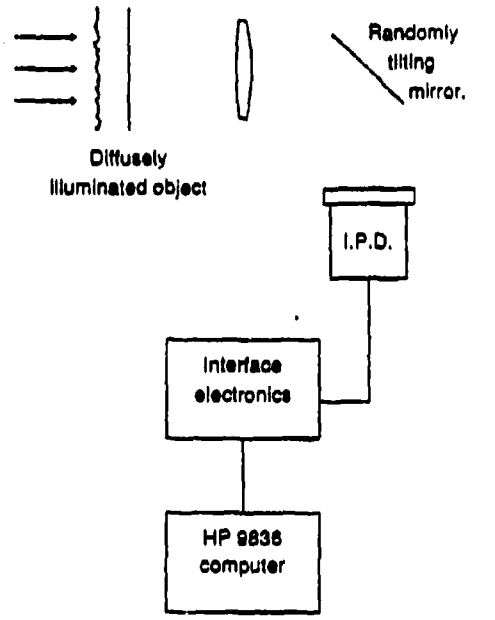

Figure 1 Schematic of equipment for experiments using a randomly moving object.

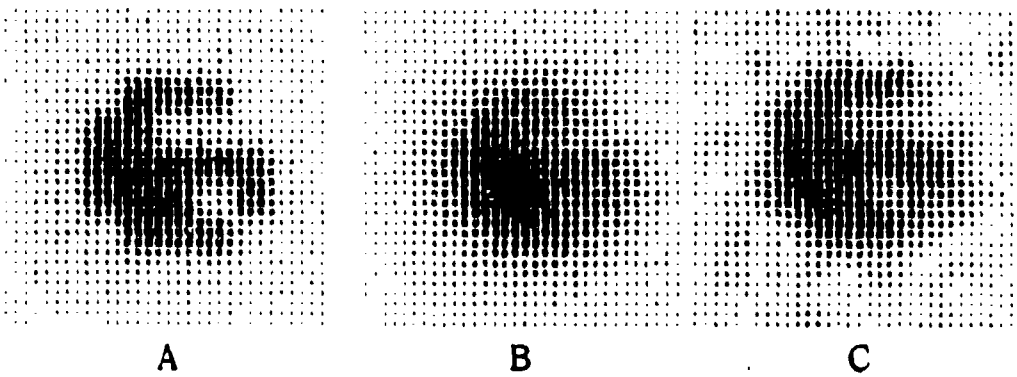

Figure 2 Experimental results on the imaging of a randomly moving object at very low light levels (average of 15 detected photons per frame, 2000 frames). (A) - image of stationary object (B) - centroided image (C) - image reconstructed from the triple correlation method.

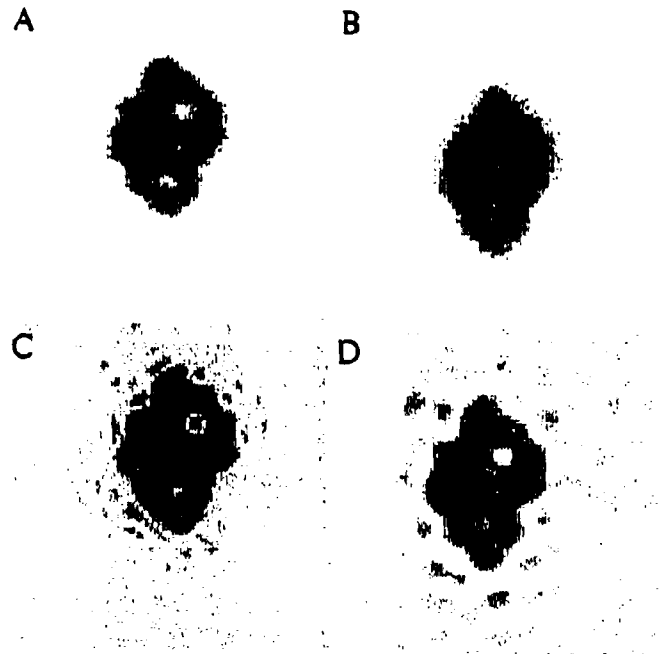

Figure 3 Computer simulation results for imaging a randomly moving object (average of 15 detected photons per frame, 2000 frames).
A - image of stationary object
B - centroided image
C - reconstruction from bi-spectrum using selected planes
D - using radon transform and bispectrum

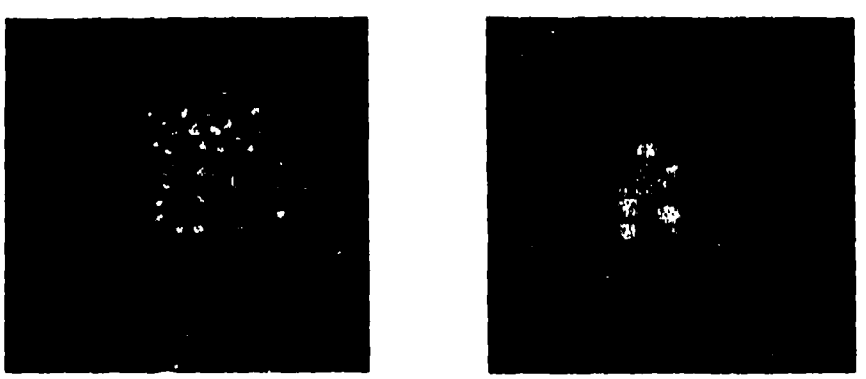

Figure 4 Computer-generated stellar speckle patterns of a point source (left) and a uniform disc (right).

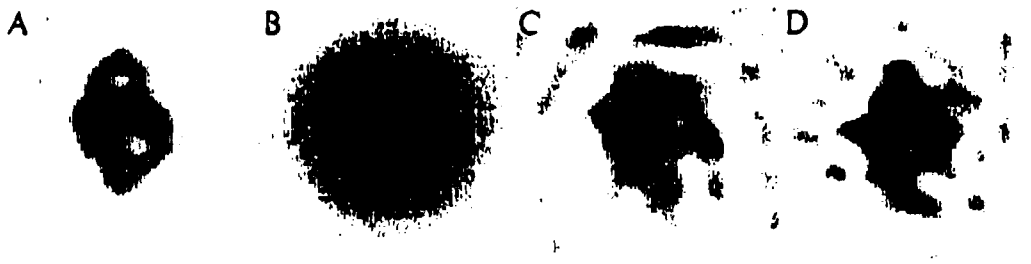

Figure 5 Computer simulation of imaging an asteroid-like object through turbulence. In each case, 12,000 frames with an average of 100 detected photons per frame was used.
(A) - diffraction-limited image of object
(B) - long-exposure image through turbulence
(C) - reconstruction using the Knox-Thompson method
(D) - reconstruction using the bispectrum method.
At this light level, more frames are required to yield an acceptable reconstruction. Examination of the spectrum of the reconstructions C and D shows that the bispectrum reconstruction is superior to that of the KT method.

828 01

REF 5

Speckle imaging techniques

J C. Dainty

Blackett Laboratory, Imperial College, London SW7 2BZ, UK

ABSTRACT

Several proposed techniques of focal plane imaging through turbulence are described and compared. The techniques are: shift-and-add, exponential filter, Knox-Thompson (cross-spectrum) and triple correlation. Particular attention is given to the performance of the methods at extremely low light levels of a few detected photons per frame.

INTRODUCTION

Speckle interferometry, as invented by Labeyrie[1], provides an estimate of the diffraction limited autocorrelation or energy spectrum of an object. In a linear, isoplanatic, incoherent imaging system, the image intensity $i(\underline{x})$ is related to the object intensity $o(\underline{x})$ by a convolution relationship,

$$i(\underline{x}) = o(\underline{x}) * p(\underline{x}) , \qquad (1)$$

where * denotes convolution and $p(\underline{x})$ is the instantaneous point spread function of the optical system. When imaging through turbulence, $p(\underline{x})$ is a random speckle pattern whose statistics are similar to those of laser speckle patterns[2]. In Fourier space, Eq.(1) is

$$I(\underline{u}) = O(\underline{u}) \, . \, P(\underline{u}) , \qquad (2)$$

where the upper-case functions denote the Fourier transforms of the lower-case ones; the quantity $P(\underline{u})$ is the instantaneous telescope-atmosphere transfer function.

In conventional long-exposure imaging, one forms the average,

$$\langle I(\underline{u}) \rangle = O(\underline{u}) \, . \, \langle P(\underline{u}) \rangle \qquad (3)$$

and, as is well-known, the average telescope-atmosphere transfer function $\langle P(\underline{u}) \rangle$ drops off rapidly for angular spatial frequencies greater than r_o/λ, where r_o, the Fried parameter, is typically 10 cm at a good observing site.

In speckle interferometry, one forms an average of the energy spectrum,

$$\langle I^{(2)}(\underline{u}) \rangle = \langle I(\underline{u}) \, I^*(\underline{u}) \rangle$$

$$= O^{(2)}(\underline{u}) \, . \, \langle P^{(2)}(\underline{u}) \rangle . \qquad (4)$$

In Eq.(4), the superscript $^{(2)}$ denotes that a second order correlation is being performed, which in image space could be written

$$\langle i^{(2)}(\underline{x}_1) \rangle = \langle \int_{-\infty}^{\infty} i(\underline{x}) \, i(\underline{x} + \underline{x}_1) \, d\underline{x} \rangle , \qquad (5)$$

As originally shown by Korff [3], the speckle transfer function $\langle P^{(2)}(\underline{u}) \rangle$ contains a diffraction-limited component and thus allows the estimation of the energy spectrum of the object up to an angular spatial frequency of D/λ, where D is the telescope diameter.

As a result of Eq (4), speckle interferometry has three properties that have contributed significantly to its success in astronomy:

(i) it provides diffraction-limited information about the object structure ,
(ii) that information is perturbed by a linear transfer function, and
(iii) the image energy spectrum can be evaluated at very low light levels using

DAINTY 1

photon correlation techniques [4].

Regarding point (ii), it is not essential that the transfer process be linear, but it is usually desirable and in any case the imaging process must be well-understood and have an inverse solution so that object data can be found quantitatively.

Clearly, neither Eq.(4) or (5), provides an estimate of the object map $o(\underline{x})$ directly. Methods of trying to estimate $o(\underline{x})$ from its energy spectrum $O^{(2)}(\underline{u})$ are reviewed in these Proceedings by Fienup and elsewhere[3]. The problem is that of estimating the phase $\phi(\underline{u})$ of $O(\underline{u})$, given the squared modulus $O^{(2)}(\underline{u}) = |O(\underline{u})|^2$. Although a considerable amount of effort has gone into solving this problem, no general solution exists. Furthermore, speckle patterns contain information that is additional to that given by the energy spectrum and this should be exploited when finding the object map.

In the following section we review briefly four proposed methods of speckle imaging, each of which processes the raw speckle data in a different way to Labeyrie's speckle interferometry. However, it is desirable that any proposed technique of speckle imaging retains the advantageous properties (i) - (iii) of the original speckle technique, as well as giving an estimate of the object map. Property (iii), the ability to work at very low light levels, is particularly important, since just about any method works when photon noise is neglected.

FOUR PROPOSED TECHNIQUES OF SPECKLE IMAGING

A. Shift-and-add

In this method, first proposed by Lynds et al[6] and considerably extended by Bates[7-9] and others[10], one averages centroided versions of selected bright speckles. At high light levels, the method would have linear transfer function if each "speckle" were a randomly translated, linearly degraded image of the original object. This is not the case, as shown by Hunt et al[11], and the shift-and-add method is not linear at high light levels. There is also the problem of identifying bright speckles in photon-limited data.

Recently, we have analysed shift-and-add imaging at very low light levels for the case of a randomly translating object[12] (whose imaging is linear at high light levels). The photon-limited case is also fundamentally non-linear. If $\langle Q_N(\underline{u}) \rangle$ denotes the Fourier spectrum of the average of all centroided frames that contain exactly N detected photons and $I(\underline{u})$ denotes the normalised Fourier spectrum of the high light level intensity of the original (unshifted) image, then

$$\langle Q_N(\underline{u}) \rangle = N\, I\left(\frac{N-1}{N}\,\underline{u}\right) \left[I^*\left(\frac{\underline{u}}{N}\right)\right]^{N-1} \qquad (6)$$

Thus, for example, for N = 2

$$\langle Q_2(\underline{u}) \rangle = 2\, |I(\tfrac{\underline{u}}{2})|^2 , \qquad (7)$$

that is, the spectrum of the shift-and-add image is proportional to the energy spectrum of the true image. Equation (6) has interesting implications for phase retrieval[13].

B. Exponential filtering

For modulus-only reconstruction in one dimension, the solution is ambiguous because the complex zeros of the energy spectrum of the object include both the zeros of the original object and their inverses. The object can be reconstructed uniquely if its zeros can be identified correctly and Walker[13,14] showed that this can be done using an exponential filter in the image domain.

The average energy spectrum of the image, $\langle I^{(2)}(\underline{u}) \rangle = \langle |I(\underline{u})|^2 \rangle$, is found in the usual way. A second energy spectrum $\langle I'^{(2)}(\underline{u}) \rangle$, is found by multiplying each frame $i(\underline{x})$ by an exponential, $\exp(-2\pi a x)$, where 'a' is a constant. It can be shown that

$$\langle I'^{(2)}(\underline{u}) \rangle = O'^{(2)}(\underline{u}) \cdot \langle P'^{(2)}(\underline{u}) \rangle , \qquad (8)$$

so that from the original data we can extract the energy spectrum of the object and that of the exponentially filtered object. In principle, these together contain sufficient information to reconstruct the object intensity. In practice, one has to use a modified version of the Fienup algorithm[7] to recover the object map and no satisfactory modification exists.

C Cross-spectrum method

This method was first proposed by Knox and Thompson[15]. The KT correlation, $I^{(KT)}(\underline{x}_1,\Delta\underline{u})$, and its Fourier transform (with respect to $\underline{x}_1$), $I^{(KT)}(\underline{u}_1,\Delta\underline{u})$, are defined by

$$I^{(KT)}(\underline{x}_1,\Delta\underline{u}) = \int_{-\infty}^{\infty} I^*(\underline{x})\, I(\underline{x}+\underline{x}_1)\exp(2\pi i\Delta\underline{u}.\underline{x})\, d\underline{x} \qquad (9)$$

and

$$I^{(KT)}(\underline{u}_1,\Delta\underline{u}) = I(\underline{u}_1)\, I^*(\underline{u}_1+\Delta\underline{u}) , \qquad (10)$$

where $\Delta\underline{u}$ is a fixed small vector.

When applying Eqs.(9) and (10) to speckle imaging, an average is taken over many speckle frames and it can be shown that

$$\langle I^{(KT)}(\underline{u}_1,\Delta\underline{u})\rangle = O^{(KT)}(\underline{u}_1,\Delta\underline{u}) \cdot \langle P^{(KT)}(\underline{u}_1,\Delta\underline{u})\rangle , \qquad (11)$$

where $$O^{(KT)}(\underline{u}_1,\Delta\underline{u}) = O(\underline{u}_1)\, O^*(\underline{u}_1+\Delta\underline{u}) \qquad (12)$$

and $$\langle P^{(KT)}(\underline{u}_1,\Delta\underline{u})\rangle \approx \langle P^{(2)}(\underline{u}_1)\rangle \cdot |\langle P(\tfrac{\Delta\underline{u}}{2})\rangle|^2 , \qquad (13)$$

where $\langle P\rangle$ is the seeing-limited transfer function. It follows from Eq (13) that $|\Delta\underline{u}|$ must be less than the seeing-limited angular frequency of r_o/λ for diffraction-limited information to be retained in Eq.(11). It also follows that the phase of the KT transfer function is zero and thus, taking the argument of Eq (11),

$$\varphi^{(KT)}(\underline{u}_1,\Delta\underline{u}) = \varphi_o(\underline{u}_1) - \varphi_o(\underline{u}_1+\Delta\underline{u}) , \qquad (14)$$

where $\varphi^{(KT)}$ is the phase of $I^{(KT)}$ and $\varphi_o(\underline{u})$ is the phase of $O(\underline{u})$.

Thus the KT technique gives phase difference information in the spectrum of the object and the phase has to be found by integration[17], avoiding phase dislocations.

D. Triple correlation

This method was first applied to speckle imaging by Weigelt[18-20] and is described in more detail elsewhere in these Proceedings and in reviews[21]. The triple (auto-) correlation and its Fourier transform, the bispectrum, are defined by

$$I^{(3)}(\underline{x}_1,\underline{x}_2) = \int_{-\infty}^{\infty} I^*(\underline{x})\, I(\underline{x}+\underline{x}_1)\, I(\underline{x}+\underline{x}_2)\, d\underline{x} \qquad (15)$$

DAINTM 3

and

$$I^{(3)}(\underline{u}_1,\underline{u}_2) = I(\underline{u}_1)\, I^*(\underline{u}_1+\underline{u}_2)\, I(\underline{u}_2)\ . \tag{16}$$

In speckle imaging, the average bispectrum of the image is related to that of the object through a bispectrum transfer function $\langle P^{(3)}(\underline{u}_1,\underline{u}_2)\rangle$,

$$\langle I^{(3)}(\underline{u}_1,\underline{u}_2)\rangle = O^{(3)}(\underline{u}_1,\underline{u}_2)\ .\ \langle P^{(3)}(\underline{u}_1,\underline{u}_2)\rangle \tag{17}$$

As with the KT technique, the bispectrum transfer function is non-zero in magnitude and has zero phase up to the diffraction limit of the telescope. Using this fact and taking the argument of Eq.(16), we find that

$$\phi^{(3)}(\underline{u}_1,\underline{u}_2) = \phi_o(\underline{u}_1) - \phi_o(\underline{u}_1+\underline{u}_2) + \phi_o(\underline{u}_2)\ , \tag{18}$$

where $\phi^{(3)}$ is the bispectrum phase. A recursive algorithm can be used to reconstruct the phase of the object transform, $\phi_o(\underline{u})$, from the bispectrum phase.

COMPARISON OF CROSS-SPECTRUM AND BISPECTRUM

If Eq.(16) for the bispectrum of a single frame is written with $\underline{u}_2 = \Delta\underline{u}$, then, for a single 'plane' of the bispectrum,

$$\begin{aligned} I^{(3)}(\underline{u}_1,\Delta\underline{u}) &= I(\underline{u}_1)\, I^*(\underline{u}_1+\Delta\underline{u})\, I(\Delta\underline{u}) \\ &= I^{(KT)}(\underline{u}_1,\Delta\underline{u})\, I(\Delta\underline{u})\ , \end{aligned} \tag{19}$$

and thus this plane of the bispectrum equals the cross-spectrum multiplied by an image-dependent number $I(\Delta\underline{u})$. Taking the argument of Eq (19),

$$\phi^{(3)}(\underline{u}_1,\Delta u) = \phi^{(KT)}(\underline{u}_1,\Delta\underline{u}) + \phi(\Delta\underline{u}) \tag{20}$$

The phase of the bispectrum is invariant to a translation of the image (this is clear from Eqs.(15) and (16)) whereas that of the cross-spectrum is not shift-invariant. When implementing the KT algorithm in practice, it is necessary to centroid each frame prior to processing and this is equivalent, in the noise sense, of calculating a single plane of the bispectrum.

Exact analytical expressions for the KT and bispectrum transfer functions are difficult to obtain and instead we have used Monte Carlo techniques to compare them. Figure 1 compares the two transfer functions for equivalent subplanes for realistic atmospheric parameters.

Signal-to-Noise Ratios

Both the cross-spectrum and triple correlation are complex quantities and thus both the signal-to-noise ratio of the modulus, SNR_m, and the phase error E_ϕ are of interest. The method of Goodman and Belsher[23] for finding SNR_m for the energy spectrum can be extended to the cross-spectrum and bispectrum for both SNR_m and E_ϕ[22]. Figure 2 shows SNR_m and E_ϕ in the frequency domain for an asteroid type of object and an imaging system with a unit transfer function (i.e. no atmospheric turbulence), for a mean number N = 100 photons per frame for equivalent cross-spectrum (KT) and bispectrum sections. Note that the SNR_m is lower (and E_ϕ higher) for the bispectrum case, confirming the general result that errors are always higher on higher moments.

Note that, in practice,

$$E_\phi \approx \frac{1}{\sqrt{2}\ SNR_m}\ , \tag{21}$$

as assumed by Nisenson and Papaliolios[24] in their analysis of the effect of photon noise on the KT algorithm.

In the presence of atmospheric turbulence, the expressions for the signal-to-noise ratio per frame in the cross-spectrum and bispectrum can become quite complicated[22]. At high light levels, then

$$\mathrm{SNR}^{(\mathrm{TC})} \sim 1 \quad , \qquad |\underline{u}_2| < r_o/\lambda$$

and (22)

$$\mathrm{SNR}^{(\mathrm{KT})} \sim 1 \quad , \qquad |\Delta\underline{u}| < r_o/\lambda$$

For $|\Delta\underline{u}| \gg r_o/\lambda$, $\mathrm{SNR}^{(\mathrm{KT})} = 0$, whereas for $|\underline{u}_2| \gg r_o/\lambda$,

$$\mathrm{SNR}^{(\mathrm{TC})} = \frac{2T^{(3)}(\underline{u}_1,\underline{u}_2)}{n_s\, T^{(2)}(\underline{u}_1)\, T^{(2)}(\underline{u}_1-\underline{u}_2)\, T^{(2)}(\underline{u}_2)} \quad , \tag{23}$$

where $T^{(n)}$ is the normalised overlap area of n pupils.

At low light levels, in the important region $|\Delta\underline{u}|$ and $|\underline{u}_2| < r_o/\lambda$, both signal-to-noise ratios show a linear dependence on the average number of photons per speckle, just like the power spectrum case. For $|\Delta\underline{u}|$ and $|\underline{u}_2| \gg r_o/\lambda$, the cross-spectrum has a signal-to-noise of essentially zero, whereas the bispectrum maintains a small value which is strongly dependent on the average number of speckles per frame.

ACKNOWLEDGEMENTS

I am grateful to G R Ayers, I C de Freitas and M J Northcott for their contributions to this and related work, which is supported by Grant GR/D 92332 from the UK Science and Engineering Research Council and Contract DAJA45-85-C-0028 from the US Army.

REFERENCES

1. A. Labeyrie, Astron and Astrophys, Vol 6, pp 85-87, (1970).
2. J. W. Goodman, in Laser Speckle and Related Phenomena, edited by J C. Dainty, Springer-Verlag, pp 9-75, (1984).
3. D. Korff, J. Opt. Soc. Am., Vol 63, pp 971-980, (1973).
4. J. C. Dainty in Ref. 2, pp 255-320.
5. H. Stark (editor), Image Recovery: Theory and Application, Academic Press, (1987)
6. C. R. Lynds, S. P. Worden and J. W. Harvey, Astrophys. J., Vol 207, pp 174-180, (1976).
7. R. H. T Bates and F. M. Cady, Opt Commun., Vol 32, pp 365-369, (1980).
8. F. M. Cady and R. H. T. Bates, Opt. Lett., Vol 5, pp 438-440, (1980).
9. A M. Sinton, B. I. K. Davey and R. H. T. Bates, J. Opt Soc. Am., Vol A3, 1010-1017, (1986).
10. J. C. Christou et al, Opt. Engng., Vol 25, pp 724-730, (1986).
11. B. R. Hunt, W. R Fright and R H. T. Bates, J Opt Soc. Am., Vol 73, pp 456-465, (1983).
12. I. C. de Freitas et al, this Proceedings.
13. J. G Walker, Optica Acta, Vol 28, pp 735-738, (1981)
14. J. G. Walker, Appl Opt., Vol 21, pp 3132-3137, (1982)
15. K. T. Knox and B. J. Thompson, Astrophys. J., Vol 193, pp L45-48, (1974)
16. M P. Rimmer, Appl Opt., Vol 13, pp 623-629, (1974)
17. B R. Hunt, J Opt Soc. Am., Vol 69, pp 393-399, (1979).
18. G. Weigelt, Opt Commun., Vol 21, pp 55-59, (1977).
19. A. W. Lohmann, G. Weigelt and B. Wirnitzer, Appl Opt., Vol 22, 4028-4037, (1983).
20. H. Bartelt, A W. Lohmann and B. Wirnitzer, Appl. Opt., Vol 23, 3121-3129, (1984).
21. A. W. Lohmann and B. Wirnitzer, Proc. IEEE, Vol 72, pp 889-901, (1984).
22. G. R. Ayers, M. J. Northcott and J. C. Dainty, in preparation for J. Opt. Soc. Am.
23. J. W. Goodman and J. F. Belsher, Proc SPIE, Vol 75, pp 141-154, (1976)
24. P. Nisenson and C. Papaliolios, Opt. Commun., Vol 47, pp 91-96, (1983).

DAINTY 5

828 01

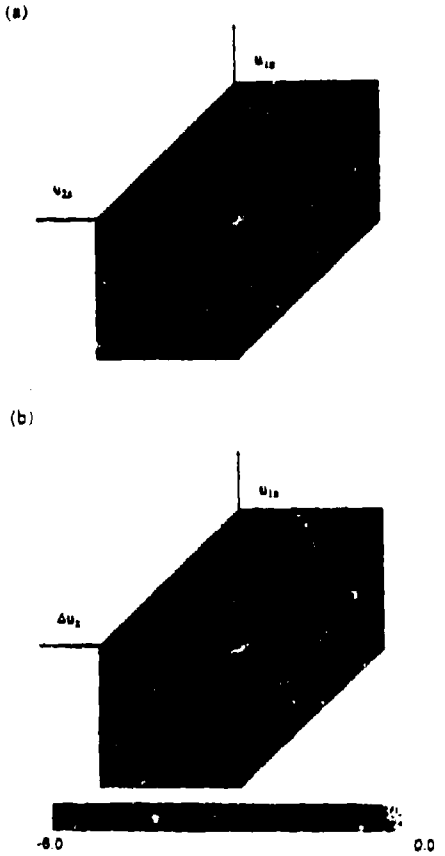

Figure (1)

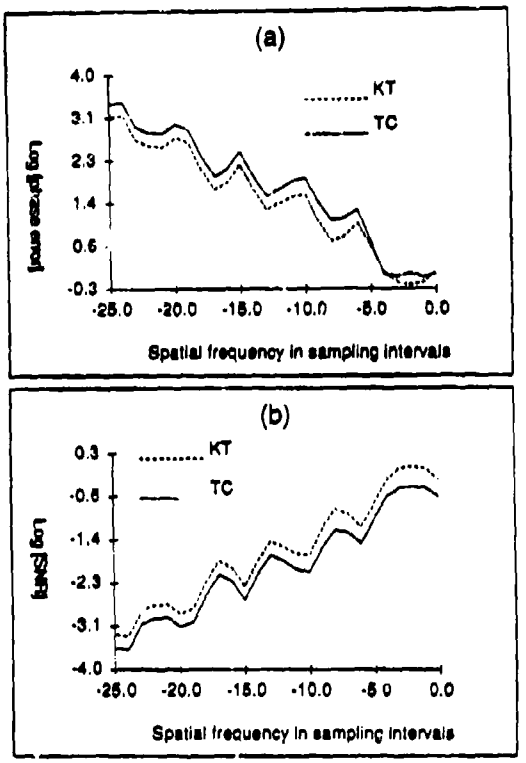

Figure (2)

OBJECT RECONSTRUCTION FROM PHOTON-LIMITED CENTROIDED DATA OF RANDOMLY TRANSLATING IMAGES

L.C. de Freitas, M. Northcott, B.J. Brames and J.C. Dainty

Optics Section - Blackett Laboratory
Imperial College - London SW7 2BZ - U.K.

ABSTRACT

Centroiding is investigated as a simple and computationally fast technique of image reconstruction, at low light level, of a randomly translating image. The detected frames are sorted by their number of photons, centroided, separated averages performed and then compared with the usual way of centroiding frames. An algorithm for retrieving the phase for one-dimensional centroided imaging is presented and computer simulated data is used to test the theory and the reconstruction technique.

1 - INTRODUCTION

The diffraction-limited image resolution of a ground-based 4 metre telescope operating at 400 nm is approximately 0.025" (arc second). Atmospheric turbulence, however, makes the image of an unresolved star broader ~ 1.0" (one second of arc) and exhibit a granular structure resembling a speckle pattern.

A number of techniques have been developed to retrieve the diffraction-limited image by recording short-exposure frames of these speckle patterns. The SHIFT-AND-ADD (SAA) method[1-5] is one of the proposed techniques. It relies on the proposition that each frame consists of many distorted replicas of the true image and that an improved estimate of the image could be found by superimposing these distorted replicas. The superposition is carried out by considering that the brightest part of a speckle image is, most likely, a distorted version of the brightest part of the true image. In each frame, the brighter speckles are found and by shifting and superimposing them at the centre of the frame (SHIFT-AND-ADD) the imperfections of the individual images tend to average out.

At very low light levels, for example, the mean number of photons/frame $\overline{N} < 10$ photons/frame, however, each of these distorted images may have only a few photons and no "bright" speckle can be chosen in order to implement the SAA technique. As a first approach on how the shift-and-add (SAA) technique behaves, at very low light levels, a theoretical study is presented focusing on centroiding photon-limited data emitted from a randomly translating image . A relationship between these centroided images and the stationary normalised image $I(\mathbf{r})$ as well as a phase reconstruction algorithm is presented for the case of one-dimensional object. Computer simulated photon data emitted from a binary star system is used to assess the theory and the reconstruction algorithm.

2 - THEORY OF CENTROIDING DATA OF RANDOMLY TRANSLATING IMAGES

To "freeze" a randomly moving image, photons, that are all supposed to be emanated from the same randomly translating image, are detected during a series of short time intervals(frames). To retrieve the stationary image one should, for each frame, shift the photon vectors by the amount that the true centroid of the image is displaced in respect to the centre of the frame and average(add) over all the frames. The true centroid and hence the true shift vector $\mathbf{c}_k$, however, is unknown and another shift vector $\mathbf{R}_k$ must be determined (see Fig. 1). As an estimator for the true centroid, the centroid vector of the detected photons can be evaluated, all the photon vectors are then shifted by this estimator and an average image of many such frames is formed.

The relationship between this estimated image and the normalised stationary image $I(\mathbf{r})$ can be derived assuming that the N-photon data $d_k(\mathbf{x})$ detected on the k^{th} frame is modeled[6] as an inhomogeneous Poisson process mathematically described as:

$$d_k(\mathbf{x}) = \sum_{j=1}^{N} \delta(\mathbf{x} - \mathbf{x}_j) \tag{1}$$

Let $\mathcal{D}_k(\mathbf{u}, \mathbf{x}_1, \ldots, \mathbf{x}_N)$ be the Fourier transform of $d_k(\mathbf{x})$

$$\mathcal{D}_k(\mathbf{u}, \mathbf{x}_1, \ldots, \mathbf{x}_N) = \sum_{j=1}^{N} \int_{-\infty}^{+\infty} \delta(\mathbf{x} - \mathbf{x}_j) \exp(-i2\pi \mathbf{u} \cdot \mathbf{x}) d\mathbf{x}$$

$$= \sum_{j=1}^{N} \exp(-i2\pi \mathbf{u} \cdot \mathbf{x}_j) \tag{2}$$

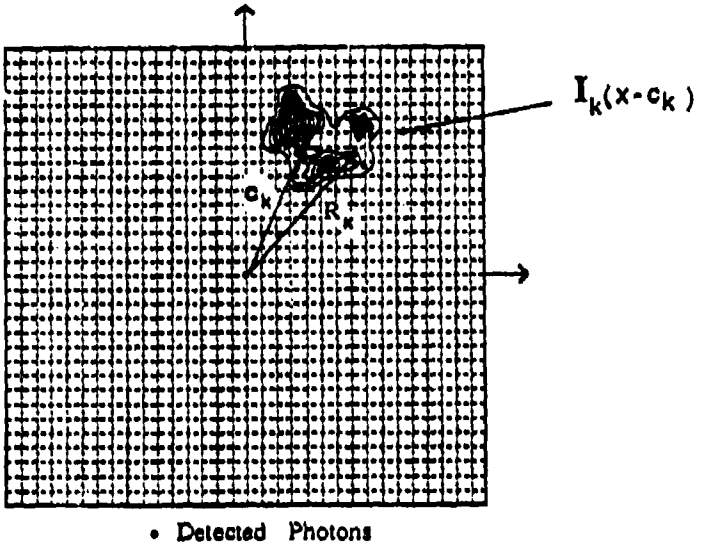

Figure 1 - Typical frame showing the true and the estimated shift vectors - c_k and R_k

The N photon centroid vector R_k of the k^{th} frame (Figure 1) is defined as

$$R_k = \frac{1}{N}\sum_{j=1}^{N} x_j \tag{3}$$

Substituting in terms of the centroid coordinates $r_j = x_j - R_k$ (Fig. 1) we have

$$\begin{aligned} \mathcal{D}_k(u, x_1, ..., x_N) &= exp(-i2\pi u \cdot R_k) \sum_{j=1}^{N} exp(-i2\pi u \cdot r_j) \\ &= exp(-i2\pi u \cdot R_k)\, \mathcal{D}_k^c(u, r_1, ...r_N) \end{aligned} \tag{4}$$

where $\mathcal{D}_k^c(u, r_1, ...r_N) = \mathcal{D}_k^c(u, x_1, ...x_N)$ is the Fourier transform of the centroided $\mathcal{D}_k(u, x_1, ...x_N)$.

The relation between the centroided and non-centroided data spectrum is therefore:

$$\begin{aligned} \mathcal{D}_k^c(u, x_1, ..., x_N) &= exp(+i2\pi u \cdot R_k)\, \mathcal{D}_k(u, x_1, ...x_N) \\ &= exp(+i2\pi u \cdot R_k) \sum_{j=1}^{N} exp(-i2\pi u \cdot x_j) \\ &= \sum_{j=1}^{N} exp(+i2\pi u \cdot \frac{x_1}{N}) ..... exp(-i2\pi u \cdot [1 - \frac{1}{N}]x_j) ..... exp(+i2\pi u \cdot \frac{x_N}{N}) \end{aligned} \tag{5}$$

Due to the dependence of $\mathcal{D}_k^c(u, x_1, ..., x_N)$ on the photon coordinates x_j the ensemble average of these $\mathcal{D}_k^c(u, x_1, ..., x_N)$ can be performed taking into account that the x_j's are independent random variables and that consequently the joint probability density, $p(x_1, ..., x_N)$, of detecting N photons between coordinates $x_1, ..., x_N$ and $x_1 + dx_1, ..., x_N + dx_N$ is the product of

the independent probability densities of having one photon detected between x_1 and $x_1 + dx_1$ times the probability density of detecting another photon between x_2 and $x_2 + dx_2$ and so on. Hence

$$p(x_1, ..., x_N)dx_1 ... dx_N = p(x_1).p(x_2).....p(x_N)\, dx_1 ... dx_N \tag{6}$$

where $p(x_j)$ is equal to the normalised intensity $\mathcal{I}_k(x_j)$ at coordinate x_j and frame k i.e.:

$$p(x_j) = \mathcal{I}_k(x_j) \tag{7}$$

Let c_k represent the true centroid shift vector at frame k. The function $\mathcal{I}_k(x_j)$ at frame k and coordinate x_j is related to the stationary normalised image $I(x_j)$ (Fig. 1) by

$$\mathcal{I}_k(x_j) = I(x_j - c_k) \tag{8}$$

As a consequence

$$\begin{aligned} p(x_j) &= \mathcal{I}_k(x_j) \\ &= I(x_j - c_k) \\ &= p(x_j, c_k) \end{aligned} \tag{9}$$

where $p(x_j, c_k)$ is a normalised probability density that depends both on x_j and on the random true centroid vector c_k.

The average of $\mathcal{D}_k^s(u, x_1, ..., x_N)$ over the ensemble of frames has therefore to be done in two steps: first averaging over the detected photon coordinates x_j and then over the true centroid vector c_k. Lets represent by $\bar{\mathcal{D}}_k^s(u, c_k)$ the result after averaging over $x_1, ..., x_N$.

$$\begin{aligned} \bar{\mathcal{D}}_k^s(u, c_k) &= \left\langle \mathcal{D}_k^s(u, x_1, ..., x_N) \right\rangle_{x_1, ..., x_N} \\ &= \int_{-\infty}^{+\infty} p(x_1, c_k)....p(x_N, c_k)\, \mathcal{D}_k^s(u, x_1, ..., x_N)\, dx_1....dx_N \\ &= \int_{-\infty}^{+\infty} I(x_1 - c_k).....I(x_N - c_k)\, \mathcal{D}_k^s(u, x_1, ..., x_N)\, dx_1.....dx_N \end{aligned} \tag{10}$$

Substituting (5) into (10) one get:

$$\begin{aligned} \bar{\mathcal{D}}_k^s(u, c_k) = \sum_{j=1}^{N} \int_{-\infty}^{+\infty} & I(x_1 - c_k)\, exp(+i2\pi u \cdot \frac{x_1}{N})\, dx_1 ..... \\ & ..... \int_{-\infty}^{+\infty} I(x_j - c_k)\, exp(-i2\pi u \cdot x_j[1 - 1/N])\, dx_j ..... \\ & ..... \int_{-\infty}^{+\infty} I(x_N - c_k)\, exp(+i2\pi u \cdot \frac{x_N}{N})\, dx_N \end{aligned} \tag{11}$$

The integrals in (11) can be evaluated easily giving:

$$\int_{-\infty}^{+\infty} I(x_j - c_k) exp(-i2\pi \vec{u} \cdot x_j) dx_j = exp(-i2\pi \vec{u} \cdot c_k)\, \tilde{I}(\vec{u}) \tag{12}$$

where $\bar{I}(\vec{u})$ is the Fourier transform of $I(\vec{r})$ and $\vec{u}$ can either be equal to $-u/N$ or to $+u[1-1/N]$.
Using result (12) the j^{th} term of the sum in (11) is:

$$
\begin{aligned}
&= \bar{I}(-u/N)\, exp(+i2\pi \frac{u}{N}\cdot c_k) \ldots\ldots \bar{I}(u[1-1/N])\, exp(-i2\pi \frac{N-1}{N} u\cdot c_k) \ldots\ldots \bar{I}(-u/N)\, exp(+i2\pi \frac{u}{N}\cdot c_k) \\
&= \bar{I}(u[1-1/N])\, exp(-i2\pi \frac{N-1}{N} u\cdot c_k) \quad \left[\bar{I}(-u/N)\right]^{N-1} \left[exp(+i2\pi \frac{u}{N}\cdot c_k)\right]^{N-1} \\
&= \bar{I}(u[1-1/N]) \quad \left[\bar{I}(-u/N)\right]^{N-1} \quad exp(+i2\pi \left[\frac{N-1}{N} - \frac{N-1}{N}\right] u\cdot c_k) \\
&= \bar{I}(u[1-1/N]) \quad \left[\bar{I}(-u/N)\right]^{N-1} \qquad (13)
\end{aligned}
$$

which is independent of j and c_k.
The evaluation of the sum over j can, therefore, be performed straightforwardly giving:

$$
\begin{aligned}
\bar{D}^k_N(u, c_k) &= \left\langle \bar{D}^k_N(u, x_1, \ldots, x_N) \right\rangle_{x_1,\ldots,x_N} \\
&= \sum_{j=1}^{N} \{\bar{I}(u[1-1/N]) \quad \left[\bar{I}(-u/N)\right]^{N-1}\} \\
&= N\, \bar{I}(u[1-1/N]) \quad \left[\bar{I}(-u/N)\right]^{N-1} \qquad (14)
\end{aligned}
$$

The result in (14) is independent of c_k and hence:

$$
\begin{aligned}
\bar{D}^s(u) &= \left\langle \bar{D}^k_N(u, c_k) \right\rangle_{c_k} \\
&= N\, \bar{I}(u[1-1/N]) \quad \left[\bar{I}(-u/N)\right]^{N-1} \qquad (15)
\end{aligned}
$$

It is convenient to introduce a normalised spectrum $\bar{Q}_N(u)$ defined as

$$
\bar{Q}_N(u) \equiv \frac{\bar{D}^s(u)}{N} \qquad \text{,yielding the important result}
$$

$$
\bar{Q}_N(u) = \bar{I}(u[1-1/N]) \quad \left[\bar{I}(-u/N)\right]^{N-1} \qquad (16)
$$

Expression (16) is a relationship between the normalised spectrum of the stationary image $\bar{I}(u)$ and the spectrum $\bar{Q}_N(u)$ of the centroided average of those frames containing exactly N photons/frame. The independence of (13) on c_k shows that $\bar{Q}_N(u)$ is a translating invariant quantity that depends only on the spectrum $\bar{I}$ and on the number of photons/frame N. As a consequence the quantity $\bar{Q}_N(u)$ is the same either for the randomly moving image as well as for the stationary image.

Equation (16) can be re-expressed in object space:

$$
\begin{aligned}
Q_N(r) &= \mathcal{F}^{-1}\{\bar{Q}_N(u)\} \\
&= \mathcal{F}^{-1}\{\bar{I}(\frac{N-1}{N}u) \quad \left[\bar{I}(-u/N)\right]^{N-1}\} \\
&= \mathcal{F}^{-1}\{\bar{I}(\frac{N-1}{N}u)\} \quad \otimes \quad \mathcal{F}^{-1}\{\left[\bar{I}(-u/N)\right]^{N-1}\} \\
&= \mathcal{F}^{-1}\{\bar{I}(\frac{N-1}{N}u)\} \otimes \\
&\qquad \otimes \underbrace{\mathcal{F}^{-1}\{\bar{I}(-u/N)\} \otimes \ldots\ldots \otimes \mathcal{F}^{-1}\{\bar{I}(-u/N)\}}_{(N-1)\ terms} \qquad (17)
\end{aligned}
$$

An examination of the above results for some particular values of N are instructive. For instance for $N = 2$ Eq.(16) reduces to

$$\begin{aligned} \bar{Q}_2(u) &= \bar{I}(\tfrac{u}{2}) \quad \bar{I}(-\tfrac{u}{2}) \\ &= \bar{I}(\tfrac{u}{2}) \quad \bar{I}^*(\tfrac{u}{2}) \\ &= \left|\bar{I}(\tfrac{u}{2})\right|^2 \end{aligned} \tag{18}$$

which is the power spectrum of $\bar{I}(u)$ where the variable u is scaled by a factor of 2. Fourier transforming $\bar{Q}_2(u)$ yields the scaled autocorrelation of the image $I(r)$.

For N=3

$$\begin{aligned} \bar{Q}_3(u) &= \bar{I}(\tfrac{2}{3}u) \quad \left[\bar{I}(-\tfrac{u}{3})\right]^2 \\ &= \bar{I}(\tfrac{2}{3}u) \quad \bar{I}(-\tfrac{u}{3})\,\bar{I}(-\tfrac{u}{3}) \end{aligned} \tag{19}$$

The above equation is related to the triple correlation[7-8] $I^{(3)}(x_1, x_2)$ defined for real functions as

$$I^{(3)}(x_1, x_2) = \int_{-\infty}^{+\infty} I(x)\, I(x + x_1)\, I(x + x_2)\, dx \tag{20}$$

and its Fourier transform $\bar{I}^{(3)}(u, v)$ known as the bispectrum

$$\bar{I}^{(3)}(u, v) = \bar{I}(u)\,\bar{I}(v)\,\bar{I}(-u - v) \tag{21}$$

It must be pointed out that for $u = \frac{2}{3}u$, $v = -\frac{1}{3}u$ or $u = -\frac{1}{3}u$, $v = \frac{2}{3}u$, which are representations of lines in the u,v plane, equation (21) reduces to (18).

Another limiting case is when $N \to \infty$. Remembering that $\bar{I}(u)$ has been normalised to unit at $u = 0$ it can be seen that:

$$\begin{aligned} \lim_{N\to\infty} \bar{Q}_N(u) &= \lim_{N\to\infty} \left\{ \bar{I}(u[1 - 1/N])\, \bar{I}(-\tfrac{u}{N})^{N-1} \right\} \\ &= \lim_{N\to\infty} \left\{ \bar{I}(u[1 - 1/N]) \right\} \times \lim_{N\to\infty} \left\{ \bar{I}(-\tfrac{u}{N})^{N-1} \right\} \\ &= \bar{I}(u) \end{aligned} \tag{22}$$

which is the normalised stationary image-spectrum.

3 - CENTROIDING PHOTON DATA

Experiments were carried out using simulated one dimensional photon data generated by a computer where the desired low-light level is achieved by selecting the value of the Poisson mean ($\bar{N}$) in the Poisson distribution of photons detected in each frame interval. In the particular simulation experiment described in this paper, we set $\bar{N} = 3$ photons/frame. Frames with 0 or 1 photon/frame are disregarded, because they do not carry any information concerning the intensity distribution of the image, and a total of 80,084 frames of a randomly translating image (of a binary star) containing $N \geq 3$ photons/frame were generated. These frames can be grouped in sets of frames containing a number of photons ranging from N=3 up to N=13 photons/frame in this case. The actual distribution for each value of N is shown in Table 1 for the photon-data used in this simulation.

For each particular set of N-photon frames, one should centroid the corresponding M_N frames, average(add) and divide by N to find the normalised image estimator $Q_N(r)$ and its Fourier transform $\bar{Q}_N(u)$:

$$Q_N(r) = \frac{1}{M_N N} \sum_{1}^{M_N} \{ \text{Frames with N photons/frame} \} \tag{23}$$

and

$$\bar{Q}_N(u) = \mathcal{F}\{Q_N(r)\} \tag{24}$$

Figure 2 depicts $Q_N(r)$ for N=2 up to N=13 photons/frame. For N=2 it can be seen that $Q_2(r)$ exhibits the same shape as the autocorrelation of the binary but distributed in a smaller (shrinked) region of space. It can also be seen that the average $Q_N(r)$ becomes more and more similar to the stationary image as N increases.

Frames containing more photons are bound to carry more information concerning the image than frames with a lesser number of photons. The limiting cases are those with no information content (N=0) and those with the image itself ($N \to \infty$). For instance frames with N=2 only carry information concerning the modulus of all possible distances within the stationary image whereas frames with N=3 photons/frame besides the modulus also carry information concerning the relative positions of points in the object giving therefore information about its structure. This fact allows one to use frames with at least N=3 photons/frame to reconstruct the image through the technique of triple correlation.

Accepting this idea one should give increased weight to those frames containing more photons. A possible way of implementing this is to construct an image estimator by adding, with equal weight, the quantities $Q_N(r)$ i.e. :

$$I^e_{weighted} = \frac{1}{\{\text{number of quantities } Q_N(r)\}} \sum_{N_{min}}^{N_{max}} Q_N(r) \tag{25}$$

In this particular case the 12 quantities, $Q_2(r)$, $Q_3(r)$,....., $Q_{13}(r)$, so formed are superimposed(averaged) forming the image estimator, $I^e_{weighted}$

$$I^e_{weighted} = \frac{1}{12} \sum_{N=2}^{13} Q_N(r) \tag{26}$$

The above procedure should be compared with the usual centroiding procedure. Let the total number of frames be $\mathcal{M} = \sum_N M_N$. The usual centroiding procedure would consist of averaging all centroided frames irrespective of the number of photons per frame N i.e.:

$$I^e_{usual} = \left\{\frac{1}{\mathcal{M}N}\right\} \sum_{\text{all frames}} \{\text{all frames irrespective of N value}\} \tag{27}$$

where $I^e_{usual}(r)$ is the usual centroided image estimate and $\mathcal{N} = \sum_{N=2}^{N=N_{max}} M_N N$ is the total number of photons of all $\mathcal{M}$ frames.

Figure 3b shows the result using the procedure given by Eq. (27), $I^e_{usual}(r)$, whereas Figure 3c shows $I^e_{weighted}$ obtained according to the procedure described by Eq. (25). Although $I^e_{weighted}$ is an improved estimate of the image further work has do be done concerning the way the quantities $Q_2(r)$, ..., $Q_N(r)$ should be added to form $I^e_{weighted}$ because, in the present case, although each frame used to build $Q_N(r)$, when N is larger, contains more structural information than a frame used to build $Q_N(r)$, when N is smaller, the number of frames with large N is smaller than the number of frames with small N.

4 - IMAGE RETRIEVAL FROM ONE-DIMENSIONAL CENTROIDED IMAGES - $Q_N(x)$

Applying Eq. (16) for real one dimensional images ($\bar{I}(-u) = \bar{I}^*(u)$) and changing $\frac{1}{N} \to u$ one gets:

$$\bar{Q}_N(N\,u) = \bar{I}(|N-1|u) \quad \left[\bar{I}^*(u)\right]^{N-1} \tag{28}$$

The randomly translating image is sampled at $\mathcal{L}$ bins equally spaced in the focal plane and the Fourier transforms $\bar{Q}_N(u)$ is therefore also sampled at $\mathcal{L}$ bins spaced by Δu. Each bin frequency can then be described as $u = k\,\Delta u$ where k = 0, 1, 2, ...,($\mathcal{L}$-1) allowing each sampled frequency to be described by its k value.

As $\bar{Q}_N(Nk)$, $\bar{I}(|N-1|k)$ and $\bar{I}(k)$ are complex quantities they can be written as:

$$\bar{Q}_N(Nk) = \left|\bar{Q}_N(Nk)\right| \exp\left(i\,\Theta_N(Nk)\right) \tag{29}$$

828 09

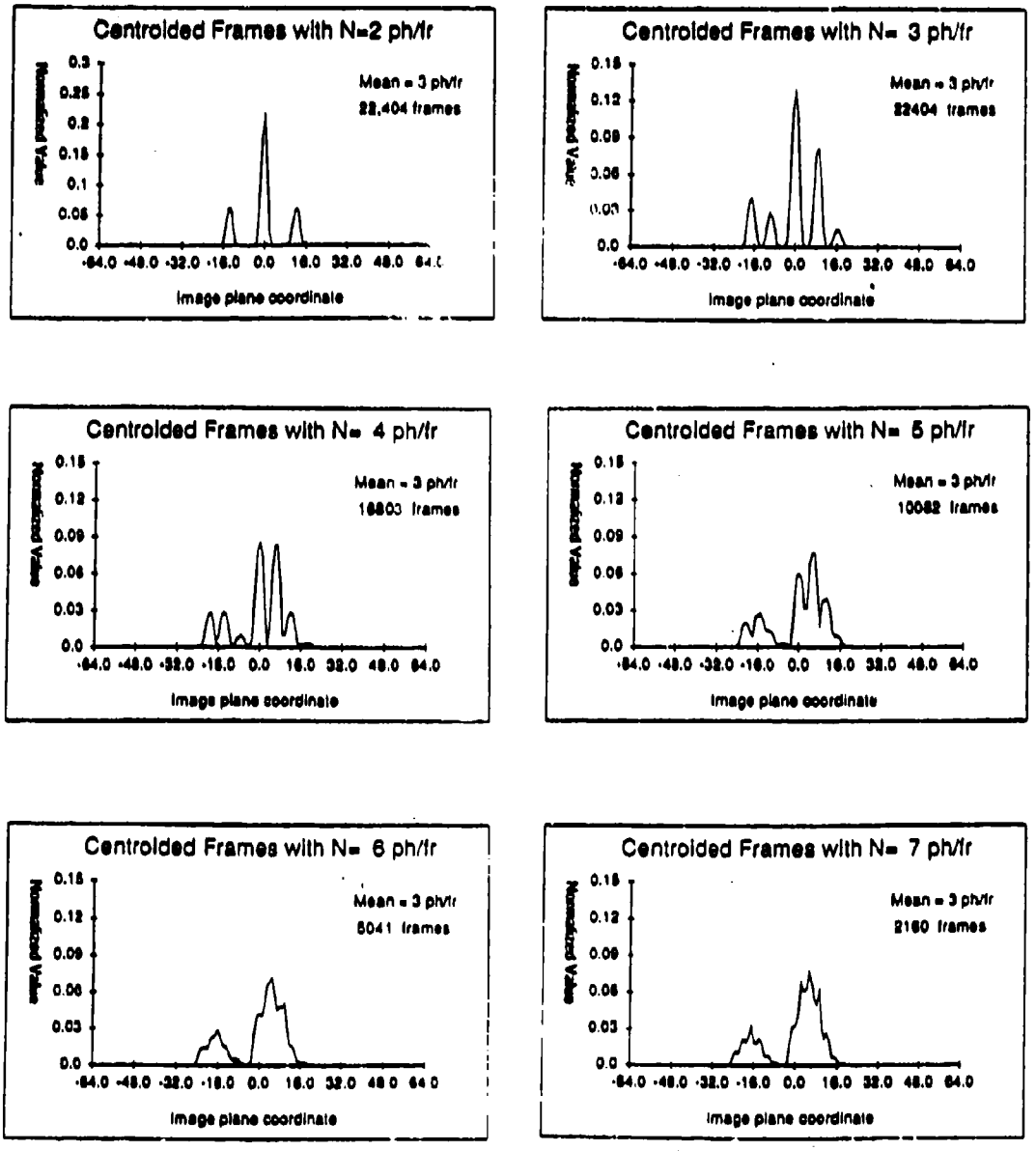

Figure 2 - Averaged Centroided Image Estimators $Q_N^{(r)}$

828 09

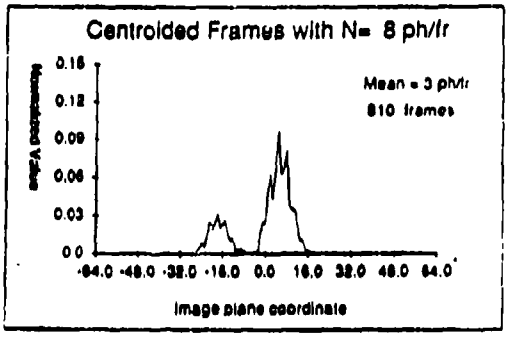

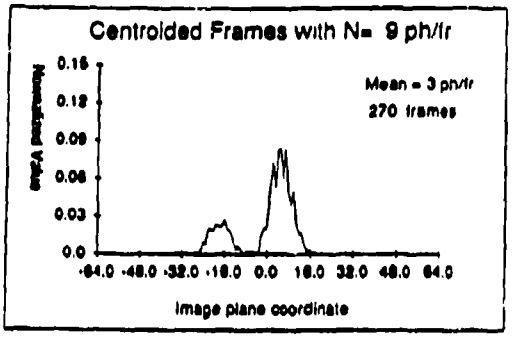

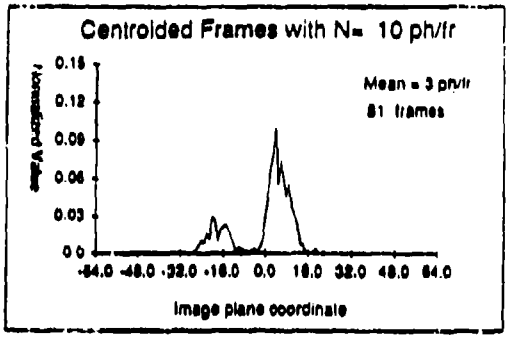

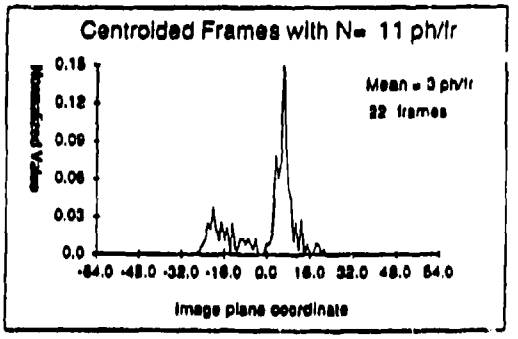

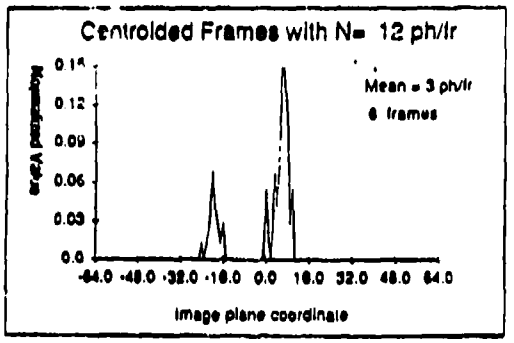

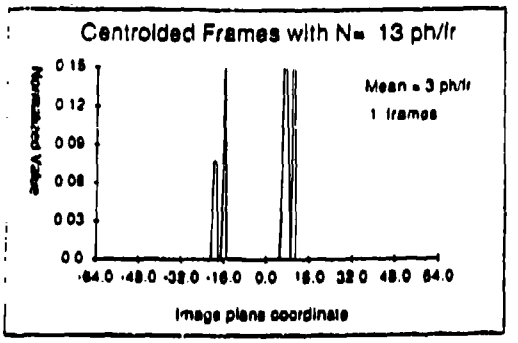

Figure 2 - continued

N	M_N	N	M_N	N	M_N
2	22404	6	5041	10	81
3	22404	7	2160	11	22
4	16803	8	810	12	6
5	10082	9	270	13	1

Table 1 - Number of frames, M_N, containing N photons/frame

$$\bar{Y}([N-1]k) = \left|\bar{Y}([N-1]k)\right| \exp\{i\,\phi([N-1]k)\} \tag{30}$$

$$\bar{Y}^*(k) = \left|\bar{Y}^*(k)\right| \exp\{-i\,\phi(k)\} \tag{31}$$

Substituting in (28):

$$\frac{\left|\bar{Q}_N(Nk)\right|}{\left|\bar{Y}([N-1]k)\right|\left|\bar{Y}^*(k)\right|} = e^{i(\phi([N-1]k)-(N-1)\phi(k)-\Theta_N(Nk))} \tag{32}$$

The left-hand-side being real ⇒

$$\Theta_N(Nk) = \phi([N-1]k) - (N-1)\phi(k) \tag{33}$$

Equation (31) is a recurrence relation linking phases at frequency k and $[N-1]k$ through the phase of the average quantity $\bar{Q}_N(Nk)$ and it can be seen that for N=2

$$\begin{aligned}\Theta_2(2k) &= \phi(k) - \phi(k)\\ &= 0\end{aligned} \tag{34}$$

and therefore no information about the phase can be retrieved. But for N=3 Eq.(31) becomes:

$$\Theta_3(3k) = \phi(2k) - 2\,\phi(k) \tag{35}$$

and hence from phase at frequency k one can reconstruct the phase at 2k up to $3k \leq \mathcal{L}/2 - 1$ where $\mathcal{L}$ is the actual number of bins used to sample $Q_2(r)$.

The method can be better understood through an example in which a one dimensional image is sampled at 32 points and therefore $\bar{Q}_N(Nk)$ is determined only at 32 frequency bins. Due to the fact that $\bar{Y}(-k) = \bar{Y}^*(u)$ one has to find the phases only in half the total number of bins and then reverse their sign. In this particular example one has, therefore, to consider only 16 frequency bins (Figure 4).

For k=0 the phase $\phi(0) = 0$. As $\bar{Q}_N(Nk)$ is shift-invariant one can always determine $\bar{Y}(k)$ apart from a constant phase shifting factor. By appropriately choosing this factor one can always set the phase at $\phi(1) = 0$. From then on by successively applying the recurrence relations (33), for each $\bar{Q}_N(Nk)$, one reconstructs all the phases by using averages of frames with N up to 16.

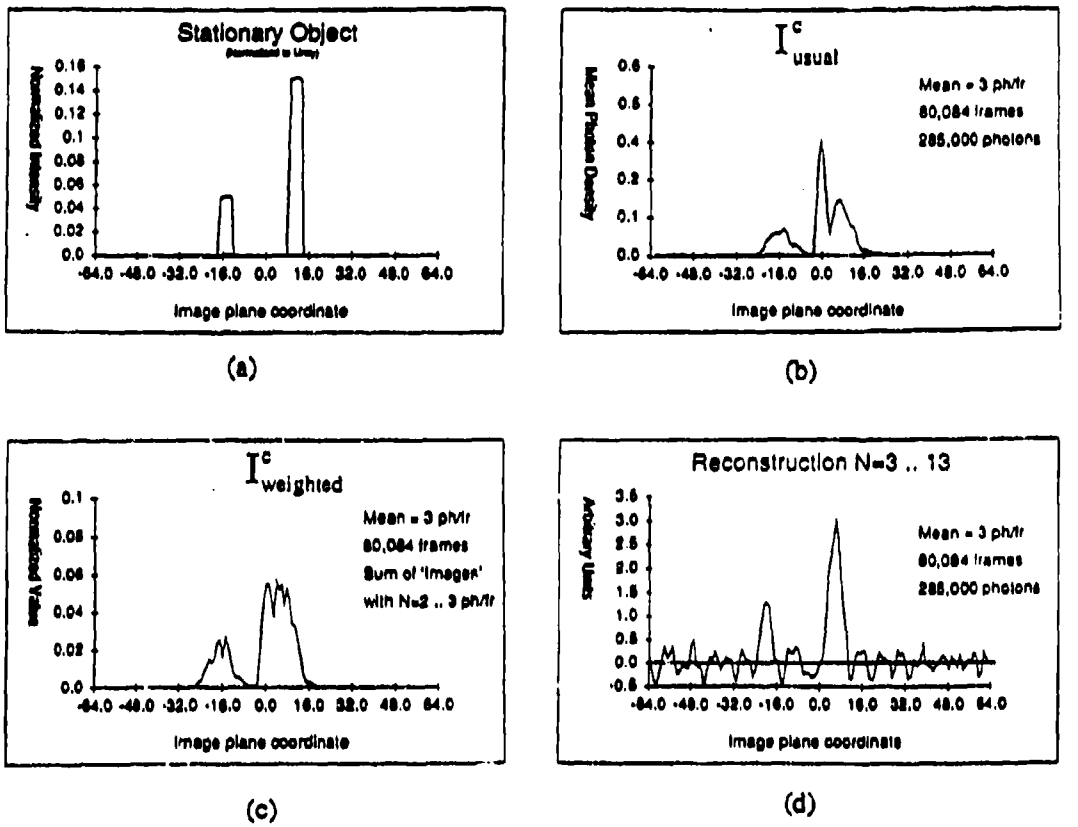

Figure 3 - Comparison between the object, I^c_{usual} , $I^c_{weighted}$ and the Reconstruction.

Using N=3 ph/fr and departing from $\phi(1)$ one gets the phase at 2 using $\Theta_3(3)$; from $\phi(2)$ one gets $\phi(4)$ using $\Theta_1(6)$; from $\phi(4)$ one gets $\phi(8)$ using $\Theta_9(12)$ but from $\phi(8)$ this recurrence relation can not be applied anymore because it would give us the phase at $\phi(16)$, which does not exist, through the use of the phase $\Theta_3(24)$ which also does not exist.

For N=4 ph/fr the recurrence relation (33) becomes:

$$\Theta_4(sk) = \phi(3k) - 3\,\phi(k) \tag{36}$$

Departing from $\phi(1)$ and using the same procedure described for the case of N=3 ph/fr one finds $\phi(3)$, $\phi(6)$ and $\phi(9)$.

In general, for a frequency bin k, where k is a prime number, one can only reconstruct its phase by using an average $\bar{Q}_N(Nk)$ such that N=k+1 photons/frame. In this particular example to reconstruct the phases up to bin 15 one needs averages of frames with N up to 16 photons/frame. The modulus of $\bar{I}(k)$ is found from the Fourier transform of the auto correlation function, the power spectrum $\left|\bar{I}(u)\right|^2$.

Figure 3d shows the reconstructed image obtained using this method with $\mathcal{L} = 128$ bins and using frames with N only up to 13 ph/frame i.e. not all the frequencies were reconstructed. Despite the fact that no other image processing technique has been used, e.g. enforcing positivity, Fig. 3d, nevertheless, gives a good estimate of the image and in this particular case also a good estimate of the relative brightness of the stars.

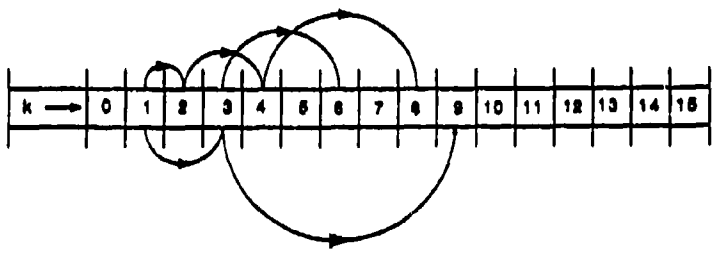

Figure 4 - Pictorial representation of the phase reconstruction algorithm

5 - CONCLUSIONS AND FUTURE WORK

The results show that centroiding, although a very simple and computationally fast technique, can be used to retrieve an image of a randomly translating object at very low light level.

Future work could address the following:

(i) how to combine the $Q_N(r)$ in an optimum way;
(ii) extend the phase retrieval algorithm to two dimensions and
(iii) apply the technique to speckled imaging.

6 - ACKNOWLEDGMENTS

The authors wishes to thank G. Ayers for providing the simulation program and valuable help in implementing the algorithm. LOF is funded by The British Council and CNPq - Brasil on leave from Departamento de Física - Univ. Fed. Mato Grosso do Sul - P.O. Box 649 - 79.100 - Campo Grande - MS - Brasil. The research is supported by the U.K. Science and Engineering Research Council - S.E.R.C. under grant GR/D 92332 and the U.S. Army under Contract DAJA 45-85-C-0028.

7 - REFERENCES

1 - C.R. Lynds, S.P. Worden and J.W. Harvey, Ap. J., 207, 174(1976).

2 - S.P. Worden, C.R. Lynds and J.W. Harvey, JOSA, 66, 1243(1976).

3 - R.H.T. Bates, M.O. Milner, G.I. Lund and A.D. Seagar, Opt. Comm., 20, 22(1978).

4 - R.H.T. Bates and F.M. Cady, Opt. Comm., 32, 365(1980).

5 - F.M. Cady and R.H.T. Bates, Opt. Lett., 5, 438(1980).

6 - J.W. Goodman and J.F. Belsher, "*Photon Limited Images and Their Restoration*" Technical Report RADC-TR-76-50 (March 1976); "*Precompensation and Postcompensation of Photon Limited Degraded Images*", Technical Report RADC-TR-76-382 (December 1976); "*Photon Limitations in Imaging and Image Restoration*", Technical Report RADC-TR-77-178 (May 1977) (all available from Rome Air Development Center, Griffiss AFB, NY 13441.

7 - A.W. Lohmann, G. Weigelt and B. Wirnitzer, Appl. Opt., 22, 4028(1983).

8 - A.W. Lohmann and B. Wirnitzer, Proc. IEEE, 72, 889(1984).

REF 7

Knox-Thompson and Triple Correlation Imaging Through Atmospheric Turbulence

G.R. Ayers, M.J. Northcott, J.C. Dainty

Optics Section
Blackett Laboratory
Imperial College, London SW7 2BZ
UK

ABSTRACT

A comparative study has been made of the Knox-Thompson method and triple correlation techniques as applied to image restoration. Both photon noise degraded and atmospheric turbulence degraded imaging have been considered. The signal-to-noise ratios of the methods have been studied analytically and with the aid of computer simulations. The ability to retain diffraction limited information on imaging through turbulence is considered in terms of phase closure relationships. On the basis of this work it is found that both image restoration techniques are effectively equivalent.

November 1987

INTRODUCTION

The problem of imaging through turbulent media has been studied for many years. Of particular interest here is the imaging of objects through atmospheric turbulence. A detailed description of this effect is given by Roddier [1].

As atmospheric conditions are continuously varying the ultimate resolution obtainable, from conventional long exposure imaging using a large telescope, is severely limited by turbulence effects. However, if short exposure, narrow optical bandwidth, images are recorded atmospheric induced wavefront perturbations may be 'frozen'. The turbulence-imposed resolution limit is therefore removed allowing diffraction limited resolution to be obtained.

It is well known that this type of imaging of a point source object results in a speckled image due to interference effects. This is a consequence of the complex amplitude in the pupil of the imaging optics consisting of typically many uncorrelated regions, 'seeing cells', the size scale [2], r_o, of these regions increasing as atmospheric conditions improve. The long exposure angular resolution limit imposed is approximately, r_o/λ, which is typically very much less than the diffraction limit, D/λ, of a telescope of diameter, D.

The technique of speckle interferometry [3] utilises the diffraction limited information present in short exposure images to obtain the spatial autocorrelation of astronomical objects even in poor 'seeing', at very low light levels and in the presence of telescope aberrations [4]. During the past 15 years, a large number of speckle imaging techniques have been proposed, see reference [5] for further details, although none are in routine use. Two of the more promising techniques are the method of Knox and Thompson (KT) [6],[7] and a method first suggested by Weigelt et al [8]-[10] which uses the concept of triple correlation (TC).

Both techniques are analogous to speckle interferometry as they involve averaging correlation functions of many short exposure images. Additionally, as a consequence of 'phase closure' [11], all three techniques possess transfer functions which allow diffraction limited information to be obtained even if r_o is very small. In addition to the Fourier modulus, the KT and TC methods allow direct recovery of the Fourier phase of an object's intensity distribution from their associated ensemble averaged correlation functions. If the spatial autocorrelation of the object alone is known then

such phase information is potentially only obtainable through indirect methods [12] and by making assumptions concerning the object's intensity distribution. For both the KT and TC methods, rigorous analyses [13], [14] show that an object's intensity distribution is uniquely related, apart from trivial ambiguities, to the relevant averaged quantity in each case (although there is no guarantee that current algorithms reconstruct this unique intensity distribution, particularly in the presence of noise).

Although these correlation techniques make available diffraction limited information, its quality must be assessed before it can be used effectively. A common measure of quality used is the signal to noise ratio, SNR, at each spatial frequency, $\mathbf{u}$, in the Fourier transform, $\langle S(\mathbf{u})\rangle$, of the particular average correlation being considered. The SNR measure can be defined as

$$SNR = \frac{|\langle S(\mathbf{u})\rangle|}{\sigma_S},$$

where σ_S is the standard deviation of the signal $S(\mathbf{u})$. This allows similar techniques to be compared and additionally gives the relative weight of the information present so that it can be used optimally.

A consequence of using short exposure times and the low luminosity of many astronomical objects of interest, is that very few photon events are recorded in individual speckle images. Photon noise is therefore introduced which can seriously lower the obtainable SNR and as a result degrade reconstructed image quality. Despite such noise, the correlation techniques have been succesfully used to study low luminosity astronomical objects, for example see reference [15].

The aim of this paper is to compare and relate the KT and TC methods with particular reference to the SNR's of their assosciated averaged correlations. The evaluation of the SNR's requires the ensemble average of many different image correlations to be carried out over both the Poisson statistics of the photon events and the statistics of atmospheric turbulence effects. Fortunately, recent work [16],[17] has assosciated the much used idea of 'phase closure' in radio astronomy with the comparatively new ideas of triple correlations and 'phase closure' pupil plane interferometry as used in the optical and infra-red wavebands. This assosciation can be extended and generalised to allow, previously very difficult, ensemble averages of many different image correlations to approximated on the basis of phase closure relationships.

The effect of photon noise on speckle interferometry was originally investigated by Goodman and Belsher [18], their work being extended by Dainty and Greenaway [19] with particular reference to the problem of photon bias. The latter is a consequence of correlating photon events with themselves and is present in both the KT and TC average signals. Evaluation of the ensemble average signals has been facilitated by the development of computationally very efficient photon coordinate differencing algorithms, [20], together with modern photon detectors, such as the PAPA detector [21] which returns a stream of time tagged photon coordinates. Use of the time tag information enables increased SNR to be obtained [28]. Previous work, [22]-[24], on the effect of photon noise and atmospheric turbulence has been carried out for the KT and TC techniques. However, only very simplified approximations to ensemble averages of image correlations over the photon noise and atmospheric statistics have been obtained. Previous studies have also only been concerned with very specific regions in Fourier space of the ensemble averaged signals, the work on the TC being only concerned with regions having the lowest SNR which are infact not used in practice [25]. The work on the KT method has only looked at the basic two dimensional correlation technique as originally proposed [6], whereas the technique can be completely generalised to give a four dimensional average signal that contains considerably more information and is analogous to the four dimensional TC signal.

The present work is organised as follows. In section 2 the mathematical form of the TC, the KT correlation and the autocorrelation are defined in both image and Fourier space. A formalism for the TC is put forward which allows it to be simply related, in image space, to the KT correlation. The correlation techniques are seen diagramatically and mathematically to be intimately related, each being simply correlations of images with themselves weighted by complex exponentials. Additionally, a further technique [26],[27], known as the phase gradient method, is included which is shown to be a sub-set of the more general KT.

In section 3 the implementation of the correlation techniques at low light level is described. Of particular importance is the development of a differencing algorithm which allows individual sections or sub-planes of the Fourier transform of the TC, known as the bispectrum, to be evaluated, the full TC differencing algorithm being reduced to a weighted KT implementation. This has the advantage that only the higher SNR regions need be calculated as opposed to the whole of the bispectrum which is evaluated if a full differencing algorithm is implemented. This problem can be

overcome by evaluating the required bispectrum planes directly in Fourier space. This however requires each frame to be Fourier transformed which becomes less efficient relative to photon differencing at low light levels.

The effect of photon noise on SNR's is considered in section 4. An estimate for the error on the phase of a complex signal is proposed and its dependency on photon noise studied for the KT and TC signals. The phase error estimate is shown to be related to the SNR. Averaging various image correlations over the photon statistics has been facilitated by a computer implementation of a generalisation of the method of Goodman and Belsher [18]. It has therefore been possible to extend the work on photon noise dependency.

Section 5 briefly considers the imaging of a randomly translating object. The necessity to centroid frames before carrying out the KT processing is explained and also the problems associated with centroiding images in the presence of photon noise.

In section 6 the use of the KT and TC for imaging through atmospheric turbulence is studied. The diffraction limited information present in the transfer functions of speckle interferometry, the KT and the TC is seen to be a direct consequence of the concept of phase closure. Extensive use has been made of a computer simulation of the imaging of objects through atmospheric turbulence using a large telescope. The dependency of SNR's and transfer functions on mean number of photon events per image, $\overline{N}$, and mean number of speckles per image, $\overline{n}_s$ is studied analytically and via Monte-Carlo type computer simulations.

Finally, in section 7 results are compared and conclusions drawn as to the relative merits of the speckle imaging techniques with respect to the areas studied.

2. Definitions and relationships

Consider a two dimensional intensity distribution, $i(x)$, and its Fourier transform, $I(u)$, defined by

$$I(u) = \int_{-\infty}^{+\infty} i(x)\, exp(-2\pi/ux)\, dx\,. \tag{1}$$

Both the triple correlation (TC), [8]-[10], and the correlation of Knox and Thompson (KT), [6][7], may be defined in image space as correlations of $i(x)$, or in Fourier space as products of $I(u)$. The TC and its Fourier transform, the bispectrum, are defined by

$$i^{TC}(x_1,x_2) = \int_{-\infty}^{+\infty} i^*(x)\, i(x+x_1)\, i(x+x_2)\, dx \tag{2}$$

$$I^{TC}(u_1,u_2) = I(u_1)\, I^*(u_1+u_2)\, I(u_2)\,. \tag{3}$$

In an analogous way the KT double correlation and its Fourier transform are defined by

$$i^{KT}(x_1,\Delta u) = \int_{-\infty}^{+\infty} i^*(x)\, i(x+x_1)\, exp(2\pi/\Delta u x)\, dx \tag{4}$$

$$I^{KT}(u_1,\Delta u) = I(u_1)\, I^*(u_1+\Delta u)\,, \tag{5}$$

where $x_1=x_{1x}+x_{1y}$ and $x_2=x_{2x}+x_{2y}$ are two dimensional spatial coordinate vectors, $u_1=u_{1x}+u_{1y}$, $u_2=u_{2x}+u_{2y}$ and $\Delta u=\Delta u_x+\Delta u_y$ are two dimensional spatial frequency vectors, and the superscript * indicates the complex conjugate. The x and y subscripts denote orthogonal component vectors.

It is apparent that Eqs.(1)-(5) are four dimensional. This fact causes implementation problems, extensive evaluation time and data storage requirements, particularly if the correlations are performed using digitized images on a computer. The basic KT technique does, however, only consist of evaluating the three sub-planes in Fourier space corresponding to $\Delta u=\Delta u_x$, $\Delta u=\Delta u_y$, and $\Delta u=\Delta u_y+\Delta u_x$, with the Δu vector components having constant values. If digitized images are used then Δu normally [7] corresponds to the fundamental sampling vector interval. Further, different values of Δu may be used and a number of sub-planes can be evaluated. This is analogous to the

many sub-planes contained in the four dimensional bispectrum, see Fig.1.

The relationships between the two methods become more apparent if Eq.(2) is rewritten, making the substitution $u_2 = \Delta u$. A single plane of the bispectrum can therefore be described by

$$I^{TC}(u_1,\Delta u) = I(u_1)\, I^*(u_1+\Delta u)\, I(\Delta u)\,. \tag{6}$$

The corresponding image space expression is obtained by inverse Fourier transforming yielding the double correlation

$$i^{TC}(x_1,\Delta u) = I(\Delta u) \int_{-\infty}^{+\infty} i^*(x)\, i(x+x_1)\, exp(2\pi/\Delta u x)\, dx$$

$$= I(\Delta u)\, i^{KT}(x_1,\Delta u)\,. \tag{7}$$

On comparing equations (5) and (6) it can be seen that for a fixed spatial frequency difference, Δu, the defined bispectrum plane corresponds to a weighted version of the KT product in Fourier space. The complex weighting factor is, however, signal dependent and as such possesses a number of important properties which will become evident in later sections.

In order to understand the correlation techniques it is instructive to consider the autocorrelation process. This corresponds to the double correlation represented by Eq.(4) with the substitution $\Delta u = 0$. The resulting representations in the image and Fourier domains are

$$i^A(x_1) = i^{KT}(x_1, 0) = \int_{-\infty}^{+\infty} i^*(x)\, i(x+x_1)\, dx \tag{8}$$

$$I^A(u_1) = I^{KT}(u_1, 0) = I(u_1) I^*(u_1)\,. \tag{9}$$

The autocorrelation of $i(x)$ is the correlation of $i(x)$ and $i(x)$ multiplied by a complex exponential factor with zero spatial frequency, see Fig.2(a). Unfortunately the complete spatial symmetry of the operation prevents the preservation of Fourier phase information. The argument of Eq.(9) is always zero,

$$arg\left\{I^A(u_1)\right\} = \Phi^A(u_1) = \phi(u_1) - \phi(u_1) = 0\,, \tag{10}$$

where $\phi(u)$ is the phase of $I(u)$, and $arg\{\}$ defines the phase of the complex number

modulo 2π .

Now consider the KT correlation of Eq.(4). This defines the correlation of $i(x)$ and $i(x)$ multiplied by a complex exponential factor with spatial frequency greater than zero, see Fig.2(b). For sampled images this generally corresponds to the fundamental spatial frequency. The KT correlation enables Fourier phase difference information to be retained. The argument of Eq.(5),

$$arg\left\{I^{KT}(u_1,\Delta u)\right\} = \Phi^{KT}(u_1,\Delta u) = \phi(u_1) - \phi(u_1+\Delta u) , \tag{11}$$

gives the phase difference between two spatial frequencies separated by the vector Δu.

The TC of Eq.(7) similarly allows the retention of phase difference information. However, absolute spatial position is indeterminable due to the property of the complex weighting factor that linear phase is cancelled. Additionally, bispectrum planes contain phase information encoded by correlating $i(x)$ with $i(x)$ multiplied by complex exponentials with higher spatial frequencies, for an example see Fig.2(c). The argument of Eq.(3),

$$arg\left\{I^{TC}(u_1,u_2)\right\} = \Phi^{TC}(u_1,u_2) = \phi(u_1) - \phi(u_1+u_2) + \phi(u_2) , \tag{12}$$

allows the phase difference between two spatial frequencies separated by the vector Δu to be determined provided the phase at frequency $u_2 = \Delta u$ is already known. In particular, for $u_2 = \Delta u$ and Δu equal to the fundamental sampling frequency in the case of discrete data, the TC gives identical phase difference information as the KT apart from the phase at Δu . This is the linear phase which cancels with the linear phase in the KT phase difference to produce the shift invariant property of the bispectrum,

$$\Phi^{TC}(u_1,\Delta u) = \Phi^{KT}(u_1,\Delta u) + \phi(\Delta u) . \tag{13}$$

Another processing technique, the phase-gradient method of Aitken et al, [26][27], is very closely related to the correlations just described. Phase information is again retained but in the form of its derivative, not explicit phase differences. The phase derivative information is contained in the imaginary part of a double product in Fourier space,

$$I^{PG}(u_1,a) = \left(IMAG\left\{I(u_1)\, I^*(u_1)\right\} \right) \frac{a}{\pi}$$

$$= (\; | I(u_1) |^2 \, \phi'(u_1) \;) \, \frac{a}{\pi} \, , \tag{14}$$

where $IMAG\{\}$ indicates the imaginary part, $\phi'(u)$ is the phase derivative, $I'(u)$ is the derivative of $I(u)$ and a is a vector gradient in image space. The result can be achieved through image space in a number of ways. For example, the following two simple correlations may be performed,

$$I^{PG}(x_1, +a) = \int_{-\infty}^{+\infty} I^*(x) \, i(x+x_1) \, [+a.x + b] \, dx \quad \text{and}$$

$$I^{PG}(x_1, -a) = \int_{-\infty}^{+\infty} I^*(x) \, i(x+x_1) \, [-a.x + b] \, dx, \tag{15}$$

where b is a real constant, and then combined and Fourier transformed to yield the result of Eq.(14). This is similar to the optical implementation of the technique used by Aitken et al,

$$I^{PG}(u_1,a) = \left[FT\left\{ I^{PG}(x_1, -a) \right\} \right]^* - FT\left\{ I^{PG}(x_1, +a) \right\}$$

$$= (\; \left[I'(u_1) \, I^*(u_1) \right]^* - I'(u_1) \, I^*(u_1) \;) \, \frac{a}{2\pi}$$

$$= (\; IMAG\left\{ I'(u_1) \, I^*(u_1) \right\} \;) \, \frac{a}{\pi}$$

$$= (\; | I(u_1) |^2 \, \phi'(u_1) \;) \, \frac{a}{\pi} \, , \tag{16}$$

The expressions of Eq.(15) correspond to correlations of $i(x_1)$ with $i(x_1)$ multiplied by linear ramp functions of opposite gradient, see Fig.2(d).

This technique is analogous to the KT with a Δu value such that there is only a linear fluctuation of phase over that distance. This corresponds to the complex exponential in the KT correlation of Eq.(4) having a spatial frequency, Δu, such that the image being correlated only extends over the linear region of the exponential. The imaginary part of the KT product in Fourier space therefore gives the phase difference between spatial frequencies Δu apart. Obviously division by Δu now yields, apart from a constant factor, the weighted phase gradient contained in the result of Eq.(14).

$$IMAG\left\{I'(u_1)\, I^*(u_1)\right\} = -\frac{1}{\Delta u}\, IMAG\left\{I^{KT}(u_1,\Delta u)\right\}_{\Delta u \to 0}$$

$$= -\frac{1}{\Delta u}\, IMAG\left\{I(u_1)\, I^*(u_1+\Delta u)\right\}_{\Delta u \to 0}$$

$$= -\frac{1}{\Delta u}\, IMAG\left\{I(u_1)\,[\, I(u_1) + I'(u_1)\,\Delta u\,]^*\right\}$$

$$\approx |\, I(u_1)\,|^2\, \phi'(u_1)\,. \qquad (17)$$

3. Implementation of correlation techniques at low light level

In a number of situations, for example 'freezing out' turbulence effects on imaging through the atmosphere, it is desirable to record many short exposure images. As a result, very few photon events are detected in individual images. However, it can be shown that apart from removable photon bias terms, one of the properties common to all the correlation techniques is that the ensemble average over many low light level frames is equivalent to the high light level correlation. At such low photon levels it is more efficient computationally to perform the correlations in image space via photon differencing algorithms rather than in Fourier space via fast Fourier transform routines and multiple products.

Using the notation of Dainty and Greenaway, [19], the pth photon limited image is represented by a sum of Dirac delta functions positioned at the coordinates of the N_p photon events,

$$d_p(\mathbf{x}) = \sum_{k=1}^{N_p} \delta(\mathbf{x}-\mathbf{x}_{pk}) \tag{18}$$

and its Fourier transform

$$D_p(\mathbf{u}) = \sum_{k=1}^{N_p} \delta(\mathbf{x}-\mathbf{x}_{pk}) \ \exp(-2\pi i \mathbf{u}\mathbf{x}) \ , \tag{19}$$

where $\mathbf{x}_{pk}$ is the position vector of the kth photon in the pth frame.

The photon differencing algorithm for the KT can be written as, [20],

$$I^{KT}(\mathbf{x}_1,\Delta\mathbf{u}) = \sum_{k_1=1}^{N_p} \sum_{k_2=1}^{N_p} \delta(\mathbf{x}_{pk_2} - \mathbf{x}_{pk_1} + \mathbf{x}_1) \exp(2\pi i/\Delta\mathbf{u}\mathbf{x}_{pk_1}). \tag{20}$$

Thus the KT correlation for each image is carried out by placing the complex number $\exp(2\pi i/\Delta\mathbf{u}\mathbf{x}_{pk_1})$ at position $\mathbf{x} = \mathbf{x}_{pk_1}-\mathbf{x}_{pk_2}$ whenever this vector coordinate difference occurs between two photon events. The same algorithm can be used to obtain the autocorrelation but with the substitution $\Delta\mathbf{u}=0$.

There are many approaches to obtaining the TC, [28], but a differencing algorithm based on Eq.(7) is most appropriately stated here. That is, each bispectrum plane corresponding to a different $\Delta\mathbf{u}$ value is evaluated independently using the following expression

$$i^{TC'}(x_1,\Delta u) = \sum_{k=1}^{N_p}\delta(x_1-x_{pk})\exp(-2\pi/\Delta u x_{pk}) \cdot \sum_{k_1=1}^{N_p}\sum_{k_2=1}^{N_p}\delta(x_{pk_2}-x_{pk_1}+x_1)\exp(-2\pi/\Delta u x_{pk_2}). \quad (21)$$

Thus the correlation is reduced to the simpler KT differencing algorithm followed by a single complex multiplication and hence requires very little additional computation time.

The phase gradient correlations of equation (15) can be evaluated using

$$i^{PG}(x_1,a) = \sum_{k_1=1}^{N_p}\sum_{k_2=1}^{N_p}\delta(x_{pk_2}-x_{pk_1}+x_1)\,(ax_{pk_2}+b). \quad (22)$$

Photon bias terms

The ensemble averaging of photon limited correlations unfortunately introduces photon bias terms. Such terms correspond to the correlation of photon events with themselves and do not contribute any useful information to the average. The elimination of bias terms is simply carried out by not including in the differencing algorithms any differences between a photon event and itself. Therefore Eqs.(20) and (22) should include the proviso that $k_1 \neq k_2$ and equation (21) is modified to read

$$i^{TC'}(x_1,\Delta u) = \sum_{k=1,k\neq k_1,k\neq k_2}^{N_p}\delta(x_1-x_{pk})\exp(-2\pi/\Delta u x_{pk}) \cdot \sum_{k_1=1,k_1\neq k_2}^{N_p}\sum_{k_2=1,k_2\neq k_1}^{N_p}\delta(x_{pk_2}-x_{pk_1}+x_1)\exp(-2\pi/\Delta u x_{pk_2}) \quad (23)$$

It is important to note, from the standpoint of photon noise analysis, that the bias terms of <u>each frame</u> [19], are removed during processing and not the ensemble average bias terms.

The unbiased quantities averaged in each technique may be stated in Fourier space as follows.

(a) The autocorrelation :

$$D_p(u_1)\,D_p^*(u_1) - D_\mu(0). \quad (24)$$

(b) The Knox-Thompson

$$D_p(u_1)\, D_p^*(u_1+\Delta u) - D_p^*(\Delta u). \tag{25}$$

(c) The triple correlation for each bispectrum plane $u_2=\Delta u$

$$D_p(u_1)\, D_p^*(u_1+\Delta u)\, D_p(\Delta u) - |D_p(u_1)|^2 - |D_p(u_1+\Delta u)|^2 - |D_p(\Delta u)|^2 + 2N_p. \tag{26}$$

(d) The phase gradient correlation

$$\frac{-1}{2\Delta u}\left[D_p(u_1)\, D_p^*(u_1+\Delta u) - D_p^*(\Delta u) - D_p^*(u_1)\, D_p(u_1+\Delta u) + D_p(\Delta u) \right]. \tag{27}$$

The variance of the above quantities with the number and distribution of photon events in each image describes the effect of photon noise on such correlation techniques.

4. Photon noise

With the exception of the autocorrelation the aim of the techniques under study is primarily to preserve some estimate of the Fourier phase. As the averages are complex numbers both the variance of the real, σ_R^2, and imaginary part, σ_I^2 of the Fourier transform are studied, together with the covariance of the real and imaginary parts, $Cov(I,R)$. Previously, [22],[23], the signal to noise ratio, SNR, measure used corresponds to,

$$SNR_m = \frac{|\text{ mean signal }|}{\text{standard deviation of signal}} \sqrt{M}$$

$$= \frac{|\langle S \rangle|}{\sigma_m} \sqrt{M} \tag{28}$$

where $\sigma_m = \sqrt{\sigma_R^2 + \sigma_I^2}$, and M is the number of independent realisations used. This measure provides a reasonable indication of the SNR; however, of concern here is the error on the phase of the complex signal. An estimate of the phase error, Θ_E, may be be found by considering the variance of the signal in a direction perpendicular to the mean signal.

$$\tan \Theta_E = \frac{\sqrt{\sigma_I^2 \cos^2 \phi + \sigma_R^2 \sin^2 \phi - Cov(I,R) \sin 2\phi}}{|\langle S \rangle|} \frac{1}{\sqrt{M}} \tag{29}$$

where ϕ is the argument of the mean complex signal, $\langle S \rangle$. Provided the number of realisations, M, used to obtain the mean signal is large, then then the small angle approximation of the tangent may be used to yield the phase error estimate directly.

$$\Theta_E \approx \frac{\sqrt{\sigma_I^2 \cos^2 \phi + \sigma_R^2 \sin^2 \phi - Cov(I,R) \sin 2\phi}}{|\langle S \rangle|} \frac{1}{\sqrt{M}} \tag{30}$$

The σ_m^2, σ_I^2, σ_R^2 and the covariance, $Cov(I,R)$, of all the unbiased estimated quantities, Eqs.(24)-(27), have been evaluated where appropriate, see Appendix(1). The method of evaluation is a computer implementation of a generalisation of the method described by Goodman and Belsher, [18], for the power spectrum. The evaluated variances are now used to compare the effect of photon noise on the correlation techniques.

The effect of photon noise on power spectrum estimation has been adequately studied by other authors, [18], [20]. Of particular interest in this work is the comparison of photon noise sensitivity of phase difference estimates obtained using the KT and the TC techniques. It is apparent from the relationships described in section(2) that the KT and TC sub-planes may be directly compared as they effectively yield the same information. The additional term present in each bispectrum sub-plane is in general known from sub-planes defined by a smaller magnitude frequency vector, u_2. However, the bispectrum, being an average of a triple product, contains noise terms to the third power causing the variance of the observed signal to be greater than that of the KT double product. This is a basic property of high order correlations and suggests the use of correlations of the lowest order possible which allow recovery of the same information. For example, Fig.3(a) shows the theoretical error, Θ_E, for a single image, on the phase difference estimates resulting from using the KT plane (u_{1y}=0, Δu_y=0) and the bispectrum plane (u_{2x}=Δu_x, u_{1y}=u_{2y}=0). The results are for an 'asteroid' type object, see Fig.3(c), which is approximately 10 x 20 pixels in a sampled region of 128 x 128 pixels, and an imaging system with a transfer function of value unity for all spatial frequencies. The mean number of photons per frame, $\bar{N}$, is 10. Cross-sections through these planes are shown in the graph of Fig.4(a), corresponding to Δu_x=u_{2x}=4, i.e. 4 times the frequency sampling interval. The signal to noise ratio, SNR_m, for the same two planes, are shown in Fig.3(b). If cross-sections through these plots are compared, for example Fig.4(b) shows the SNR of the KT section Δu_x=4 and Δu_y, u_{1y}=0) and the bispectrum (u_{2x}=4 and u_{2y}=u_{1y}=0, a further indication of the advantage of the double product estimation is obtained.

As a second example, consider estimating the mean number of photons per frame using the bispectrum element u_1=u_2=0 and the KT element u_1=Δu=0. The SNR for a single frame for the KT is

$$SNR_{KT} = \frac{\bar{N}^2}{\sqrt{4\bar{N}^3 + 2\bar{N}^2}} \tag{31}$$

and for the bispectrum is

$$SNR_{TC} = \frac{\bar{N}^3}{\sqrt{9\bar{N}^5 + 18\bar{N}^4 + 6\bar{N}^3}}. \tag{32}$$

It is apparent that the KT has a greater SNR then the bispectrum at this point for all values of $\bar{N}$. In particular, for the limiting cases of $\bar{N}$ approaching infinity and $\bar{N}$ very

much less than unity the following results are obtained using the expressions for the signal variances given in Appendix(1).

$$\lim_{\bar{N}\to\infty} SNR_{KT} = \frac{\sqrt{\bar{N}}}{2} \tag{33}$$

and

$$\lim_{\bar{N}\to\infty} SNR_{TC} = \frac{\sqrt{\bar{N}}}{3} . \tag{34}$$

$$SNR_{KT} = \frac{\bar{N}}{\sqrt{2}} \qquad \bar{N} \ll 1 \tag{35}$$

and

$$SNR_{TC} = \frac{\sqrt{\bar{N}^3}}{\sqrt{6}} \qquad \bar{N} \ll 1 . \tag{36}$$

The plots of Θ_E and SNR_m shown in Figs.3 and 4 indicate a close relationship between these quantities as expected from Eqs.(28) and (29). Typically,

$$\Theta_E \approx \frac{1}{\sqrt{2}SNR_m}; \tag{37}$$

however, the only generalisation that can be made provides an upper bound for the phase error in relation to SNR_m.

$$\Theta_E \leq \frac{1}{SNR_m}\sqrt{\frac{1+\sqrt{2}}{2}} \tag{38}$$

This inequality assumes nothing about the statistics of the fluctuating signal. Nevertheless it is a useful expression as it allows a bound on the phase error to be defined without calculating Θ_E which, in general, is a far more difficult task than evaluation of SNR_m. The additional $\sqrt{2}$ arises in this expression due to potential correlation between the real and imaginary parts of the complex signal, resulting in a non-zero covariance.

Nisenson and Papaliolios, [22], assume that in the KT method, for small Δu values, σ_m is the modulus of a complex error vector which can possess any phase between $\pm\pi$ with equal probability. This then gives, on averaging over all possible phases, in the expression for the phase error given by Eq.(37). If the simple imaging case previously described is again considered then the validity of these assumptions can be investigated. Figure 5 shows plots of the ratio of Θ_E, defined by Eq.(30), to

$1/(\sqrt{2}SNR_m)$ for the same KT and bispectrum planes as used in Fig.3. Both plots show the same important features and so only one of them, the KT plane in this case, needs to be studied in detail. It should be noted that the result is unity in general with, in particular, the exception of the region around $\Delta u_x=0$. This is important as this is the main region used for the reconstruction of the object's Fourier transform. These results are straightforward to explain if the Fourier transform of a single realisation is represented by $D_p(u)$, defined by Eq.(19). This is a summation over a number of unit moduli complex exponentials resulting in a complex exponential at each spatial frequency, u, which possesses a phase that is effectively uniformly distributed modulo 2π, correlated over a short range of spatial frequencies and uncorrelated between realisations, the correlation over spatial frequencies increasing if frames contain very few photon events. On this basis it is easily seen that away from the axes, where the KT signal is a product of Fourier transform values for well separated spatial frequencies (large Δu), then the real and imaginary parts of the signal are essentially uncorrelated random variables with equal variances. This gives rise to the same result as that of Nisenson and Papaliolios. However, the regions close to the axis, (small Δu) correspond to where the Nisenson and Papaliolios assumptions are made whereas it is exactly these regions for which the assumptions break down. The phase of the signal in each frame near the axis tends to be small, see Eq.(11), giving rise to a large real and small imaginary part. The real and imaginary parts therefore tend to be correlated and a non-zero covariance results. Additionally the real variance is large and the imaginary variance small. In general, the phase, ϕ, of the averaged signal is also small and so the following expression for the phase error results.

$$\Theta_E = \frac{\sigma_I}{|\langle S \rangle|} \frac{1}{\sqrt{M}} \tag{39}$$

As can be seen in Fig.5(b), this is smaller than that predicted by $1/(\sqrt{2}SNR_m)$ which contains the large real variance contribution. Unfortunately, the nature of sampling leads to occasssional discontinuities in the Fourier phase of the object being imaged. This can consequently give a large signal phase, ϕ, which increases the contributions of the real variance and the covariance to the phase error, see Eq.(30). The result is that Eq.(38) tends to the equality. This also can be seen in Fig.5(b) where large values for the plotted ratio are visible near the axis. The implication of this is that a larger number of frames are required in these high phase error regions than that predicted by the SNR_m value. The number of frames required could in fact be more than double the

SNR_m-based prediction. The latter does however appear to give a reasonable indication of the expected error on the phase of the mean signal, again indicating the usefulness of evaluating the SNR_m as opposed to the more complicated Θ_E.

5. Imaging a randomly translating object

The KT imaging technique is, unlike the TC, dependent on image shifts resulting in signal degradation. Consider trying to image, using the KT technique, an object whose image is randomly translating. Such translations may, for example, be a consequence of the first order degrading effect of atmospheric turbulence. The cause of image shift is wavefront tilt relative to the optical axis of the imaging system, which, as in the case of atmospheric turbulence, is effectively independent of other wavefront perturbations. Suppose such tilts result in a Gaussian probability distribution, $p(\mathbf{a})$, of image shifts, $\mathbf{a}$.

$$p(\mathbf{a}) = \frac{1}{\sqrt{2\pi}\sigma_a} \exp(-\frac{a^2}{2\sigma^2}) \tag{40}$$

where σ_a is the standard deviation of the shifts. An ensemble averaged transfer function may therefore be defined which reduces the KT signal by an amount dependent on Δu and σ_a .

$$\begin{aligned} \langle T_s(u) \rangle &= \int \exp(2\pi j u\mathbf{a}) \exp(2\pi j(u+\Delta u)\mathbf{a})\, p(\mathbf{a})\, d\mathbf{a} \\ &= \exp(-2\pi^2 \Delta u^2 \sigma^2) \end{aligned} \tag{41}$$

As an example consider a frequency sampling interval Δu of 0.5 arcseconds^{-1} and a standard deviation of image shift of 0.5 arcseconds. Such numbers are reasonably typical in the astronomical case and result in the signal being reduced by approximately 0.75. This effectively reduces the improved SNR obtained by averaging the KT double product as opposed to the equivalent bispectrum plane.

In the absence of photon noise centroiding images before correlating makes the KT method a shift invariant process and so removes the above effect. Assuming sampled data and Δu equal to the spatial frequency sampling interval. The Fourier spectrum of the centroided image, $\hat{I}(u)$, can be expressed using Fourier shift theorem as

$$\hat{I}(u) = I(u)\left\{\frac{I^*(\Delta u)}{|I(\Delta u)|}\right\}^{\frac{u}{\Delta u}} \tag{42}$$

and the KT average performed with centroided frames becomes

$$\hat{I}(u)\,\hat{I}^*(u+\Delta u) = I(u)\left\{\frac{I^*(\Delta u)}{|I(\Delta u)|}\right\}^{\frac{u}{\Delta u}} I^*(u+\Delta u)\left\{\frac{I(\Delta u)}{|I(\Delta u)|}\right\}^{\frac{u+\Delta u}{\Delta u}}$$

$$= I(u)\, I^*(u+\Delta u)\, \frac{I(\Delta u)}{|I(\Delta u)|} \tag{43}$$

The advantage of performing a double product for the KT has been lost and the correlation has now become a triple product in Fourier space, equivalent with respect to third order noise terms to the bispectrum.

At low light levels the problem is complicated by the presence of photon noise which prevents the accurate determination of the image centroid. The KT average obtained on averaging a series of low light level randomly moving images, centroiding each image before processing, can be shown to give, see Appendix (2),

$$< N_p\,(N_p-1)\, \hat{f}(u+\frac{\Delta u}{N_p})\, \hat{f}^*(u+\Delta u-\frac{\Delta u}{N_p})\, \hat{f}^*(\frac{\Delta u}{N_p})^{N_p-2} > \tag{44}$$

where N_p is the number of photon events in the pth image and $\hat{f}(u)$ is the Fourier transform of the object normalised by $I(0)$. The ensemble average over the Poisson statistics of the number of photon events in each image is left unresolved due to the intrinsic object dependency of the above result. This result differs from the desired result,

$$< N_p\,(N_p-1)\, \hat{f}(u)\, \hat{f}^*(u+\Delta u) >, \tag{45}$$

because of the presence of the frequency shift vector, $\frac{\Delta u}{N_p}$. The latter is, however, negligibly small for all images except those containing a few photons. In particular, for frames containing two photons the autocorrelation results and no phase information is preserved. The centroiding error effect obviously increases with Δu. This result is important as it suggests that the technique cannot be used in its present form when only a few photon events per frame are recorded. This is in contrast to the shift invariant TC which allows objects to be imaged reasonably well at very low photon levels [29],[30].

6. Imaging through atmospheric turbulence

Both the KT and the TC techniques have been used successfully for imaging astronomical objects. Their success is based upon the techniques overcoming the degrading properties of atmospheric turbulence. Many images are recorded, with exposure times short enough to freeze atmospheric perturbations, and processed to yield ensemble average transfer functions which contain diffraction limited information. Obtainable resolutions are therefore ultimately limited by telescope characteristics.

The complex mathematical nature of the transfer functions concerned makes a complete analytical study extremely difficult. We have therefore used Monte Carlo computer simulations to obtain a reasonable idea of the effects of the statistical fluctuations of atmospheric turbulence. The wavefront phase perturbations induced by the turbulence have been considered to have a Gaussian correlation function with a standard deviation of value r_o/λ, r_o being the Fried [2] parameter describing the atmospheric conditions being studied. Wavefront amplitude perturbations are not present in the simulations. The simulations allow any form of telescope pupil function to be used and the imaging of arbitrary object intensity distributions. The introduction of photon noise is also possible.

Initially, consider a further simplification of the problem based on the work of Roddier [16]. Suppose the atmosphere is modelled by a distribution of 'seeing' cells of diameter r_o/λ in angular spatial frequency space. The wavefront phase is assumed constant across each seeing cell and the complex amplitude is assumed uncorrelated between cells. Using this basic model the processing techniques may be simply explained.

Consider two 'seeing' cells separated by a vector in the telescope pupil, λu, where λ is the mean wavelength and u an angular spatial frequency vector. If a point source is imaged through the telescope using a pupil function consisting of two apertures, corresponding to the two 'seeing' cells, then a fringe pattern is produced with a narrow spatial frequency bandwidth. The major component, at frequency u, $I(u)$, is produced by contributions from all pairs of points with a separation λu, one point in each aperture, see Fig.6(a). If the major component is averaged over many frames then the result for frequencies greater then r_o/λ tends to zero. This is due to the phase difference, $\Phi_A - \Phi_B$, modulo 2π between the two apertures being uniformly distributed

between $\pm\pi$ with zero mean, see Fig.7(a). This results in the Fourier component performing a random walk in the complex plane and averaging to zero.

$$arg\left\{I(u)\right\} = \phi(u) + \Phi_A - \Phi_B \tag{46}$$

$$\langle I(u)\rangle = 0 \; ; \quad u > r_o/\lambda \tag{47}$$

where $\phi(u)$ is the Fourier phase at frequency u, and $\langle\ \rangle$ indicates an ensemble average over many frames.

Consider now the autocorrelation technique which in Fourier space corresponds to estimating the power spectrum. The major Fourier component of the fringe pattern is averaged as a product with its complex conjugate and so the atmospheric phase contribution is eliminated and the averaged signal is non-zero, see Fig.6(b).

$$arg\left\{I(u)\, I(-u)\right\} = \phi(u) + \Phi_A - \Phi_B + \phi(-u) - \Phi_A + \Phi_B = 0 \tag{48}$$

and

$$\langle I(u)\, I(-u)\rangle = \langle |I(u)|^2 \rangle \neq 0. \tag{49}$$

Unfortunately phase information is not preserved. This is the simplest form of the 'phase closure' [11] idea used in radio astronomy.

The KT technique is a small modification of the above. The major Fourier component of the fringe pattern is averaged with a component at a frequency displaced by a small vector Δu. Provided the vector displacement Δu does not force the vector difference $-u-\Delta u$ to be outside the spatial frequency bandwidth of the fringe pattern then Fourier phase difference information is preserved in the averaged signal, see Fig.7(b). Again the atmospheric phase effectively forms a closed loop, see Fig.6(c).

$$arg\left\{I(u)\, I(-u-\Delta u)\right\} = \phi(u) + \Phi_A - \Phi_B + \phi(-u-\Delta u) - \Phi_A + \Phi_B \tag{50}$$

$$= \phi(u) - \phi(u+\Delta u)$$

and

$$\langle I(u)\, I(-u-\Delta u)\rangle \neq 0 \; ; \quad \Delta u < r_o/\lambda. \tag{51}$$

Suppose this system of two apertures is extended to three and the Δu value is made greater than r_o/λ , see Fig.6(d).
Now

$$arg\left\{I(u)\, I(-u-\Delta u)\right\} = \phi(u) + \Phi_A - \Phi_B - \phi(-u-\Delta u) - \Phi_A + \Phi_C$$

$$= \phi(u) - \phi(u+\Delta u) - \Phi_B + \Phi_C \qquad (52)$$

$$< I(u)\, I(-u-\Delta u) > = 0 ; \quad \Delta u < r_o/\lambda. \qquad (53)$$

It can be seen that the atmospheric phase contribution is not closed. The resulting phase becomes uniformly distributed, see Fig.7(c), and the signal performs a random walk and averages to zero. Thus the KT technique is limited to frequency differences $\Delta u < r_o/\lambda$. If however the bispectrum average is performed then the phase is again closed and Fourier phase difference information is preserved, see Fig.7(d) and Fig.7(e).

$$arg\left\{I(u)\, I(\Delta u)\, I(-u-\Delta u)\right\} = \phi(u) + \Phi_A - \Phi_B + \phi(\Delta u) \qquad (54)$$

$$+ \Phi_B - \Phi_C + \phi(-u-\Delta u) - \Phi_A + \Phi_C$$

$$= \phi(u) - \phi(u+\Delta u) + \phi(\Delta u)$$

Thus the bispectrum, unlike the KT, can obtain phase difference information for phase differences, Δu, greater than r_o/λ. It is apparent that the phase closure requirement can be restated in terms of the spatial frequency vectors which define a particular technique in Fourier space; the vector sum of the spatial frequency vectors must be less than r_o/λ for the ensemble average of the signal to be non-zero, the only exception being if frequency vectors can be grouped together such that all the groups independently have a sum that is less than r_o/λ.

Using this simplified model it can be seen how the techniques are related through the phase closure concept and how they allow preservation of Fourier phase information. However, the use of a telescope pupil consisting of a few sub-apertures only allows a limited number of spatial frequencies to be studied. This may be desirable in certain circumstances but in general the full telescope aperture is used to make use of all the available light flux and to allow many spatial frequencies to be studied.

Suppose a series of short exposure images are recorded. The pth image may be represented, using the incoherent imaging equation in Fourier space, as

$$I_p(u) = O(u)\, S_p(u) \tag{55}$$

where $S_p(u)$ is the combined transfer function of the telescope-atmosphere imaging system. The ensemble averaged transfer functions of the KT and TC techniques are defined by

$$T^{(KT)}(u_1,\Delta u) = \langle S_p(u_1)\, S_p^*(u_1+\Delta u) \rangle \tag{56}$$

and

$$T^{(TC)}(u_1,u_2) = \langle S_p(u_1)\, S_p^*(u_1+u_1)\, S_p(u_2) \rangle \tag{57}$$

respectively.

The effect of using the full aperture on these transfer functions is, firstly, to introduce information on all spatial frequencies out to the telescope diffraction limit and, secondly, to lower the transfer function for those frequencies which were present with the three sub-aperture pupil function. The reduction of the average transfer functions is due to contributions from combinations of sub-apertures, present in the full pupil, for which phase closure is not realised. For example, signal contributions from the two frequency vectors, u and u+Δu in Fig.6(c), but with both of the vectors lying between different pairs of sub-apertures thus preventing phase closure.

Although both transfer functions are four dimensional a reasonable indication of their behaviour may be obtained by studying two dimensional sub-planes through them corresponding to $u_1=u_{1x}$, with $\Delta u=\Delta u_x$ for the KT and $u_2=u_{2x}$ for the bispectrum. Fig.8 shows plots of these planes, obtained using the Monte Carlo computer simulation, allowing a comparison of their basic properties. Both possess a high central region for frequencies u_{1x}, Δu_x and u_{2x} being less than the 'seeing cutoff' of approximately r_o/λ. Additionally both planes contain a high region around the axis $u_{1x}=0$. This region allows information about frequency differences of up to approximately r_o/λ to be recovered with high signal-to-noise-ratio. It should be noted that this region is wider in the KT case. This is due to the third term present in the bispectrum triple product which reduces the bispectrum modulus, falling off in a similar manner to the short-exposure transfer function. Cross-sections through these planes, see Fig.9, show this fact. However, the benefit of this additional term can also be seen. As the frequency difference vectors, Δu_x and u_{2x}, increase, the KT signal, in contrast to the

bispectrum, reduces in value and becomes more random due to the lack of exact phase closure. The remaining high regions present in the bispectrum are redundant due to the twelve fold symmetry of the function.

Of particular interest, is the number of different frequency difference vectors, Δu_x and u_{2x}, high signal to noise information can be acquired. In general the greater the number the better the resulting reconstructed object intensity distribution[14],[23].

Signal to noise ratio (SNR)

Again the problem arises of describing the statistics of complex signals. The use of the phase error measure, Θ_E (Eq.(30)), poses many problems in an analytic study due to the complexity of the signal variances required. Consequently, the SNR measure SNR_m (Eq.(28)) is used, as in section 4, to compare analytically the KT and TC techniques. The phase error measure, Θ_E, has however been studied computationally, using the Monte Carlo simulation previously described and the following results comparing Θ_E and the SNR_m when imaging through atmospheric turbulence were obtained.

Figure (10) shows plots of the ratio of the phase error Θ_E to $1/(\sqrt{2}SNR_m)$ for the sub planes of the KT signal and the bispectrum defined by $u_1=u_{1x}$, $u_2=u_{2x}$, $\Delta u=\Delta u_x$. These plots are the result of computationally simulating the effect of imaging the 'asteroid' shown in Fig.3(c) with a 2 metre telescope and 0.7 arc second 'seeing'. Five thousand independent realisations of the atmosphere were used to obtain the ensemble averages. These plots should be directly compared with those in Fig.5. Although no photon noise is present the atmospheric turbulence induced signal fluctuations result in the same overall effect; the variances of the real and imaginary part of the signal tend to be independent and equal, with zero covariance, away from the axes, whereas near the axes the covariance tends to be larger with a small imaginary variance and a large real variance. Again the SNR_m appears to give a reasonable indication of the phase error, however the fluctuation of the ratio about unity near the axes is still present, a consequence of the non-zero covariance.

The signal to noise ratios of the KT and TC in Fourier space are defined by

$$SNR^{(KT)}(u_1,\Delta u) = \frac{|\langle I_p(u_1)\, I_p^*(u_1+\Delta u)\rangle|}{\sigma_{(KT)}}\sqrt{M} \tag{58}$$

where

$$\sigma^2_{(KT)} = \langle |I_p(u_1)\, I_p^*(u_1+\Delta u)|^2\rangle - |\langle I_p(u_1)\, I_p^*(u_1+\Delta u)\rangle|^2,$$

and

$$SNR^{(TC)}(u_1,u_2) = \frac{|\langle I_p(u_1)\, I_p^*(u_1+u_2)\, I_p(u_2)\rangle|}{\sigma_{(TC)}}\sqrt{M} \tag{59}$$

where

$$\sigma^2_{(TC)} = < | I_p(u_1)\, I_p^*(u_1+u_2)\, I_p(u_2) |^2 > - | < I_p(u_1)\, I_p^*(u_1+u_2)\, I_p(u_2) > |^2,$$

and M is the number of independent images.

In order to compare the SNR's the averages must be evaluated for a range of frequency vectors. Based on the model of Roddier, [16], the following results have been obtained. The mean number of speckles per frame, $\bar{n}_p$, is assumed to be much greater than unity and $\bar{n}_s$ is 2.3 $(D/r_o)^2$, D being the telescope diameter.

The approximations required to estimate the effect of atmospheric turbulence on ensemble averages are repetitive, and tedious. Consequently, a typical quantity, the ensemble average mean square of the bispectrum, is treated in detail as a worked example, see in Appendix (3). The effect on imaging a point source at high light level is considered first. The Fourier spectrum of the pth image, $I_p(u_1)$, therefore reduces to that of the point spread function of the telescope-atmosphere combination, $S_p(u)$.
For u_1, u_2, $\Delta u > r_o/\lambda$,

$$< S_p(u_1)\, S_p^*(u_1+u_2)\, S_p(u_2) > \approx \frac{2}{\bar{n}_s^2}\, T^{(3)}(u_1,u_2) \tag{60}$$

$$< |S_p(u_1)\, S_p^*(u_1+u_2)\, S_p(u_2)|^2 > \approx \frac{1}{\bar{n}_s^3}\, T^{(2)}(u_1)\, T^{(2)}(u_2)\, T^{(2)}(u_1+u_2) \tag{61}$$

$$< S_p(u_1)\, S_p^*(u_1+\Delta u) > \approx 0 \tag{62}$$

and for u_2, $\Delta u < r_o/\lambda$,

$$< S_p(u_1)\, S_p^*(u_1+u_2)\, S_p(u_2) > \approx \frac{1}{\bar{n}_s}\, T^{(2)}(u_1) < S_p(u_2) > \tag{63}$$

$$< S_p(u_1)\, S_p^*(u_1+\Delta u) > \approx \frac{1}{\bar{n}_s}\, T^{(2)}(u_1) \tag{63}$$

$$< |S_p(u_1)\, S_p^*(u_1+u_2)\, S_p(u_2)|^2 > \approx \frac{2}{\bar{n}_s^2}\, |T^{(2)}(u_1)|^2\, | < S_p(u_2) > |^2 \tag{64}$$

$$< |S_p(u_1)\, S_p^*(u_1+\Delta u)|^2 > \approx \frac{2}{\bar{n}_s^2}\, |T^{(2)}(u_1)|^2 \tag{65}$$

where $T^{(2)}(u)$ is the normalised overlap integral of two pupils separated by u, and $T^{(3)}(u_1,u_2)$ is the normalised overlap integral of three pupils separated by u_1 and u_2. Consequently, the SNR's are

$$SNR^{(TC)} = \frac{2\,T^{(3)}(u_1,u_2)}{\bar{n}_s^{1/2}\,[T^{(2)}(u_1)\,T^{(2)}(u_1+u_2)\,T^{(2)}(u_2)\,]^{1/2}}\sqrt{M} \qquad u_1,\ u_2 > r_o/\lambda$$

$$\approx \sqrt{M} \qquad u_2 < r_o/\lambda \tag{66}$$

and

$$SNR^{(KT)} \approx 0 \qquad u_1,\ \Delta u > r_o/\lambda$$

$$\approx \sqrt{M} \qquad \Delta u < r_o/\lambda. \tag{67}$$

For u_1, $\Delta u < r_o/\lambda$ at high light level both techniques have statistics which, within the approximations made here, reflect the negative exponential behaviour of the SNR of the power spectrum[18]. For frequencies outside this range, for which no power spectrum equivalent exists, the KT has approximately zero SNR whereas the bispectrum SNR has a $1/\sqrt{\bar{n}_s}$ dependency. This result disagrees with that obtained by Wirnitzer [23] which shows no such dependency. The SNR of the information for $u_2 > r_o/\lambda$ is therefore typically of the order of $\sqrt{\bar{n}_s}$ lower than that for $u_2 < r_o/\lambda$. If individual images are considered to be independent then in order to obtain equivalent SNR in both regions a multiplicative factor of order $\bar{n}_s$ more frames are required when $u_2 > r_o/\lambda$.

Figure 11 shows plots of a single plane of the KT and bispectrum ($u_1=u_{1x}$, $u_2=u_{2x}$, $\Delta u=\Delta u_x$) SNR's at high light level obtained using the computer simulation. Again the high region around $u_{1x}=0$ should be compared between the two plots. The width of this region gives an indication of the number of frequency difference vectors high SNR information is available for object reconstruction. On comparing cross-sections for constant Δu_x and u_{2x} values it is found that both techniques have very similar SNR's if difference vectors are less than approximately r_o/λ, see Fig.12. Beyond this value the closure phase property of the bispectrum maintains its SNR above that of the KT which tends to fluctuate wildly. The high SNR regions around the axes are constricted near the origin for both techniques. This is particularly

noticable in the bispectrum where distinct regions of low SNR exist, corresponding to positions where two of the terms in the bispectrum triple product are identical, hence increasing the variance of the bispectrum phase. These regions are clearly visible in Fig.11, for example around the line defined by $u_{1x} = u_{2x}$. In contrast to the transfer functions, the SNR's for the cross-sections shown, with Δu_x, $u_{2x} < r_o/\lambda$, maintain a roughly constant value for values of u_{1x} up to approximately r_o/λ of the telescope imposed cutoff.

Unfortunately, the need to observe astronomical objects with low luminosity and the short exposure requirement of 'freezing' the atmosphere result in low numbers of photon events being recorded in individual images. For such low light level images the effect of photon noise becomes important. The photon noise dependent variances, see Appendix (1), therefore need to be averaged over the atmospheric statistics in various regimes. These regimes being defined in general by the ratio, $\bar{n}$, of the average number of photons, $\bar{N}$, to the average number of speckles per frame, $\bar{n}_s$, and by the value of the frequency vectors u_1, u_2, Δu. Again using the model of Roddier[16], averaging over the atmospheric statistics yields the following approximations for the required statistical moments.

For u_1, u_2, $\Delta u > r_o/\lambda$,

$$\sigma^2_{(TC)} = \bar{N}^3 + \frac{T^{(2)}(u_2)}{\bar{n}_s}\bar{N}^2 + \frac{T^{(2)}(u_1)}{\bar{n}_s}\bar{N}^2 + \frac{T^{(2)}(u_1+u_2)}{\bar{n}_s}\bar{N}^2 + \frac{T^{(2)}(u_1)}{\bar{n}_s^2}T^{(2)}(u_2)\bar{N}^3 + \frac{T^{(2)}(u_1)}{\bar{n}_s^2}T^{(2)}(u_1+u_2)\bar{N}^3 + \frac{T^{(2)}(u_1+u_2)}{\bar{n}_s^2}T^{(2)}(u_2)\bar{N}^3 + \frac{T^{(2)}(u_1)}{\bar{n}_s^3}T^{(2)}(u_1+u_2)T^{(2)}(u_2)\bar{N}^3 \qquad \bar{N} > 1, \tag{68}$$

$$\sigma^2_{(TC)} = \bar{N}^3 \qquad \bar{N} > 1,\ \bar{n} \ll 1 \tag{69}$$

$$\sigma^2_{(KT)} = 0. \tag{70}$$

For u_2, $\Delta u < r_o/\lambda$,

$$\sigma^2_{(TC)} = \bar{N}^3 + \bar{N}^4 |< S_p(u_2) >|^2 + \frac{\bar{N}^4}{\bar{n}_s} T^{(2)}(u_1) + \frac{\bar{N}^4}{\bar{n}_s} T^{(2)}(u_1+u_2)$$

$$+ \frac{\bar{N}^5}{\bar{n}_s} T^{(2)}(u_1) |< S_p(u_2) >|^2 + \frac{\bar{N}^5}{\bar{n}_s} T^{(2)}(u_1+u_2) |< S_p(u_2) >|^2$$

$$+ \frac{\bar{N}^6}{\bar{n}_s^2} T^{(2)}(u_1) T^{(2)}(u_1+u_2) |< S_p(u_2) >|^2 \qquad \bar{N} > 1 \tag{71}$$

$$\sigma^2_{(TC)} \approx \bar{N}^3 + \bar{N}^4 |< S_p(u_2) >|^2 \qquad \bar{N} > 1, \bar{n} \ll 1 \tag{72}$$

$$\sigma^2_{(KT)} \approx \bar{N}^2 + \frac{\bar{N}^3}{\bar{n}_s} T^{(2)}(u_1) + \frac{\bar{N}^3}{\bar{n}_s} T^{(2)}(u_1+\Delta u)$$

$$+ \frac{\bar{N}^4}{\bar{n}_s^2} T^{(2)}(u_1) T^{(2)}(u_1+\Delta u) \qquad \bar{N} > 1 \tag{73}$$

$$\sigma^2_{(KT)} \approx \bar{N}^2 \qquad \bar{N} > 1, \bar{n} \ll 1 \tag{74}$$

The mean signals are

$$\bar{N}^3 T^{(TC)}(u_1,u_2) \quad \text{and} \quad \bar{N}^2 T^{(KT)}(u_1,\Delta u)$$

for the bispectrum and KT respectively.

The SNR's of the two techniques may now be compared for the various regimes. For u_1, u_2, $\Delta u > r_o/\lambda$,

$$SNR^{(TC)} \approx \bar{N}^{3/2} T^{(TC)}(u_1,u_2) \sqrt{M}$$

$$\approx \frac{2}{\bar{n}_s^2} \sqrt{\bar{N}^3} T^{(3)}(u_1,u_2)\sqrt{M} \qquad \bar{n} \ll 1 \tag{75}$$

The result is more complicated for larger $\bar{n}$ but the general form corresponds to a gradual falling off of the dependence on $\bar{N}$ due to the variance becoming more dependent on $\bar{N}$ as succesive terms in Eq.(68) take precedence. Eventually, for $\bar{n} \gg 1$, the SNR is simple dependent on $\bar{n}_s$ as the $\bar{N}^6$ dependent term of Eq.(68) dominates the variance. When $\bar{N}$ is approximately equal to $\bar{n}_s$ then there is roughly a linear dependence of the $SNR^{(TC)}$ on $\bar{N}$ as the $\bar{N}^4$ dependent term dominates the variance. The KT has approximately zero SNR in the equivalent region, $\Delta u > r_o/\lambda$.

For u_2, $\Delta u < r_o/\lambda$ and $\bar{n} \ll 1$,

$$SNR^{(TC)} \simeq \frac{\bar{N}^3 \, T^{(KT)}(u_1,u_2) < S_p(u_2) >}{\bar{n}_s \, [\, \bar{N}^3 + \bar{N}^4 \, |< S_p(u_2) >|^2 \,]^{1/2}} \sqrt{M} \tag{76}$$

and

$$SNR^{(KT)} \simeq \frac{\bar{N}}{\bar{n}_s} \, T^{(KT)}(u_1,\Delta u) \, \sqrt{M}. \tag{77}$$

In particular Eq.(76) reduces to a linear dependence on $\bar{n}$, equivalent to the power spectrum, for $u_2 = 0$, as expected. Again for larger $\bar{n}$ both SNR's are far more complicated but, as before, their dependence on $\bar{N}$ gradually falls off as the terms in the variances dependent on higher powers of $\bar{N}$ dominate. Both SNR's tend to the high light level value of unity, as for the power spectrum, for $u_2 = \Delta u = 0$.

A Monte Carlo simulation has been carried out, see Fig.13, which reasonably confirms the $\bar{N}$ and $\bar{n}_s$ dependencies of the above SNR results.

The ensemble averaged variances derived can easily be incorporated into phase reconstruction algorithms [28] to weight optimally the information present in the average signals. The expression for the variance of the bispectrum given in Eq.(68) is particularly useful as a weighting function as it can be evaluated from knowledge of $\bar{N}$ and the ensemble average image spatial power spectrum at various spatial frequencies. This weighting function will, however, suffer from the fact that it is independent of the phase of the bispectrum at each point. Two possible approaches to overcoming this are the following. Firstly, a larger weighting function can be given to those points for which the bispectrum phase is not close to zero on the basis of the phase error tending to the equality in Eq. 38). Alternatively, the variances and covariance of the real and

imaginary parts of the complex signal, see Appendix (1), could be approximated in a similar manner to the variance of the modulus and the full expression for the phase error defined in Eq.(30) evaluated.

CONCLUSION

It is evident that the KT and TC methods of image processing are very closely related from both the mathematical and implementation viewpoints. The extension of the KT method to a more general form, whereby the frequency difference vector, Δu, can take on a wide range of values removes the TC advantage of a having a redundency of phase information that can increase the SNR. It is necessary to centroid images before processing using the KT method and this removes the signal-to-noise-ratio, SNR, gain over the TC which should result as a consequence of being a lower order correlation. Additionally, the need to centroid and the development of an efficient photon differencing TC algorithm result in implementation times being equivalent, despite the KT method being a lower order correlation.

A more appropriate measure of the phase error, Θ_E, of a complex signal has been suggested. This has been compared with the traditional SNR based measure whereby the phase error is approximated by $1/(\sqrt{2}SNR)$. It is found that this gives a reasonable indication of the phase error; however, in certain circumstances, for small frequency difference vectors, the value predicted by this means can be considerably in error. It is seen that the SNR can be used to provide an upper bound on the phase error.

$$\Theta_E \leq \frac{\sqrt{1+\sqrt{2}}}{\sqrt{2}SNR}.$$

Speckle interferometry, the KT correlation and the TC have been seen to be connected through phase closure relationships. By considering phase closure in terms of spatial frequency vectors forming closed loops in the telescope pupil, it has been possible to evaluate many ensemble averages of image correlations over the statistics of atmospheric turbulence. A computer implementation of a generalisation of the technique of Goodman and Belsher[18] has allowed photon noise dependent SNR's to be investigated. Using these developments, together with a computer simulation of the effects of imaging through turbulence, the SNR's of the TC and KT methods have been compared with, in particular, their dependency on $\bar{n}_s$ and $\bar{N}$.

It is found that the the highest SNR regions of both the TC and KT average signals are of equivalent value and extent. They correspond to using frequency difference vectors, Δu, u_2, that have magnitudes that are less than, or of the order of, r_o/λ. In this

region both SNR's are linearly dependent on the number of photons per speckle at very low light levels and approximately unity at high light level. They are reflecting their close assosciation with the negative exponential statistics of the power spectrum. Outside these high SNR regions the KT signal is insignificant and the bispectrum SNR shows a $\sqrt{\bar{N}^3}/\bar{n}_s^2$ dependency at very low light levels and a $1/\sqrt{\bar{n}_s}$ at high level. Again this is suggesting the effective equivalance of the two techniques as for typical values of $\bar{n}_s$, of the order of 1000, the additional information present in the bispectrum would require many more frames to be processed to be of any use. Results from a Monte-Carlo type computer simulation, which enabled the ensemble average over the atmospheric statistics to be evaluated within the constraints of the model used, agree well with the results obtained from the analytic study based on phase closure relations.

This work was supported by the UK Science and Engineering Research Council (GR/D 92332) and the US Army (DAJA 45-85-C-0028).

Appendices

Appendix (1)

A computer implementation of a generalisation of Goodman and Belsher's method [18] for averaging signals in Fourier space in the presence of photon noise has been used to yield the following results. Consider imaging, with a mean number of photon events per frame of $\bar{N}$, an intensity distribution which has a high light level image with the Fourier transform $I(u)$.

The KT signal of the pth frame is, in Fourier space,

$$D^{(KT)}(u_1,\Delta u) = D_p(u_1)\, D_p^*(u_1+\Delta u) - D_p^*(\Delta u), \qquad \text{(A1.1)}$$

resulting in the following expressions for the second order statistics. The second moment of the real part of the signal is given by

$$1/4 < [\, D_p^{(KT)}(u_1,\Delta u) + D_p^{(KT)^*}(u_1,\Delta u)\,]^2 > \qquad \text{(A1.2)}$$

and averaging over the photon noise statistics gives

$$\begin{aligned}
&1/4\, [\, I(-u_1)\, I(-u_1)\, I(u_1+\Delta u)\, I(u_1+\Delta u)\, \bar{N}^4 + cc \\
&+ 2\, I(-u_1-\Delta u)\, I(-u_1)\, I(u_1)\, I(u_1+\Delta u)\, \bar{N}^4 \\
&+ I(-u_1)\, I(-u_1)\, I(2u_1+2\Delta u)\, \bar{N}^3 + cc \\
&+ 2\, I(-u_1)\, I(u_1)\, \bar{N}^3 \\
&+ 2\, I(-u_1)\, I(\Delta u)\, I(u_1+\Delta u)\, \bar{N}^3 + cc \\
&+ 2\, I(-u_1-\Delta u)\, I(-u_1)\, I(2u_1+\Delta u)\, \bar{N}^3 + cc \\
&+ I(-u_1-\Delta u)\, I(-u_1-\Delta u)\, I(2u_1)\, \bar{N}^3 + cc \\
&+ 2\, I(-u_1-\Delta u)\, I(u_1+\Delta u)\, \bar{N}^3 \\
&+ I(-\Delta u)\, I(-\Delta u)\, \bar{N}^2 + cc \\
&+ I(-2u_1)\, I(2u_1+2\Delta u)\, \bar{N}^2 + cc \\
&+ 2\, I(-2u_1,-\Delta u)\, I(2u_1+\Delta u)\, \bar{N}^2 \\
&+ 2\, \bar{N}^2\,],
\end{aligned}$$

where cc indicates the complex conjugate. It should be noted that each cc is the complex conjugate of the whole of the term to its left, including the sign.

The second moment of the imaginary part of the signal is given by

$$-1/4 < [\, D_p^{(KT)}(u_1,\Delta u) - D_p^{(KT)^*}(u_1,\Delta u)\,]^2 >, \qquad \text{(A1.3)}$$

and averaging over the photon noise statistics gives

$$\begin{aligned}
&-1/4\ [\, I(-u_1)\, I(-u_1)\, I(u_1+\Delta u)\, I(u_1+\Delta u)\, \bar{N}^4 + cc \\
&-2\, I(-u_1-\Delta u)\, I(-u_1)\, I(u_1)\, I(u_1+\Delta u)\, \bar{N}^4 \\
&+ I(-u_1)\, I(-u_1)\, I(2u_1+2\Delta u)\, \bar{N}^3 + cc \\
&-2\, I(-u_1)\, I(u_1)\, \bar{N}^3 \\
&+2\, I(-u_1)\, I(\Delta u)\, I(u_1+\Delta u)\, \bar{N}^3 + cc \\
&-2\, I(-u_1-\Delta u)\, I(-u_1)\, I(2u_1+\Delta u)\, \bar{N}^3 + cc \\
&+ I(-u_1-\Delta u)\, I(-u_1-\Delta u)\, I(2u_1)\, \bar{N}^2 + cc \\
&-2\, I(-u_1-\Delta u)\, I(u_1+\Delta u)\, \bar{N}^3 \\
&+ I(-\Delta u)\, I(-\Delta u)\, \bar{N}^2 + cc \\
&+ I(-2u_1)\, I(2u_1+2\Delta u)\, \bar{N}^2 + cc \\
&-2\, I(-2u_1-\Delta u)\, I(2u_1+\Delta u)\, \bar{N}^2 \\
&-2\, \bar{N}^2\,].
\end{aligned}$$

The first joint moment of the real and imaginary parts of the signal is given by

$$-1/4 < [\, D_p^{(KT)}(u_1,\Delta u) - D_p^{(KT)^*}(u_1,\Delta u)\,] \cdot [\, D_p^{(KT)}(u_1,\Delta u) + D_p^{(KT)^*}(u_1,\Delta u)\,] >. \qquad \text{(A1.4)}$$

and averaging over the photon noise statistics gives

$$\begin{aligned}
&-1/4\ [\, I(-u_1-\Delta u)\, I(-u_1-\Delta u)\, I(u_1)\, I(u_1)\, \bar{N}^4 - cc \\
&+ I(-u_1-\Delta u)\, I(-u_1-\Delta u)\, I(2u_1)\, \bar{N}^3 - cc \\
&+2\, I(-u_1-\Delta u)\, I(-\Delta u)\, I(u_1)\, \bar{N}^3 - cc \\
&+ I(-2u_1-2\Delta u)\, I(u_1)\, I(u_1)\, \bar{N}^3 - cc \\
&+ I(-\Delta u)\, I(-\Delta u)\, \bar{N}^2 - cc \\
&+ I(-2u_1-2\Delta u)\, I(2u_1)\, \bar{N}^2 - cc\,].
\end{aligned}$$

The TC signal of the pth frame is, in Fourier space,

$$D_p^{(TC)}(u_1,u_2) = D_p(u_1)\, D_p^*(u_1+u_2)\, D_p(u_2) - |D_p(u_1)|^2 - |D_p(u_1+u_2)|^2 - |D_p(u_2)|^2 + 2N_p, \qquad \text{(A1.5)}$$

resulting in the following expressions for the second order statistics.

The second moment of the real part of the signal is given by

$$1/4 < [\, D_p^{(TC)}(u_1,u_2) + D_p^{(TC)^*}(u_1,u_2)\,]^2 > \qquad \text{(A1.6)}$$

and averaging over the photon noise statistics gives

$$\begin{aligned}
&1/4\, [\, I(-u_1)\, I(-u_1)\, I(-u_2)\, I(-u_2)\, I(2u_1+2u_2)\, \bar{N}^3 + cc \\
&+ 2\, I(-u_1)\, I(-u_1)\, I(-u_2)\, I(u_1)\, I(u_1+u_2)\, \bar{N}^3 + cc \\
&+ I(-u_1)\, I(-u_1)\, I(-2u_2)\, I(u_1+u_2)\, I(u_1+u_2)\, \bar{N}^3 + cc \\
&+ 2\, I(-u_1)\, I(-u_2)\, I(-u_1)\, I(u_2)\, I(u_1+u_2)\, \bar{N}^3 + cc \\
&+ 2\, I(-u_1)\, I(-u_2)\, I(u_2)\, I(u_1)\, \bar{N}^3 \\
&+ 2\, I(-u_1-u_2)\, I(-u_1)\, I(-u_2)\, I(u_1)\, I(u_1+2u_2)\, \bar{N}^3 + cc \\
&+ 2\, I(-u_1-u_2)\, I(-u_1)\, I(-u_2)\, I(u_1+u_2)\, I(u_1+u_2)\, \bar{N}^3 + cc \\
&+ 2\, I(-u_1-u_2)\, I(-u_1)\, I(-u_2)\, I(u_2)\, I(2u_1+u_2)\, \bar{N}^3 + cc \\
&+ 2\, I(-u_1-u_2)\, I(-u_1)\, I(u_1)\, I(u_1+u_2)\, \bar{N}^3 \\
&+ 2\, I(-u_1-u_2)\, I(-u_1)\, I(u_2)\, I(u_1-u_2)\, I(u_1+u_2)\, \bar{N}^3 + cc \\
&+ I(-u_1-u_2)\, I(-u_1-u_2)\, I(u_2)\, I(u_2)\, I(2u_1)\, \bar{N}^3 + cc \\
&+ 2\, I(-u_1-u_2)\, I(-u_2)\, I(u_2)\, I(u_1+u_2)\, \bar{N}^3 \\
&+ I(-u_1)\, I(-u_1)\, I(-2u_2)\, I(2u_1+2u_2)\, \bar{N}^2 + cc \\
&+ 2\, I(-u_1)\, I(-u_1)\, I(u_1)\, I(u_1)\, \bar{N}^2 \\
&+ 4\, I(-u_1)\, I(-u_2)\, I(u_2)\, I(u_1)\, \bar{N}^2 \\
&+ 2\, I(-u_1)\, I(-2u_2)\, I(u_2)\, I(u_1+u_2)\, \bar{N}^2 + cc \\
&+ 2\, I(-u_1)\, I(u_1)\, \bar{N}^2 \\
&+ 2\, I(-u_1)\, I(u_2)\, I(u_1-u_2)\, \bar{N}^2 + cc \\
&+ 2\, I(-u_1-u_2)\, I(-u_1)\, I(-u_2)\, I(2u_1+2u_2)\, \bar{N}^2 + cc \\
&+ 4\, I(-u_1-u_2)\, I(-u_1)\, I(u_1)\, I(u_1+u_2)\, \bar{N}^2 \\
&+ 2\, I(-u_1-u_2)\, I(-u_1)\, I(u_1-u_2)\, I(u_1+2u_2)\, \bar{N}^2 + cc \\
&+ 2\, I(-u_1-u_2)\, I(-u_1)\, I(u_2)\, I(2u_1)\, \bar{N}^2 + cc \\
&+ 2\, I(-u_1-u_2)\, I(-u_1)\, I(2u_1+u_2)\, \bar{N}^2 + cc
\end{aligned}$$

$$
\begin{aligned}
&+ 2\, I(-u_1-u_3)\, I(-u_1+u_3)\, I(-u_3)\, I(2u_1+u_3)\, \bar{N}^4 + cc \\
&+ 2\, I(-u_1-u_2)\, I(-u_1+u_3)\, I(u_1-u_2)\, I(u_1+u_2)\, \bar{N}^4 \\
&+ 2\, I(-u_1-u_2)\, I(-u_1-u_2)\, I(u_1+u_2)\, I(u_1+u_2)\, \bar{N}^4 \\
&+ I(-u_1-u_2)\, I(-u_1-u_2)\, I(2u_2)\, I(2u_1)\, \bar{N}^4 + cc \\
&+ 2\, I(-u_1-u_2)\, I(-u_2)\, I(u_1+2u_2)\, \bar{N}^4 + cc \\
&+ 4\, I(-u_1-u_2)\, I(-u_2)\, I(u_2)\, I(u_1+u_2)\, \bar{N}^4 \\
&+ 2\, I(-u_1-u_2)\, I(u_1+u_2)\, \bar{N}^4 \\
&+ 2\, I(-u_1-2u_2)\, I(-u_1)\, I(u_1)\, I(u_1+2u_2)\, \bar{N}^4 \\
&+ 2\, I(-u_1-2u_2)\, I(-u_1)\, I(u_2)\, I(2u_1+u_2)\, \bar{N}^4 + cc \\
&+ 2\, I(-u_2)\, I(-u_2)\, I(u_2)\, I(u_2)\, \bar{N}^4 \\
&+ 2\, I(-u_2)\, I(u_2)\, \bar{N}^4 \\
&+ I(-2u_1)\, I(-u_2)\, I(-u_2)\, I(2u_1+2u_2)\, \bar{N}^4 + cc \\
&+ 2\, I(-2u_1-u_2)\, I(-u_2)\, I(u_2)\, I(2u_1+u_2)\, \bar{N}^4 \\
&+ I(-u_1)\, I(-u_1)\, I(2u_1)\, \bar{N}^3 + cc \\
&+ 2\, I(-u_1)\, I(-u_2)\, I(u_1+u_2)\, \bar{N}^3 + cc \\
&+ 2\, I(-u_1+u_2)\, I(u_1-u_2)\, \bar{N}^3 \\
&+ I(-u_1-u_2)\, I(-u_1-u_2)\, I(2u_1+2u_2)\, \bar{N}^3 + cc \\
&+ 2\, I(-u_1-2u_2)\, I(-u_1+u_2)\, I(2u_1+u_2)\, \bar{N}^3 + cc \\
&+ 2\, I(-u_1-2u_2)\, I(u_1+2u_2)\, \bar{N}^3 \\
&+ I(-u_2)\, I(-u_2)\, I(2u_2)\, \bar{N}^3 + cc \\
&+ I(-2u_1)\, I(-2u_2)\, I(2u_1+2u_2)\, \bar{N}^3 + cc \\
&+ 2\, I(-2u_1-u_2)\, I(2u_1+u_2)\, \bar{N}^3 \\
&+ 2\, \bar{N}^3 \\
&+ I(-u_1)\, I(-u_1)\, I(-u_2)\, I(-u_2)\, I(u_1+u_2)\, I(u_1+u_2)\, \bar{N}^6 + cc \\
&+ 2\, I(-u_1-u_2)\, I(-u_1)\, I(-u_2)\, I(u_2)\, I(u_1)\, I(u_1+u_2)\, \bar{N}^6 \,].
\end{aligned}
$$

The second moment of the imaginary part of the signal is given by

$$-1/4 < [\, D_p^{(TC)}(u_1,u_2) - D_p^{(TC)^*}(u_1,u_2)\,]^2 > \qquad \text{(A1.7)}$$

and averaging over the photon noise statistics gives

$$
\begin{aligned}
&-1/4\, [\, I(-u_1)\, I(-u_1)\, I(-u_2)\, I(-u_2)\, I(2u_1+2u_2)\, \bar{N}^3 + cc \\
&+ 2\, I(-u_1)\, I(-u_1)\, I(-u_2)\, I(u_1)\, I(u_1+u_2)\, \bar{N}^3 + cc
\end{aligned}
$$

$$
\begin{aligned}
&+ I(-u_1)\, I(-u_1)\, I(-2u_2)\, I(u_1+u_2)\, I(u_1+u_2)\, \bar{N}^5 + cc \\
&+ 2\, I(-u_1)\, I(-u_2)\, I(-u_2)\, I(u_2)\, I(u_1+u_2)\, \bar{N}^5 + cc \\
&- 2\, I(-u_1)\, I(-u_2)\, I(u_2)\, I(u_1)\, \bar{N}^5 \\
&- 2\, I(-u_1-u_2)\, I(-u_1)\, I(-u_2)\, I(u_1)\, I(u_1+2u_2)\, \bar{N}^5 + cc \\
&+ 2\, I(-u_1-u_2)\, I(-u_1)\, I(-u_2)\, I(u_1+u_2)\, I(u_1+u_2)\, \bar{N}^5 + cc \\
&- 2\, I(-u_1-u_2)\, I(-u_1)\, I(-u_2)\, I(u_2)\, I(2u_1+u_2)\, \bar{N}^5 + cc \\
&- 2\, I(-u_1-u_2)\, I(-u_1)\, I(u_1)\, I(u_1+u_2)\, \bar{N}^5 \\
&- 2\, I(-u_1-u_2)\, I(-u_1)\, I(u_2)\, I(u_1-u_2)\, I(u_1+u_2)\, \bar{N}^5 + cc \\
&+ I(-u_1-u_2)\, I(-u_1-u_2)\, I(u_2)\, I(u_2)\, I(2u_1)\, \bar{N}^5 + cc \\
&- 2\, I(-u_1-u_2)\, I(-u_2)\, I(u_2)\, I(u_1+u_2)\, \bar{N}^5 \\
&+ I(-u_1)\, I(-u_1)\, I(-2u_2)\, I(2u_1+2u_2)\, \bar{N}^4 + cc \\
&+ 2\, I(-u_1)\, I(-u_1)\, I(u_1)\, I(u_1)\, \bar{N}^4 \\
&+ 4\, I(-u_1)\, I(-u_2)\, I(u_2)\, I(u_1)\, \bar{N}^4 \\
&+ 2\, I(-u_1)\, I(-2u_2)\, I(u_2)\, I(u_1+u_2)\, \bar{N}^4 + cc \\
&- 2\, I(-u_1)\, I(u_1)\, \bar{N}^4 \\
&- 2\, I(-u_1)\, I(u_2)\, I(u_1-u_2)\, \bar{N}^4 + cc \\
&+ 2\, I(-u_1-u_2)\, I(-u_1)\, I(-u_2)\, I(2u_1+2u_2)\, \bar{N}^4 + cc \\
&+ 4\, I(-u_1-u_2)\, I(-u_1)\, I(u_1)\, I(u_1+u_2)\, \bar{N}^4 + cc \\
&- 2\, I(-u_1-u_2)\, I(-u_1)\, I(u_1-u_2)\, I(u_1+2u_2)\, \bar{N}^4 + cc \\
&+ 2\, I(-u_1-u_2)\, I(-u_1)\, I(u_2)\, I(2u_1)\, \bar{N}^4 + cc \\
&- 2\, I(-u_1-u_2)\, I(-u_1)\, I(2u_1+u_2)\, \bar{N}^4 + cc \\
&- 2\, I(-u_1-u_2)\, I(-u_1+u_2)\, I(-u_2)\, I(2u_1+u_2)\, \bar{N}^4 + cc \\
&- 2\, I(-u_1-u_2)\, I(-u_1+u_2)\, I(u_1-u_2)\, I(u_1+u_2)\, \bar{N}^4 \\
&- 2\, I(-u_1-u_2)\, I(-u_1-u_2)\, I(u_1+u_2)\, I(u_1+u_2)\, \bar{N}^4 \\
&+ I(-u_1-u_2)\, I(-u_1-u_2)\, I(2u_2)\, I(2u_1)\, \bar{N}^4 + cc \\
&- 2\, I(-u_1-u_2)\, I(-u_2)\, I(u_1+2u_2)\, \bar{N}^4 + cc \\
&+ 4\, I(-u_1-u_2)\, I(-u_2)\, I(u_2)\, I(u_1+u_2)\, \bar{N}^4 \\
&- 2\, I(-u_1-u_2)\, I(u_1+u_2)\, \bar{N}^4 + cc \\
&- 2\, I(-u_1-2u_2)\, I(-u_1)\, I(u_1)\, I(u_1+2u_2)\, \bar{N}^4 \\
&- 2\, I(-u_1-2u_2)\, I(-u_1)\, I(u_2)\, I(2u_1+u_2)\, \bar{N}^4 + cc \\
&+ 2\, I(-u_2)\, I(-u_2)\, I(u_2)\, I(u_2)\, \bar{N}^4 \\
&- 2\, I(-u_2)\, I(u_2)\, \bar{N}^3 \\
&+ I(-2u_1)\, I(-u_2)\, I(-u_2)\, I(2u_1+2u_2)\, \bar{N}^4 + cc \\
&- 2\, I(-2u_1-u_2)\, I(-u_2)\, I(u_2)\, I(2u_1+u_2)\, \bar{N}^4 \\
&+ I(-u_1)\, I(-u_1)\, I(2u_1)\, \bar{N}^3 + cc
\end{aligned}
$$

$$
\begin{aligned}
&+ 2\, I(-u_1)\, I(-u_2)\, I(u_1+u_2)\, \bar{N}^3 + cc \\
&- 2\, I(-u_1+u_2)\, I(u_1-u_2)\, \bar{N}^3 \\
&+ I(-u_1-u_2)\, I(-u_1-u_2)\, I(2u_1+2u_2)\, \bar{N}^3 + cc \\
&- 2\, I(-u_1-2u_2)\, I(-u_1+u_2)\, I(2u_1+u_2)\, \bar{N}^3 + cc \\
&- 2\, I(-u_1-2u_2)\, I(u_1+2u_2)\, \bar{N}^3 \\
&+ I(-u_2)\, I(-u_2)\, I(2u_2)\, \bar{N}^3 + cc \\
&+ I(-2u_1)\, I(-2u_2)\, I(2u_1+2u_2)\, \bar{N}^3 + cc \\
&- 2\, I(-2u_1-u_2)\, I(2u_1+u_2)\, \bar{N}^3 \\
&- 2\, \bar{N}^3 \\
&+ I(-u_1)\, I(-u_1)\, I(-u_2)\, I(-u_2)\, I(u_1+u_2)\, I(u_1+u_2)\, \bar{N}^4 + cc \\
&- 2\, I(-u_1-u_2)\, I(-u_1)\, I(-u_2)\, I(u_2)\, I(u_1)\, I(u_1+u_2)\, \bar{N}^4 \,].
\end{aligned}
$$

The first joint moment of the real and imaginary parts of the signal is given by

$$
\begin{aligned}
-J/4 < [\; & D_p^{(TC)}(u_1,u_2) - D_p^{(TC)^*}(u_1,u_2) \;] \\
& .[\; D_p^{(TC)}(u_1,u_2) + D_p^{(TC)^*}(u_1,u_2) \;]>
\end{aligned}
\qquad \text{(A1.8)}
$$

and averaging over the photon noise statistics gives

$$
\begin{aligned}
&-J/4\, [\; - I(-u_1)\, I(-u_1)\, I(-u_2)\, I(-u_2)\, I(2u_1+2u_2)\, \bar{N}^3 - cc \\
&- 2\, I(-u_1)\, I(-u_1)\, I(-u_2)\, I(u_1)\, I(u_1+u_2)\, \bar{N}^3 - cc \\
&- I(-u_1)\, I(-u_1)\, I(-2u_2)\, I(u_1+u_2)\, I(u_1+u_2)\, \bar{N}^3 - cc \\
&- 2\, I(-u_1)\, I(-u_2)\, I(-u_2)\, I(u_2)\, I(u_1+u_2)\, \bar{N}^3 - cc \\
&- 2\, I(-u_1-u_2)\, I(-u_1)\, I(-u_2)\, I(u_1+u_2)\, I(u_1+u_2)\, \bar{N}^3 - cc \\
&+ I(-u_1-u_2)\, I(-u_1-u_2)\, I(u_2)\, I(u_2)\, I(2u_1)\, \bar{N}^3 - cc \\
&- I(-u_1)\, I(-u_1)\, I(-2u_2)\, I(2u_1+2u_2)\, \bar{N}^3 - cc \\
&- 2\, I(-u_1)\, I(-2u_2)\, I(u_2)\, I(u_1+u_2)\, \bar{N}^3 - cc \\
&- 2\, I(-u_1-u_2)\, I(-u_1)\, I(-u_2)\, I(2u_1+2u_2)\, \bar{N}^3 - cc \\
&+ 2\, I(-u_1-u_2)\, I(-u_1)\, I(u_2)\, I(2u_1)\, \bar{N}^3 - cc \\
&+ I(-u_1-u_2)\, I(-u_1-u_3)\, I(2u_2)\, I(2u_1)\, \bar{N}^3 - cc \\
&- I(-2u_1)\, I(-u_2)\, I(-u_2)\, I(2u_1+2u_2)\, \bar{N}^3 - cc \\
&+ I(-u_1)\, I(-u_1)\, I(2u_1)\, \bar{N}^3 - cc \\
&+ 2\, I(-u_1)\, I(-u_2)\, I(u_1+u_2)\, \bar{N}^3 - cc \\
&- I(-u_1-u_2)\, I(-u_1-u_2)\, I(2u_1+2u_2)\, \bar{N}^3 - cc
\end{aligned}
$$

$$+ I(-u_3)\, I(-u_3)\, I(2u_3)\, \overline{N}^3 - cc$$

$$- I(-2u_1)\, I(-2u_2)\, I(2u_1+2u_2)\, \overline{N}^3 - cc$$

$$- I(-u_1)\, I(-u_1)\, I(-u_2)\, I(-u_2)\, I(u_1+u_2)\, I(u_1+u_2)\, \overline{N}^3 - cc\ ].$$

Appendix (2)

Centroiding frames before performing the KT technique results in errors being introduced into the ensemble average when photon noise is present.

The pth low light level image is described by Eq.(18) and its Fourier transform by Eq.(19). The following expression maybe written relating the shift, X_p, from the image centroid of the photon event distribution. The image centroid being the 'centre of gravity' of the image photon event distribution.

$$N_p\,(X_p - x_g) = \sum_{k=1}^{N_p} (x_k - x_g), \tag{A2.1}$$

where x_g is any point in the frame used as a reference. Hence,

$$X_p = \frac{\sum_{k=1}^{N_p} x_k}{N_p}. \tag{A2.2}$$

The KT signal in Fourier space is

$$D_p(u_1)\, D_p^*(u_1+\Delta u) - D_p^*(\Delta u), \tag{A2.3}$$

and if $D_p(u)$ is centroided, using the Fourier shift theorem, to give,

$$D_p(u)\exp(-2\pi/X_p u), \tag{A2.4}$$

then the resulting KT signal formed is

$$D_p(u_1)\exp(-2\pi/X_p u_1)\, D_p^*(u_1+\Delta u)\exp(2\pi/X_p(u_1+\Delta u)$$
$$- D_p^*(\Delta u)\exp(2\pi/X_p \Delta u). \tag{A2.5}$$

Using the method of Goodman and Belsher [18] the ensemble average over the photon event distribution yields

$$< N_p\,(N_p-1)\, f(u+\frac{\Delta u}{N_p})\, f^*(u+\Delta u-\frac{\Delta u}{N_p})\, f^*(\frac{\Delta u}{N_p})^{N_p-2} >$$
$$- < N_p\, f^*(\Delta u-\frac{\Delta u}{N_p})\, f(\frac{\Delta u}{N_p})^{N_p-1} >$$
$$+ < N_p\, f^*(\Delta u-\frac{\Delta u}{N_p})\, f(\frac{\Delta u}{N_p})^{N_p-1} > \tag{A2.6}$$

where $\hat{I}(u)$ is the object Fourier transform, $I(u)$, normalised by $I(0)$ and $< >$ indicates an ensemble average over the Poisson statistics of the photon events. Obviously the bias terms cancel as desired. However, the resulting signal differs from the required result,

$$< N_p(N_p-1)\, \hat{I}(u_1)\, \hat{I}^*(u_1+\Delta u) >, \tag{A2.7}$$

obtained from a series of photon limited images of a stationary object which is not centroided before performing the KT average. The average over the bias term alone yields a result which is completely general for any frequency Δu. Consequently the same result maybe used to describe the resulting image obtained by summing a series of centroided images which contain photon noise.

$$< E[D_p(u)\exp(-2\pi i X_p u)] > = < N_p\, \hat{I}(u-\frac{u}{N_p})\, \hat{I}^*(\frac{u}{N_p})^{N_p-1} > \tag{A2.8}$$

where $E[]$ indicates the expectation value of the signal due to the photon event distribution.

Appendix (3)

Roddier[16] has developed a model which may be extended, in conjunction with some simple assumptions concerning the statistics of atmosphere induced wavefront perturbations, to approximate the effect of atmospheric turbulence on ensemble averages of intensity distribution correlations in general.

Imaging through atmospheric turbulence with a large single aperture telescope is modelled by describing the telescope pupil function, $H_o(x)$, as a distribution of 'seeing cells' of diameter r_o. The wavefront phase is assumed constant across each cell and the complex amplitude in the pupil, $A(x)$, is assumed uncorrelated between cells. The complex amplitude modulus is assumed to be unity. The Fourier transform of the intensity distribution of an image of a point source is therefore described by,

$$S_p(u) = \frac{\int_{pupil} H_o(x)\, H_o^*(x+\lambda u)\, A(x)\, A^*(x+\lambda u)\, dx}{\int_{pupil} |H_o(x)|^2\, dx}. \qquad (A3.1)$$

This integral may be approximated, using the simple model, by a sum of complex exponentials corresponding to the complex amplitude difference between pairs of 'seeing cells'.

$$S_p(u) = \frac{1}{N(0)} \sum_{s=1}^{N(u)} \exp[j(\Phi_s - \Phi_s')] \qquad (A3.2)$$

where $\Phi_s - \Phi_s'$ is the wavefront phase difference between the sth pair of 'seeing cells' separated by λu. There are approximately $N(u)$ such pairs in the pupil.

In order to study the signal to noise ratios of the KT and TC techniques a number of different correlations need to be averaged over the atmospheric statistics. Using the above model a particular correlation is treated to try to indicate the form of the approximations required in general. These and similar approximations are used to average all the correlations needed for the investigation allowing the form of the dominant terms to be determined.

Consider, as an example, averaging the modulus squared of the bispectrum of a point source, for frequencies u_1, $u_2 > r_o/\lambda$. This term is of particular importance as it

allows the variance of the bispectrum to be evaluated.

$$< |S_p(u_1)\, S_p^*(u_1+u_2)\, S_p(u_2)|^2 >$$

$$= < \frac{1}{N(0)^6} \sum_{q=1}^{N(u_1)} \sum_{r=1}^{N(u_1+u_2)} \sum_{s=1}^{N(u_2)} \exp[j(\Phi_q - \Phi'_q) + j(\Phi_r - \Phi'_r) + j(\Phi_s - \Phi'_s)]$$

$$\cdot \sum_{q'=1}^{N(u_1)} \sum_{r'=1}^{N(u_1+u_2)} \sum_{s'=1}^{N(u_2)} \exp[j(\Phi'_{q'} - \Phi_{q'}) + j(\Phi'_{r'} - \Phi_{r'}) + j(\Phi'_{s'} - \Phi_{s'})] > \qquad (A3.3)$$

In general, this expression corresponds to summing over contributions from six different pairs of 'seeing cells' and for such combinations the ensemble average tends to zero. However, certain other combinations, for which 'seeing cells' occur in more than one pair, result in 'phase closure' and a non-zero ensemble average contribution. Such combinations all result in the phase closure relationship

$$(\Phi_q - \Phi'_q) + (\Phi_r - \Phi'_r) + (\Phi_s - \Phi'_s)$$

$$+ (\Phi'_{q'} - \Phi_{q'}) + (\Phi'_{r'} - \Phi_{r'}) + (\Phi'_{s'} - \Phi_{s'}) = 0. \qquad (A3.4)$$

which may be realised in a number of different ways. To see how these arise and to obtain their contribution to the ensemble average it is instructive to consider imaging through a telescope pupil with an atmosphere induced complex amplitude distribution which is delta correlated.

$$C_A(x) = < A(x')\ A^*(x'+x) > = \delta(x) \qquad (A3.5)$$

This corresponds to making $N(0)$ approach infinity so that the summation approximation of eqn. (A3.3) again becomes an integral expression.

$$< |S_p(u_1)\, S_p^*(u_1+u_2)\, S_p(u_2)|^2 >$$

$$= \frac{1}{Y} \iiint\!\!\iiint H_o(x_1)\, H_o^*(x_1+\lambda u_1)\, H_o(x_2)\, H_o^*(x_1-\lambda(u_1+u_2))\, H_o(x_3)\, H_o^*(x_3+\lambda u_2)$$

$$\cdot H_o^*(x_4)\, H_o(x_4+\lambda u_1)\, H_o^*(x_5)\, H_o(x_5-\lambda(u_1+u_2))\, H_o^*(x_6)\, H_o(x_6+\lambda u_2)$$

$$< A(x_1)\, A^*(x_1+\lambda u_1)\, A(x_2)\, A^*(x_2-\lambda(u_1+u_2))\, A(x_3)\, A^*(x_3+\lambda u_2)\, A^*(x_4)\, A(x_4+\lambda u_1)$$

$$A^*(x_5)\, A(x_5-\lambda(u_1+u_2))\, A^*(x_6)\, A(x_6+\lambda u_2) > dx_1\, dx_2\, dx_3\, dx_4\, dx_5\, dx_6.$$

where the normalisation factor Y is defined by

$$Y = \left[\iiint |H_o(x_1)|^2\, |H_o(x_2)|^2\, |H_o(x_3)|^2\, dx_1\, dx_2\, dx_3 \right]^2 \qquad (A3.6)$$

By averaging over the complex amplitude statistics the phase closure non-zero ensemble average contribution terms can be approximated. Since the complex amplitude is assumed to possess unit modulus its higher moments cannot be generated using Reed's theorem [31] which is only applicable if the complex amplitude is a gaussian random variable. Instead the high order moment is broken down into combinations of lower order moments on the basis of phase closure considerations. This break down of the higher order moments is perhaps more easily seen if the phase closure relationship is thought of in terms of spatial frequency vectors forming closed loops in the telescope pupil, see Fig.14.

(a) Consider terms for which

$$(\Phi_q - \Phi'_q) + (\Phi'_{q'} - \Phi_{q'}) = 0,$$

$$(\Phi_r - \Phi'_r) + (\Phi'_{r'} - \Phi_{r'}) = 0,$$

$$(\Phi_s - \Phi'_s) + (\Phi'_{s'} - \Phi_{s'}) = 0,$$

These correspond to the following non-zero contribution to the ensemble average over the complex amplitude statistics, see Fig.14(b).

$$< A(x_1)\, A^*(x_4) > < A(x_4+\lambda u_1)\, A^*(x_1+\lambda u_1) > < A(x_2)\, A^*(x_5) >$$

$$. < A(x_5-\lambda(u_1+u_2))\, A^*(x_2-\lambda(u_1+u_2)) > < A(x_3)\, A^*(x_6) > < A(x_6+\lambda u_2)\, A^*(x_3+\lambda u_2) >$$

$$= \delta(x_4-x_1)\, \delta(x_5-x_2)\, \delta(x_6-x_3) \qquad \text{(A3.7)}$$

Resulting in the following contribution to the average modulus squared of the bispectrum which is non-zero for all spatial frequencies out to the diffraction limit of the telescope. For an unapodised aperture this is simplified to a product of terms dependent on the normalised diffraction limited transfer function, $T^{(2)}(u)$.

$$\frac{1}{V} \int_{pupil} \int\int |H_o(x_1)|^2\, |H_o(x_1+\lambda u_1)|^2\, |H_o(x_2)|^2\, |H_o(x_1-\lambda(u_1+u_2))|^2\, |H_o(x_3)|^2\, |H_o(x_3+\lambda u_2)|^2\, dx_1\, dx_2\, dx_3.$$

$$= \frac{1}{\bar{n}_s^3}\, T^{(2)}(u_1)\, T^{(2)}(u_2)\, T^{(2)}(u_1+u_2) \qquad \text{(A3.8)}$$

where the mean number of speckles per frame, $\bar{n}_s$ is defined by

$$\bar{n}_s \approx \frac{\int_{pupil} |H_o(x)|^2\, dx}{\int_{-\infty}^{\infty} |C_A(x)|^2\, dx}$$

(b) Consider terms for which

$$(\Phi_q - \Phi'_q) + (\Phi'_{q'} - \Phi_{q'}) = 0,$$

$$(\Phi_r - \Phi'_r) + (\Phi'_{r'} - \Phi_{r'}) + (\Phi_s - \Phi'_s) + (\Phi'_{s'} - \Phi_{s'}) = 0,$$

These correspond to two terms, see Fig.14(c), that have identical non-zero contributions to the ensemble average over the complex amplitude statistics, provided the pupil is symmetric.
For example,

$$< A(x_1)\, A^*(x_4) > < A(x_4+\lambda u_1)\, A^*(x_1+\lambda u_1) > < A(x_2)\, A^*(x_6) >$$

$$. < A(x_3)\, A^*(x_2-\lambda(u_1+u_2)) > < A(x_5-\lambda(u_1+u_2))\, A^*(x_3+\lambda u_2) > < A(x_6+\lambda u_2)\, A^*(x_5) >$$

$$= \delta(x_4-x_1)\, \delta(x_6-x_2)\, \delta(x_5-x_6-\lambda u_2)\, \delta(x_2-x_3-\lambda(u_1+u_2))\, \delta(x_3-x_5-\lambda(u_1+u_2)-\lambda u_2). \qquad \text{(A3.9)}$$

results in the following contribution to the average modulus squared of the bispectrum which is non-zero for all spatial frequencies out to the diffraction limit of the telescope. This simplifies for the case of an unapodised aperture to a product of terms dependent on the normalised diffraction limited transfer function, $T^{(2)}(u)$, and the normalised overlap integral, $T^{(4)}(u_2, u_1+u_2)$, of four pupils with separations from an arbitrary origin of zero, λu_2, $\lambda(u_1+u_2)$ and $\lambda(u_1+u_2)+\lambda u_2$.

$$\frac{1}{Y} \int_{\text{pupil}} |H_\phi(x_1)|^2\, |H_\phi(x_1+\lambda u_1)|^2\, dx_1$$

$$. \int_{\text{pupil}} |H_\phi(x_2)|^2\, |H_\phi(x_2-\lambda u_1)|^2\, |H_\phi(x_1-\lambda(u_1+u_2))|^2\, |H_\phi(x_2+\lambda u_2)|^2\, dx_2$$

$$\approx \frac{1}{\pi_\phi^4}\, T^{(2)}(u_1)\, T^{(4)}(u_2, u_1+u_2) \qquad \text{(A3.10)}$$

The symmetry of the bispectrum squared modulus results in further terms for the same phase closure realisation, namely

$$\frac{2}{\pi_\phi^4}\, T^{(2)}(u_2)\, T^{(4)}(u_1, u_1+u_2) \quad \text{and} \quad \frac{2}{\pi_\phi^4}\, T^{(2)}(u_1+u_2)\, T^{(4)}(u_1, u_2). \qquad \text{(A3.11)}$$

(c) Consider terms for which

$$(\Phi_q - \Phi'_q) + (\Phi_r - \Phi'_r) + (\Phi_s - \Phi'_s) = 0,$$

$$(\Phi'_{q'} - \Phi_{q'}) + (\Phi'_{r'} - \Phi_{r'}) + (\Phi'_{s'} - \Phi_{s'}) = 0,$$

These correspond to four terms that have identical non-zero contributions to the ensemble average over the complex amplitude statistics. For example,

$$< A(x_3)\, A^*(x_1+\lambda u_1) > < A(x_1)\, A^*(x_2-\lambda(u_1+u_2)) > < A(x_2)\, A^*(x_3+\lambda u_2) >$$

$$< A(x_4+\lambda u_1)\, A^*(x_6) > < A(x_5-\lambda(u_1+u_2))\, A^*(x_4) > < A(x_6+\lambda u_2)\, A^*(x_5) >$$

$$= \delta(x_1-x_3+\lambda u_1)\, \delta(x_2-x_1-\lambda(u_1+u_2))\, \delta(x_3-x_2+\lambda u_2)\, \delta(x_6-x_4-\lambda u_1)$$

$$.\delta(x_4-x_5+\lambda(u_1+u_2))\, \delta(x_5-x_6-\lambda u_2) \qquad \text{(A3.12)}$$

Another example is shown diagrammatically in Fig.14(d) Again a diffraction limited contribution results which, after combining all terms, is simplified by considering an unapodised aperture, to yield

$$\left[\frac{2}{\Upsilon} \int_{\text{pupil}} |H_o(x_1)|^2\, |H_o(x_1+\lambda u_1)|^2\, |H_o(x_1+\lambda(u_1+u_2))|^2\, dx_1 \right]^2$$

$$= \frac{4}{\pi_o^4}\, T^{(3)}(u_1,u_2)\, T^{(3)}(u_1,u_2) \qquad \text{(A3.13)}$$

The normalised diffraction limited bispectral transfer function $T^{(3)}(u_1,u_2)$ is the overlap integral of three pupils with separations from an arbitrary origin of zero, λu_1 and $\lambda(u_1+u_2)$.

The closure phase realisation being considered in this section has some redundancy with the previous realisations, (a) and (b). For example, in eqn. (A3.10) if $x_1+\lambda u_1 = x_2$ then the phase closure conditions of (c) are realised. The redundancy must therefore be eliminated by subtracting the relevent duplicated terms. In this example this corresponds to subtracting

$$\frac{2}{\pi_o^2}\, T^{(4)}(u_2,u_1+u_2).$$

Compensating for all the redundancy requires subtracting the following.

$$\frac{4}{\pi_o^2} \left[T^{(4)}(u_2,u_1+u_2) + T^{(4)}(u_1,u_1+u_2) + T^{(4)}(u_1,u_2) \right] + \frac{2}{\pi_o^2}\, T^{(3)}(u_1,u_2) \qquad \text{(A3.14)}$$

Figures 14(e) and 14(f) shown examples of phase closure relations which shown redundancy.

(d) Finally, consider realising the closure phase of eqn. (A3.4) without any of the equality conditions of (a) - (c) being true. Averaging over the complex amplitudes

yields 40 terms which have the following, identical, non-zero contributions to the ensemble average provided the pupil is symmetric.

$$\frac{1}{Y}\int_{\text{pupil}} |H_o(x_1)|^4\,|H_o(x_1+\lambda u_1)|^4\,|H_o(x_1+\lambda(u_1+u_2))|^4\,dx_1$$

$$\approx \frac{T^{(3)}(u_1,u_2)}{\pi_o^3} \qquad \text{(A3.15)}$$

The ensemble averaged modulus squared of the bispectrum therefore consists of a sum of many terms with, in particular differing dependencies on π_o. However, it has been assumed that π_o is very much greater then unity and so in this limit terms which are inversely proportional to the lowest power of π_o will easily dominate. In this example the contribution of the term defined by Eq.(A3.8) will dominate all others.

This approach has been applied to all the ensemble averages over the atmospheric statistics required for the SNR study.

REFERENCES

[1] Roddier F., "The effects of atmospheric turbulence in optical astronomy", p.281-376, in Progress in Optics, ed. E. Wolf, North Holland (1981).

[2] Fried D.L., J. Opt. Soc. Am. 56. p.1372 (1966).

[3] Labeyrie A., "Attainment of diffraction limited resolution in large telescopes by Fourier analysing speckle patterns in star images", Astron. Astrophys., 6, p85-87 (1970)

[4] Dainty J.C., "Diffraction limited imaging of stellar objects using telescopes of low optic quality", Opt. Commun., 7, p.129-134 (1973).

[5] Dainty J.C., Fienup J.R., "Phase retrieval and image reconstruction for astronomy", p.231-275, in Image Recovery, ed. H.Stark, Academic Press (1987)

[6] Knox K.T., Thompson B.J., "Recovery of images from atmospherically degraded short exposure photographs", Astron. J., 193, L45-L48 (1974).

[7] Knox K.T., "Image retrieval from astronomical speckle patterns", J. Opt. Soc. Am., 66, p.1236-1239 (1976).

[8] Weigelt G., "Modified speckle interferometry : speckle masking", Opt. Commun., 21, p.55 (1977).

[9] Lohmann A.W., Weigelt G.P., Wirnitzer B., "Speckle masking in astronomy - triple correlation theory and applications", Appl. Opt., 22, p.4028 (1983).

[10] Weigelt G.P., Wirnitzer B., "Image reconstruction by the speckle masking method", Opt. Lett., 8, p.389 (1983).

[11] Jennison R.C., "A phase sensitive interferometer technique for the measurement of the Fourier transforms of spatial brightness distribution of small angular extent", Mon. Not. Roy. Astr. Soc., 118, p.276 (1958).

[12] Fienup J.R., Opt. Lett. 3 27 (1978).

[13] Brames B.J., Dainty J.C., "A method of determining object intensity distributions in stellar speckle interferometry", J. Opt. Soc. Am., 71, p.1542-1545 (1981).

[14] Bartelt H., Lohmann A.W., Wirnitzer B., "Phase and amplitude recovery from bispectra", Appl. Opt., 23, p.3121-3129 (1984).

[15] Hege E.K., Hubbard N.E., Strittmatterr P.A., Worden S.P., Astrophys. J., 248, L1 (1981).

[16] Roddier F., "Triple correlation as a phase closure tehnique", Opt. Commun., 60, 3, p.145-148 (1986).

[17] Baldwin J.E., Haniff C.A., Mackay C.D., Warner P.J., "Closure phase in high resolution optical imaging", Nature, 320, p.595-597 (1986).

[18] Goodman J.W., Belsher J.F., "Photon limited images and their restoration", RADC-TR-76-50, March, 1976; "Precompensation and postcompensation of photon limited degraded images", RADC-TR-76-382, Dec., 1976; "Photon limitations in imaging and restoration", RADC-TR-77-175, May, 1977. All ARPA Order no.2646, (Rome Air Development Center, Griffiss AFB, NY 13441.

[19] Dainty J.C., Greenaway A.H., "Estimation of spatial power spectra in speckle interferometry", J. Opt. Soc. Am., 69, 5, p786-790 (1979).

[20] Koechlin L., "Observational speckle interferometry", Proc. IAU Colloq. No.50 (1978).

[21] Papaliolios C., Mertz L., "A new two dimensional photon camera", Proc. SPIE 331 p360-365 (1982).

[22] Nisenson P., Papaliolios, "Effects of photon noise on speckle image reconstruction with the Knox and Thompson algorithm", Opt. Commun., 47, p.91-96 (1983).

[23] Wirnitzer B., "Bispectral analysis at low light levels and astronomical speckle masking", J. Opt. Soc. Am., 2, p.14-21 (1985).

[24] Fontanella J.C., Seve A., "Reconstruction of turbulence degraded images using the Knox-Thompson algorithm", J. Opt. Soc. Am. A, 4, p.438-448 (1987).

[25] Hofmann K.-H., Weigelt G., "Speckle masking observation of the central object in the giant H II region NGC3603*", Astron. Astrophys. 167, L15-L16 (1986).

[26] Aitken G., Houtman R., Johnson R., Pochet J.M., "Direct phase gradient measurement for speckle image reconstruction", Appl. Opt. 25, p.1031 (1986).

[27] Aitken G., Houtman R., Johnson R., "Phase gradient speckle image processing: digital implementation and noise bias terms", Appl. Opt., 25 (1986).

[28] Northcott M.J., Ayers G.R, Dainty J.C, "Algorithms for image reconstruction for photon-limited data using the triple correlation", in preparation for J. Opt. Soc. Am. A.

[29] Dainty J.C., Northcott M.J., "Imaging a randomly translating object at low light levels using the triple correlation", Opt. Commun., 58, p.11-14 (1986).

[30] Ayers G.R., Dainty J.C., Northcott M.J., "Photon limited imaging through turbulence", Proc. SPIE, issue unknown (1987).

[31] Reed I.S., "On a moment theorem for complex gaussian processes", IRE Transactions on information theory, IT-8, 194 (1962)

Figure captions

Figure (1) : Corresponding sub-planes of (a) the bispectrum ($u_1=u_{1x}$, $u_2=u_{2x}$) and (b) the KT ($u_1=u_{1x}$, $\Delta u=\Delta u_x$) four dimensional transfer functions of a circular aperture lens.

Figure (2) : Pictorial representation of correlation techniques in the image plane. (a) The autocorrelation, (b) the Knox-Thompson correlation for a single plane, $\Delta u=\Delta u_x$, (c) a single bispectrum plane, $u_2=2\Delta u=2\Delta u_x$, represented as a double correlation in the image plane, and (d) correlations required for phase-gradient technique, $a=a_x$. The asterisk (*) indicates the correlation of the two dimensional images and multiplication by a function is indicated by the overlayed dashed axes and 1-D function. The functions are constant in the orthogonal direction. The real and imaginary parts of the correlations are shown separately.

Figure (3) : Plots (a) shows the theoretical error, Θ_B, for a single image, on the phase difference estimates resulting from using the bispectrum plane ($u_{2x}=\Delta u_x$, $u_{1y}=u_{2y}=0$) and the KT plane ($u_{1y}=0$, $\Delta u_y=0$). The signal to noise ratio, SNR_m, for the same two planes, are shown in (b). Plots (a) and (b) are on a natural logarithmic scale. The results are for an 'asteroid' type object which is shown in (c), together with its Fourier modulus.

Figure (4) : Graph (a) compares the phase error on corresponding cross sections of the bispectrum ($u_1=u_{1x}$, $u_2=u_{2x}$) and the Knox-Thompson ($u_1=u_{1x}$, $\Delta u=\Delta u_x$) sub-planes for $u_{2x}=\Delta u_x=4$ frequency sampling intervals. Graph (b) compares the SNR_m of the same two cross-sections of the KT and bispectrum sub-planes.

Figure (5) : Plots of the ratio of Θ_B, defined by Eq.(30), to $1/(\sqrt{2}SNR_m)$ for (a) the bispectrum plane defined by $u_{2x}=\Delta u_x$, $u_{1y}=u_{2y}=0$, and (b) the KT plane defined by $u_{1y}=0$, $\Delta u_y=0$. Departure of the ratio from unity only occurs near the axes.

Figure (6) : Diagrammatic representation of systems of pupil sub-apertures, of diameter r_o, showing how 'phase closure' is realised. The phase closure requirement can be redefined in terms of spatial frequency vectors forming a closed loop. (a) Vectors contributing to Fourier spatial frequency u. (b) Phase closure is achieved in the power spectrum by taking pairs of vectors of opposite sign, $-u$ and $+u$, to form a closed loop. (c) Approximate phase closure is achieved in the Knox and Thompson method by taking two vectors, u and $u+\Delta u$, and assuming that the pupil phase is constant over Δu. The bispectrum adds a third vector Δu to explicitly form phase closure. (d) The third vector, Δu, is essential for phase closure when $\lambda\Delta u > r_o$. The KT method fails with this arrangement.

Figure (7) : The graphs illustrate the retention of phase information in the KT and TC techniques. The results have been obtained using a computer simulation of imaging a point source through a 2 metre telescope and approximately 0.7 arc second seeing at high light level. The point source is centroided and so has zero Fourier phase at all spatial frequencies. The phase distribution statistics are obtained using an ensemble of 5000 different atmospheric realisations. The fluctuation of phase between frames is plotted for the first 150 realisations only. The telescope pupil consists of three widely spaced sub-apertures of diameter r_o. Graphs (a) show the uniformly distributed Fourier phase associated with spatial frequencies greater than r_o/λ. Graphs (b) and (d) show Fourier phase difference information is retained using both the KT and TC techniques for $\Delta u < r_o/\lambda$. Graph (c) shows Fourier phase information is lost if the KT is used with $\Delta u > r_o/\lambda$. Graph (e) shows phase difference information is again retained, even though $\Delta u > r_o/\lambda$, due to the phase closure property of the bispectrum.

Figure (8) : Plots showing the moduli of corresponding sub-planes of (a) the bispectrum ($u_1=u_{1x}, u_2=u_{2x}$) and (b) the KT ($u_1=u_{1x}, \Delta u=\Delta u_x$) four dimensional transfer functions for imaging through a 2 metre telescope with approximately 0.7 arc second 'seeing'. The data was obtained using a Monte Carlo computer simulation, generating 10000 independent realisations of the atmosphere to obtain the ensemble average. Both (a) and (b) are plotted using the same natural logarithmic scale.

Figure (9) : Graphs (a) and (b) respectively, show corresponding cross sections through the bispectrum ($u_1=u_{1x}$, $u_2=u_{2x}$) and the Knox-Thompson ($u_1=u_{1x}$, $\Delta u=\Delta u_x$) sub-

planes of their atmosphere-telescope combination transfer functions. The cross-sections correspond to frequency difference vectors, u_{2x}, Δu_x, of 0, 2, 4, 6, and 8 frequency sampling intervals. The telescope cutoff occurs at 50 and r_o/λ at approximately 4.5 frequency sampling intervals.

Figure (10) : Plots of the ratio of the phase error Θ_E to $1/(\sqrt{2}SNR_m)$ for the sub planes of the KT and bispectrum of the 'asteroid' type object shown in Fig.3(c) defined by $u_1=u_{1x}$, $u_2=u_{2x}$, $\Delta u=\Delta u_x$. These plots are the result of computationally simulating the effect of imaging the 'asteroid' shown in Fig.3(c) with a 2 metre telescope and 0.7 arc second 'seeing'. Departure from unity only occurs near the axes.

Figure (11) : plots of a single plane of the KT, (a), and bispectrum, (b), ($u_1=u_{1x}$, $u_2=u_{2x}$, $\Delta u=\Delta u_x$) SNR's at high light level obtained using the computer simulation to obtain ensemble averages over 10,000 independent realisations of atmospheric turbulence.

Figure (12) : Graphs (a) and (b) respectively, show corresponding cross sections through the Knox-Thompson ($u_1=u_{1x}$, $\Delta u=\Delta u_x$) and the bispectrum ($u_1=u_{1x}$, $u_2=u_{2x}$) sub-planes of their SNR's shown in Fig.11. The cross-sections correspond to frequency difference vectors, u_{2x}, Δu_x, of 0, 2, 4, 6, and 8 frequency sampling intervals. The telescope cutoff occurs at 50 and r_o/λ at approximately 4.5 frequency sampling intervals.

Figure (13) : The graphs in this figure are the results of a Monte Carlo computer simulation whereby ensemble averages over the atmospheric statistics have been carried out on the photon noise dependent variances defined in Appendix(1). Graph (a) shows the dependency of the SNR of the bispectrum on $\bar{n}_s$ and $\bar{N}$. The relative SNR is the ratio of the SNR for the bispectrum point defined by $u_1=0.4D/\lambda$, $u_2=0$ at $r_o \approx 0.185D$ to that at $r_o \approx 0.095D$. This ratio of r_o corresponds to a ratio of 0.25 in the mean number of speckles per frame, $\bar{n}_s$. The plot tends to 4 at very low light level, corresponding to a $1/\bar{n}_s$ dependency, see Eqs.(76), (77), and tends to unity at high light level, corresponding to a SNR which is approximately independent of $\bar{n}_s$, see Eq.(66). Graph (b) shows an equivalent plot to (a) for the bispectrum point defined by

u_1=0.6D/λ, u_2=0.3D/λ. The plot tends to a value of 16 at very low light level, corresponding to a $1/\bar{n}_s^2$ dependency, see Eq.(75) and tends to 2 at high light level, corresponding to a $1/\sqrt{\bar{n}_s}$ dependency, see Eq(66). Graph (c) shows the approximate linear dependence upon $\bar{N}$ of the SNR of the same bispectrum point when the mean number of photons per speckle is approximately one. The mean number of speckles per image, $\bar{n}_s$, in this example is approximately 1000. Graph (d) shows the approximate $\bar{N}^{3/2}$ dependency of the same bispectrum point when the mean number of photons per speckle is very much less than unity. See Eq.(75). The upper line is a $\bar{N}^{3/2}$ dependent reference. Graph (e) shows the linear dependence on $\bar{N}$ at very low light level of the SNR's of the KT and TC signals defined by u_1=0.4D/λ, u_2=0 Δu=0. See Eqs.(76),(77). The upper line is a linear reference. The KT signal has the slightly higher SNR, however the lines appear to be superimposed.

Figure (14) : Phase closure relationships can be viewed in terms of spatial frequency vectors forming closed loops in the telescope pupil. Diagram (a) shows a representation of the 6 vectors which need to be considered when analysing the modulus squared of the bispectrum at a point defined by u_1, u_2. Diagram (b) shows how the vectors can be selected in conjugate pairs to cancel the phase. Each pair being analogous to the power spectrum at that particular frequency. Diagrams (c) and (d) show other possible combinations of vectors which result in phase closure. Diagrams (e) and (f) show redundent configurations between those represented in (b)-(d).

(a)

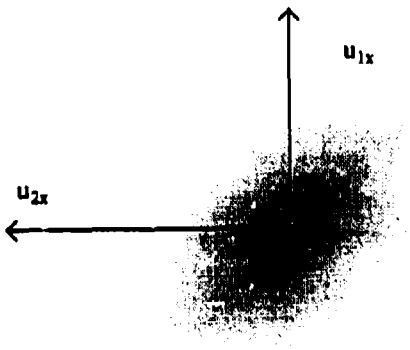

(b)

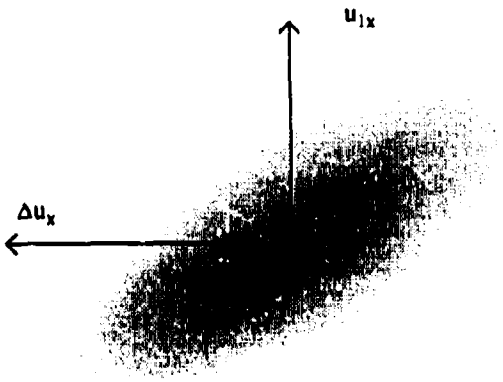

0.0 1.0

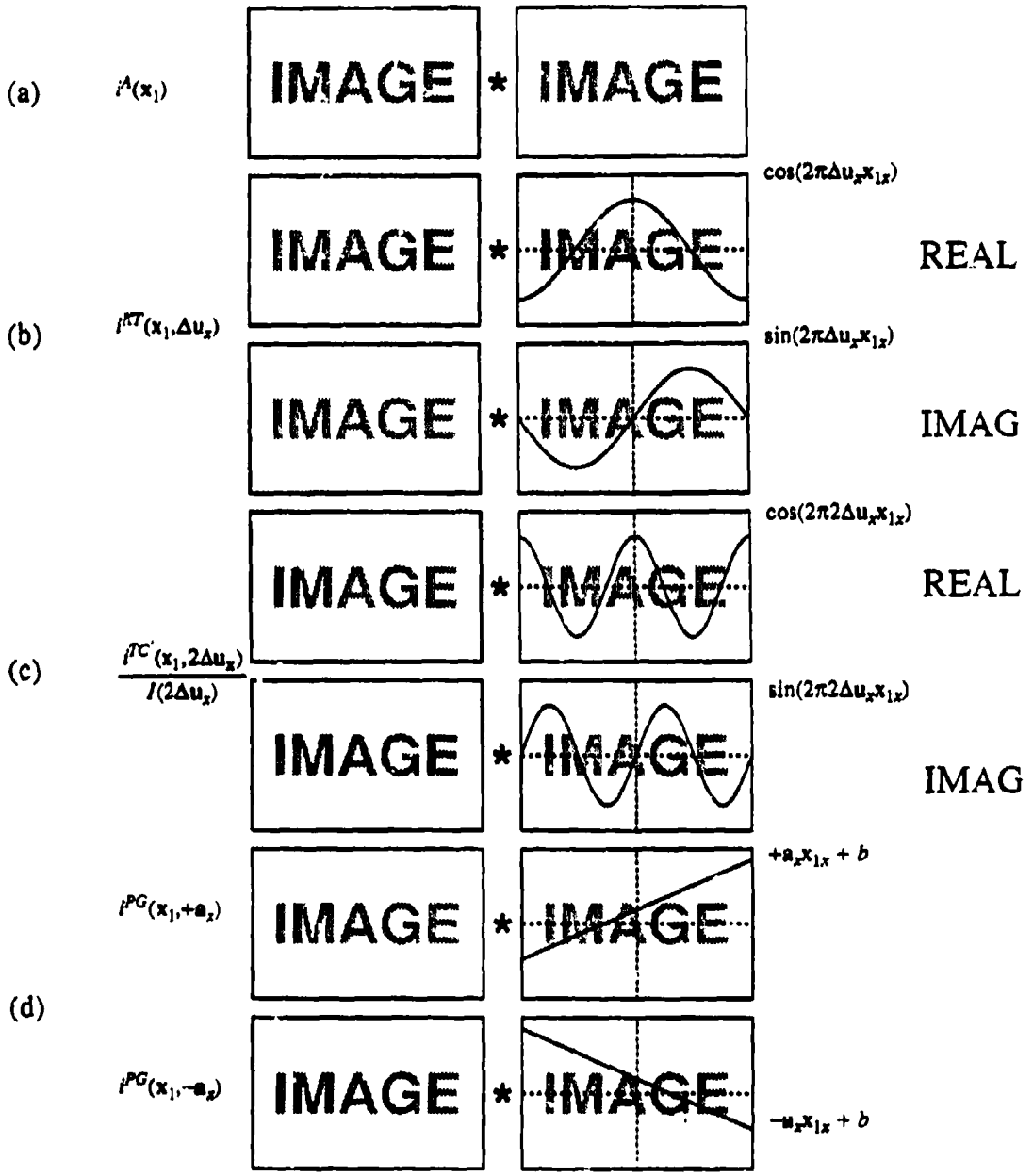
(a)
$I^A(x_1)$
IMAGE * IMAGE
$\cos(2\pi\Delta u_x x_{1x})$
IMAGE * IMAGE
REAL
(b)
$I^{RT}(x_1,\Delta u_x)$
$\sin(2\pi\Delta u_x x_{1x})$
IMAGE * IMAGE
IMAGE
$\cos(2\pi 2\Delta u_x x_{1x})$
IMAGE * IMAGE
REAL
(c)
$\frac{I^{TC}(x_1,2\Delta u_x)}{I(2\Delta u_x)}$
$\sin(2\pi 2\Delta u_x x_{1x})$
IMAGE * IMAGE
IMAG
$I^{PG}(x_1,+a_x)$
$+a_x x_{1x} + b$
IMAGE * IMAGE
(d)
$I^{PG}(x_1,-a_x)$
IMAGE * IMAGE
$-a_x x_{1x} + b$

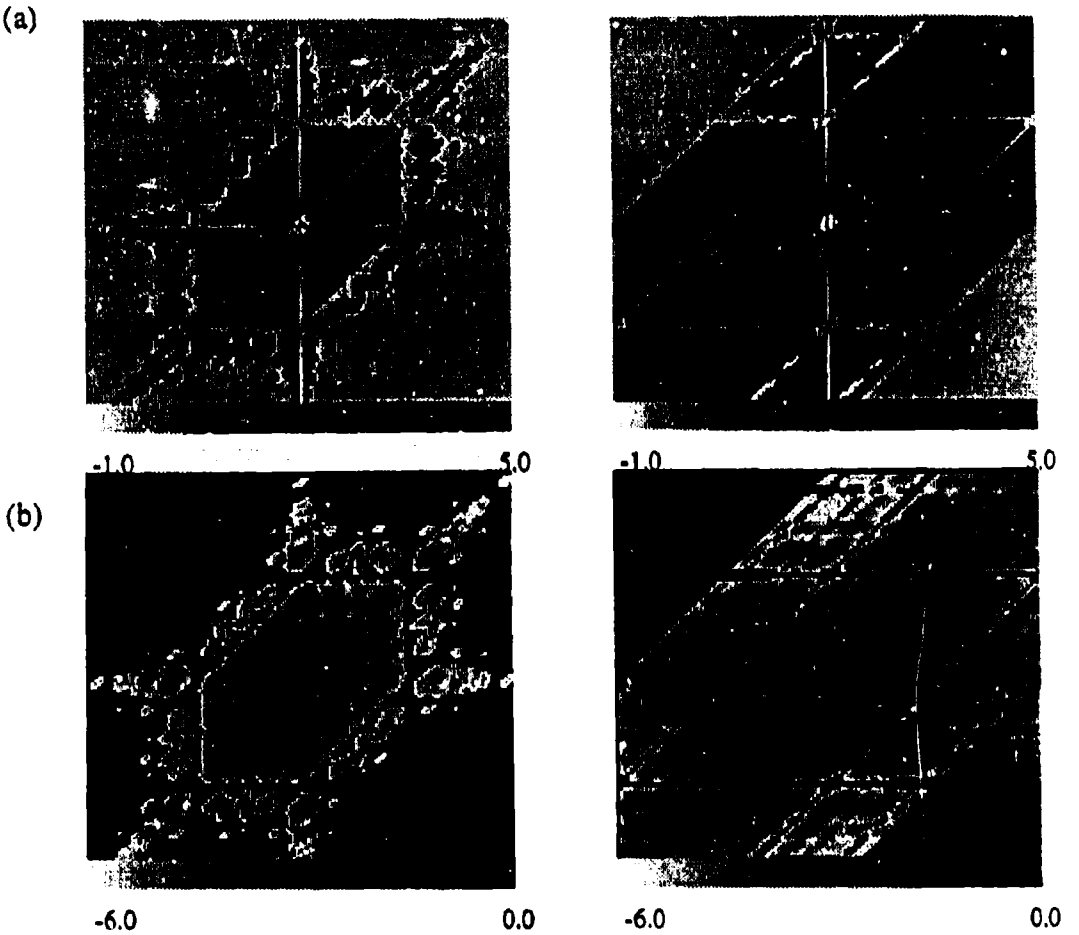
(a)
-1.0
5.0
-1.0
5.0
(b)
-6.0
0.0
-6.0
0.0
(c)
0.0
7.0
0.0
2000

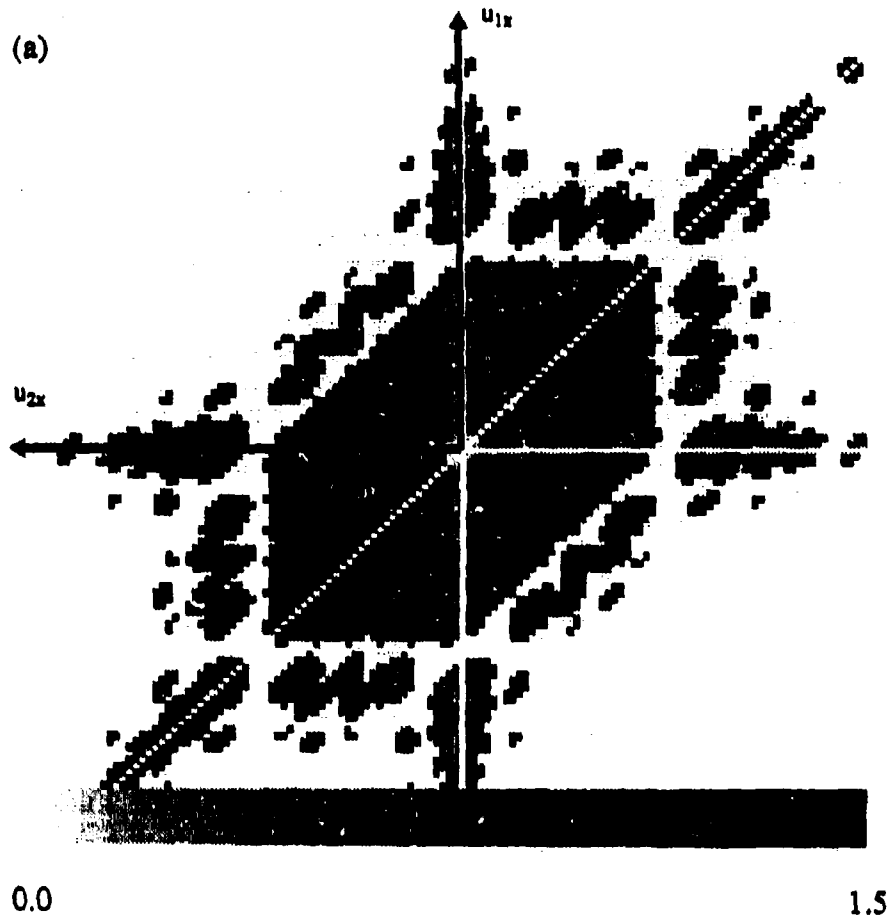
(a)
u_{1x}
u_{2x}
0.0
1.5

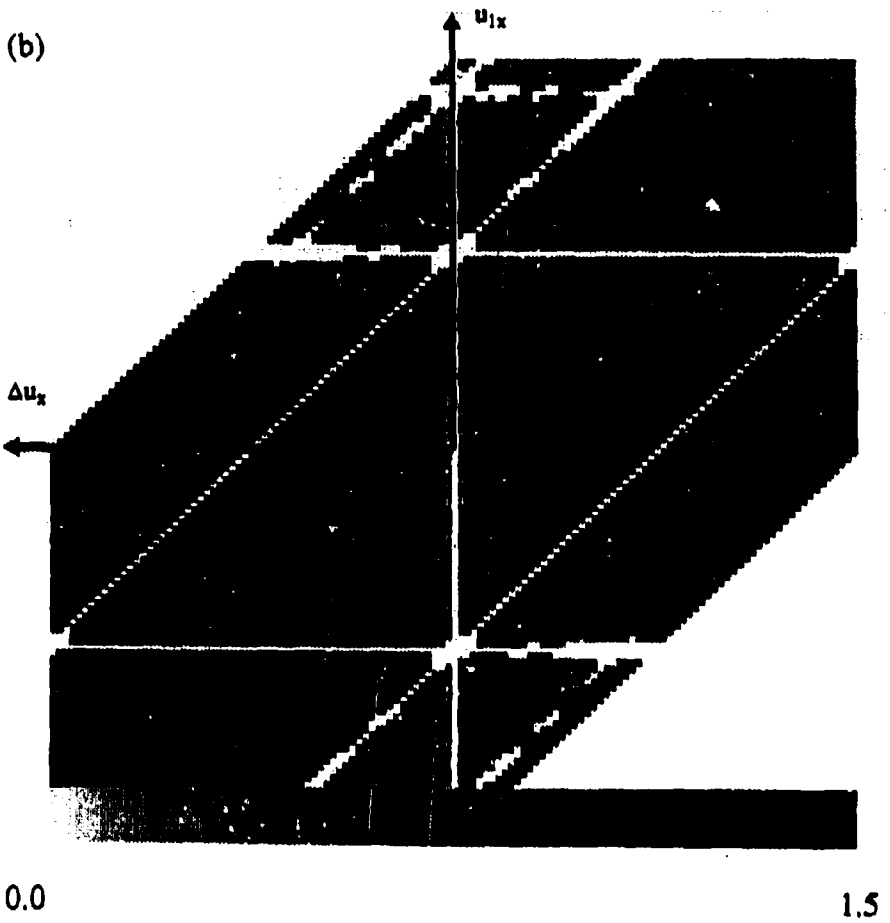
(b)
u_{1x}
Δu_x
0.0
1.5

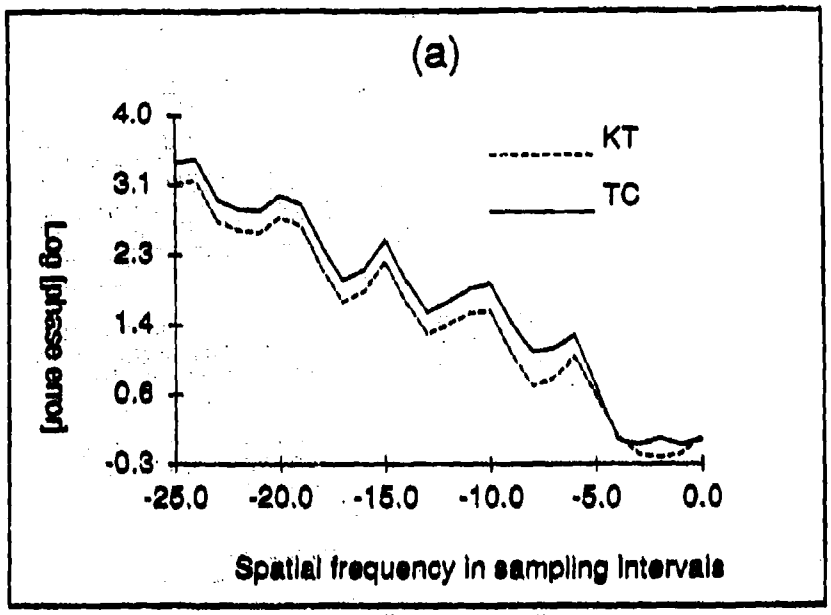
(a)
4.0
3.1
2.3
1.4
0.6
-0.3
KT
TC
Log [phase error]
-25.0
-20.0
-15.0
-10.0
-5.0
0.0
Spatial frequency in sampling intervals

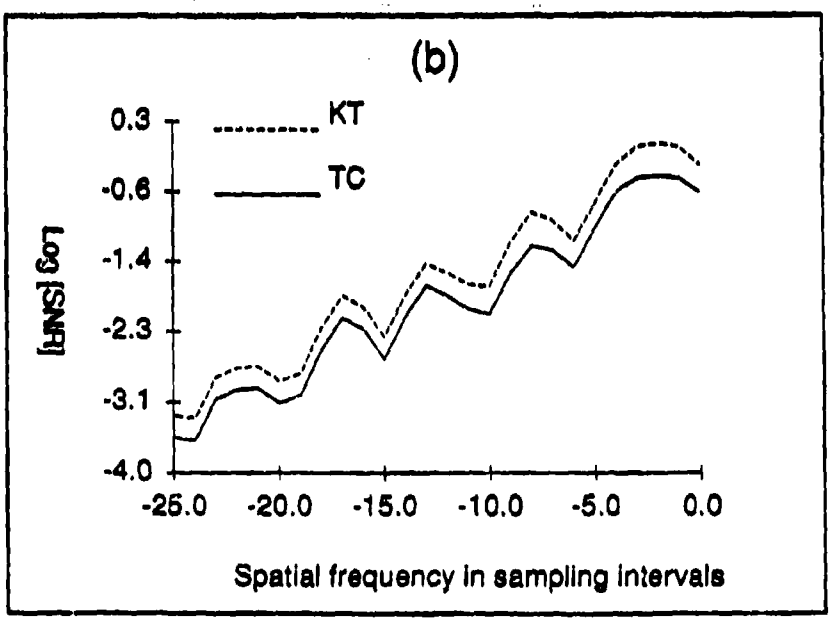
(b)
0.3
-0.6
-1.4
-2.3
-3.1
-4.0
KT
TC
Log [SNR]
-25.0
-20.0
-15.0
-10.0
-5.0
0.0
Spatial frequency in sampling intervals

A
B
C
D
u+Δu
Δu

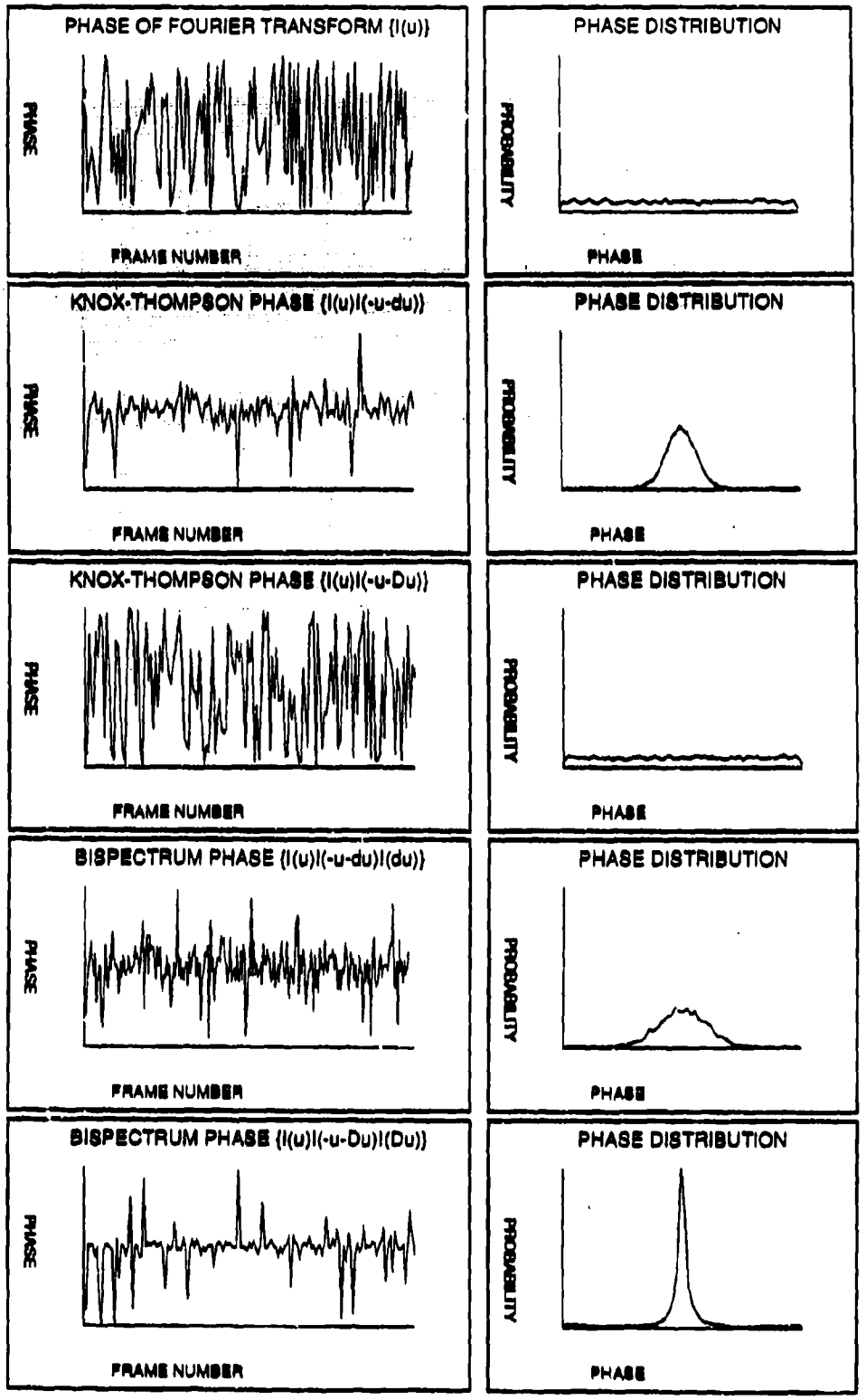
PHASE OF FOURIER TRANSFORM {I(u)}
PHASE
FRAME NUMBER
PHASE DISTRIBUTION
PROBABILITY
PHASE
KNOX-THOMPSON PHASE {I(u)I(-u-du)}
PHASE
FRAME NUMBER
PHASE DISTRIBUTION
PROBABILITY
PHASE
KNOX-THOMPSON PHASE {I(u)I(-u-Du)}
PHASE
FRAME NUMBER
PHASE DISTRIBUTION
PROBABILITY
PHASE
BISPECTRUM PHASE {I(u)I(-u-du)I(du)}
PHASE
FRAME NUMBER
PHASE DISTRIBUTION
PROBABILITY
PHASE
BISPECTRUM PHASE {I(u)I(-u-Du)I(Du)}
PHASE
FRAME NUMBER
PHASE DISTRIBUTION
PROBABILITY
PHASE

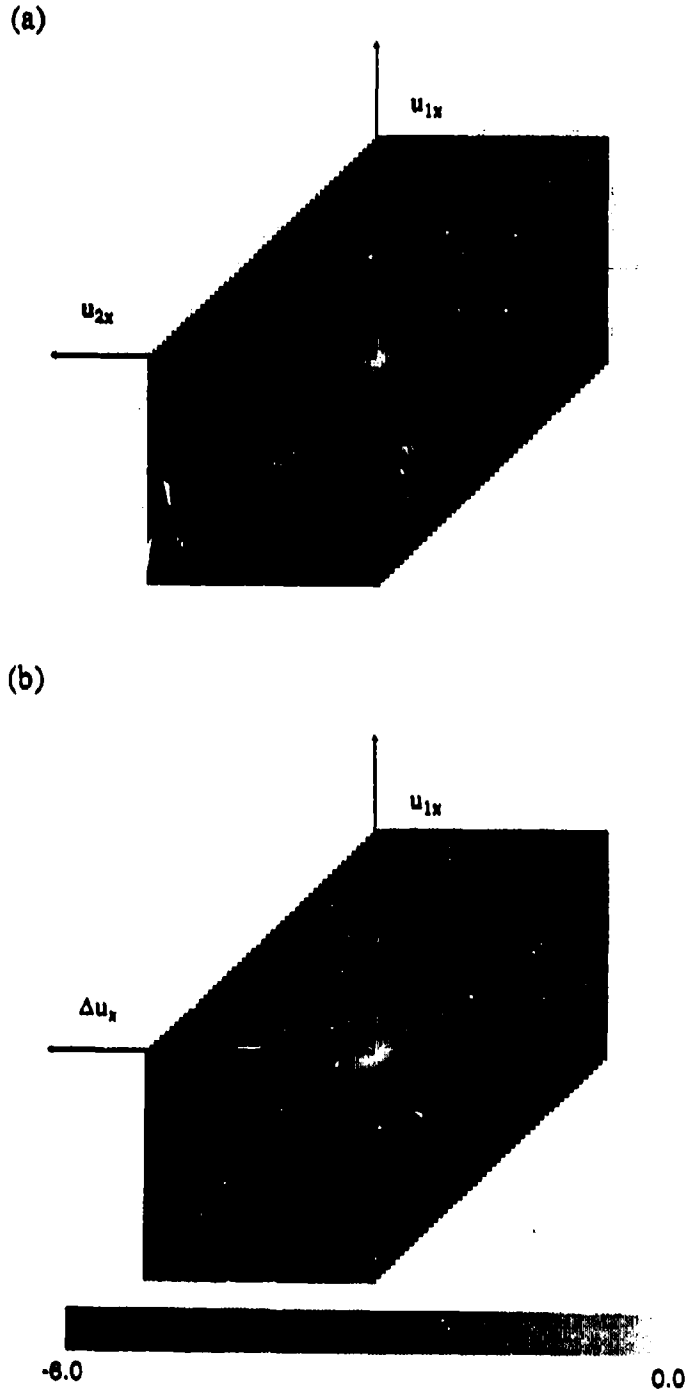
(a)
u_{1x}
u_{2x}
(b)
u_{1x}
Δu_x
-6.0
0.0

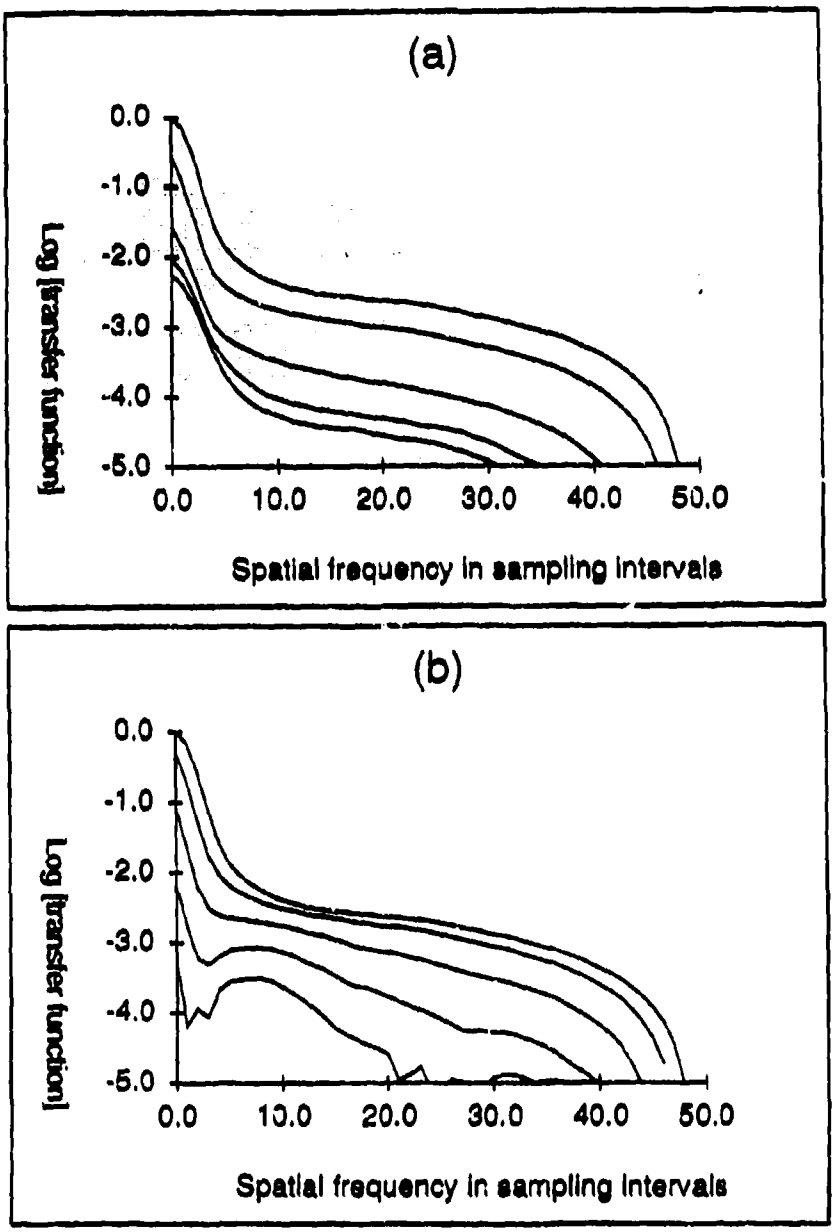
(a)
0.0
-1.0
-2.0
-3.0
-4.0
-5.0
Log [transfer function]
0.0
10.0
20.0
30.0
40.0
50.0
Spatial frequency in sampling intervals
(b)
0.0
-1.0
-2.0
-3.0
-4.0
-5.0
Log [transfer function]
0.0
10.0
20.0
30.0
40.0
50.0
Spatial frequency in sampling intervals

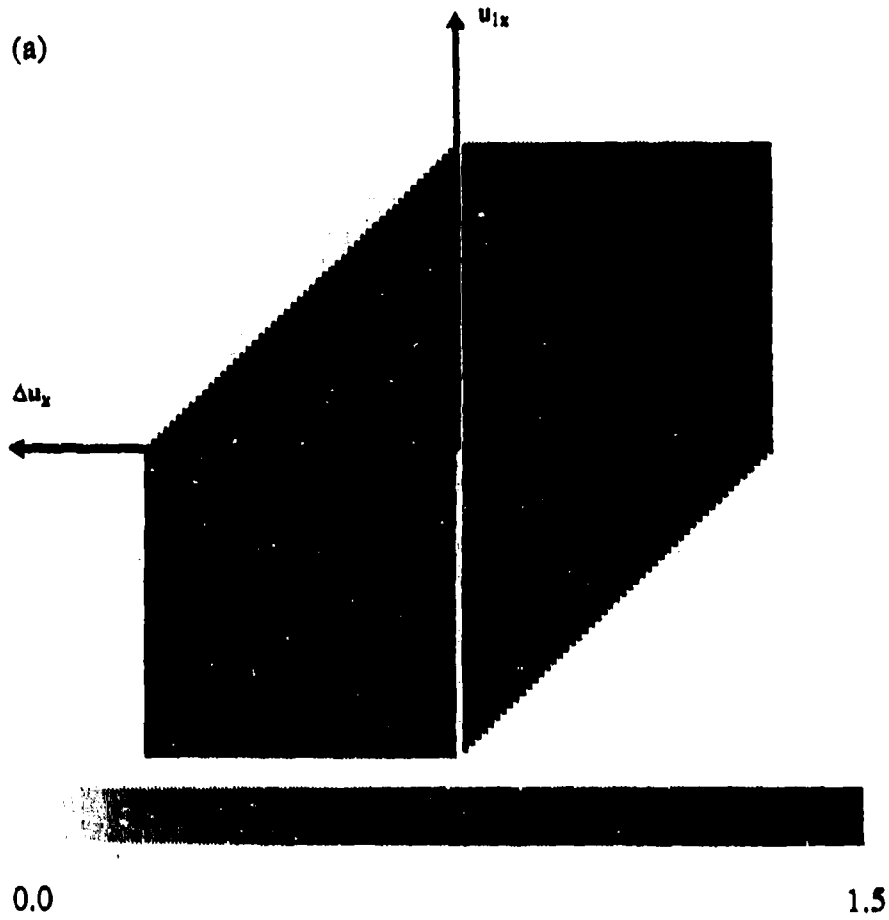
(a)
u_{1x}
Δu_x
0.0
1.5

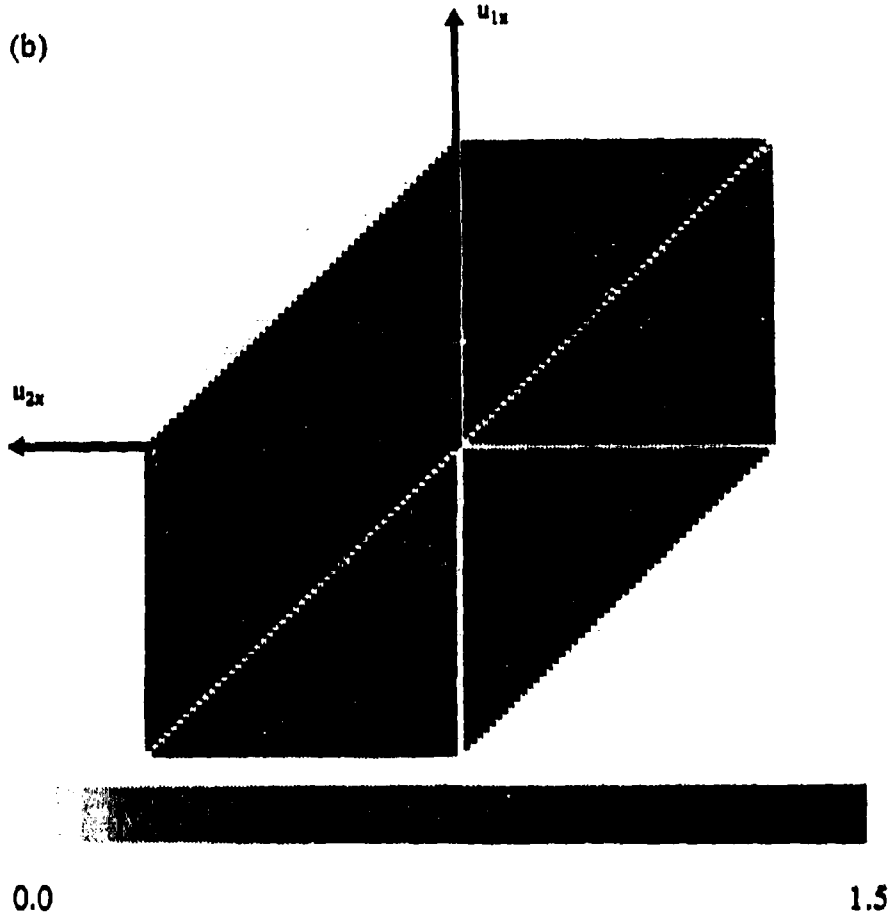
(b)
u_{1x}
u_{2x}
0.0
1.5

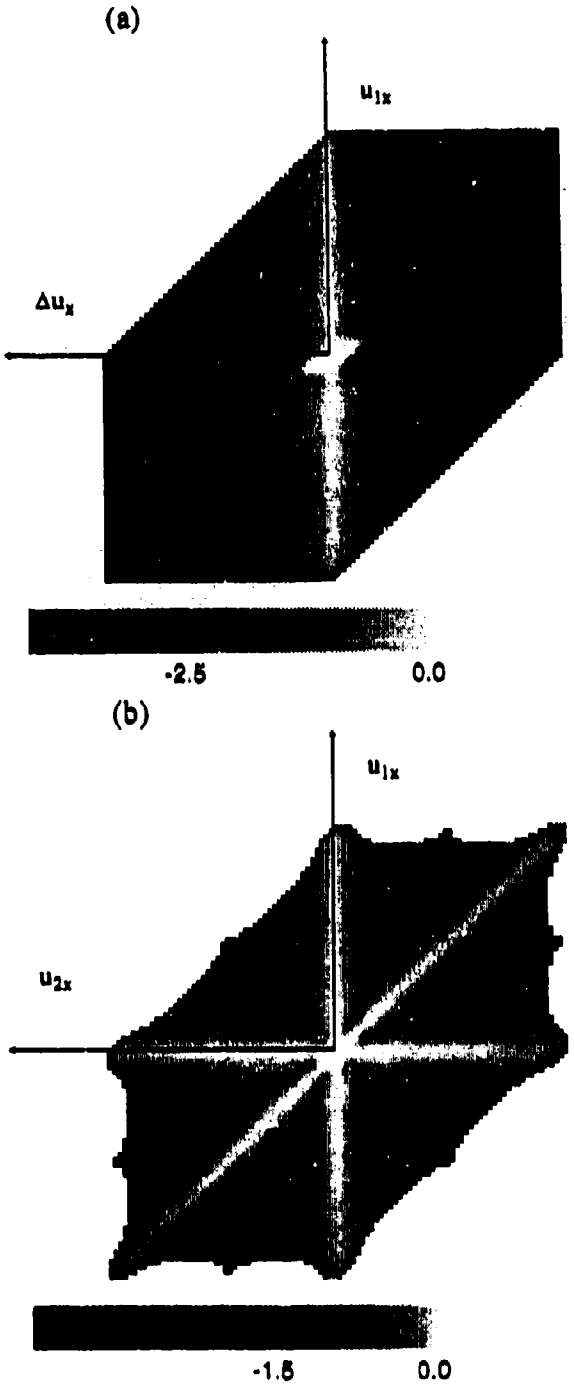
(a)
u_{1x}
Δu_x
-2.5
0.0
(b)
u_{1x}
u_{2x}
-1.5
0.0

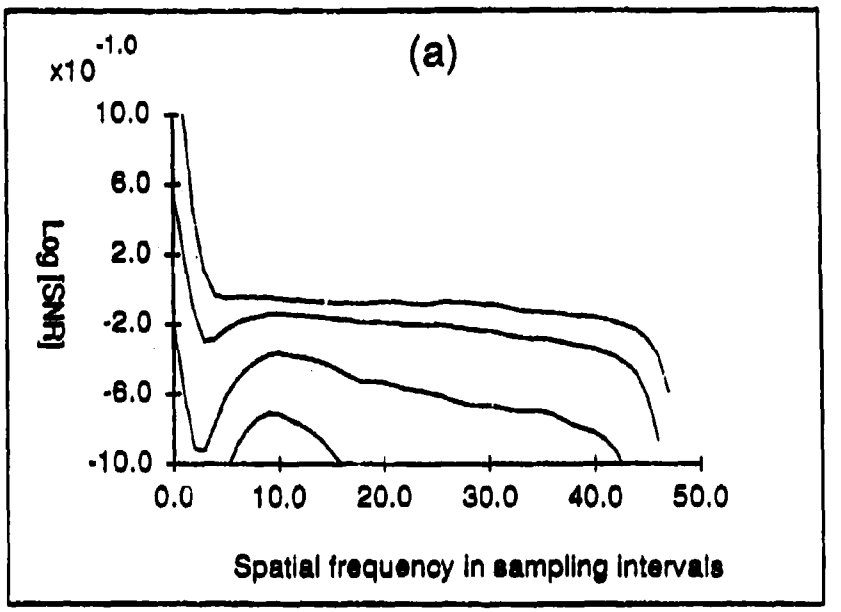
(a)
x10^-1.0
10.0
6.0
2.0
-2.0
-6.0
-10.0
Log [SNR]
0.0
10.0
20.0
30.0
40.0
50.0
Spatial frequency in sampling intervals

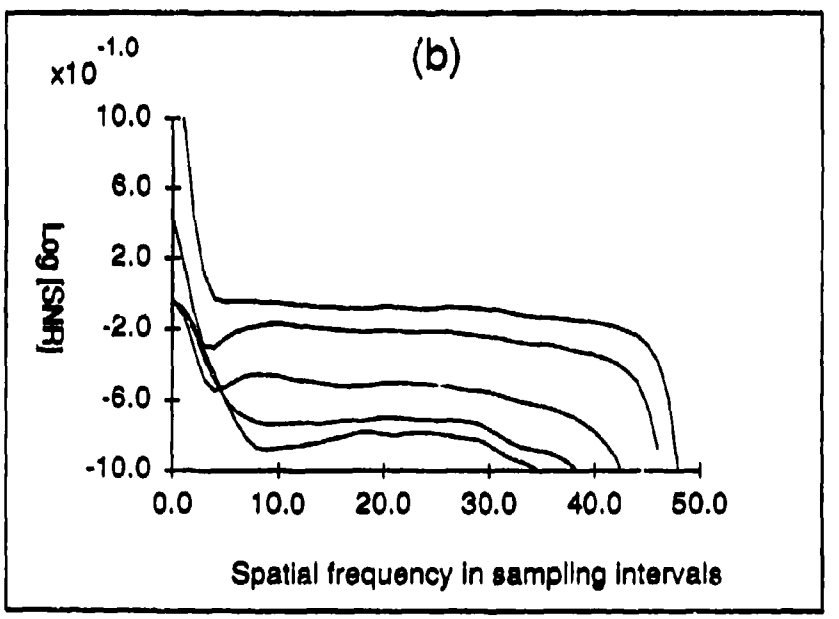
(b)
x10^-1.0
10.0
6.0
2.0
-2.0
-6.0
-10.0
Log [SNR]
0.0
10.0
20.0
30.0
40.0
50.0
Spatial frequency in sampling intervals

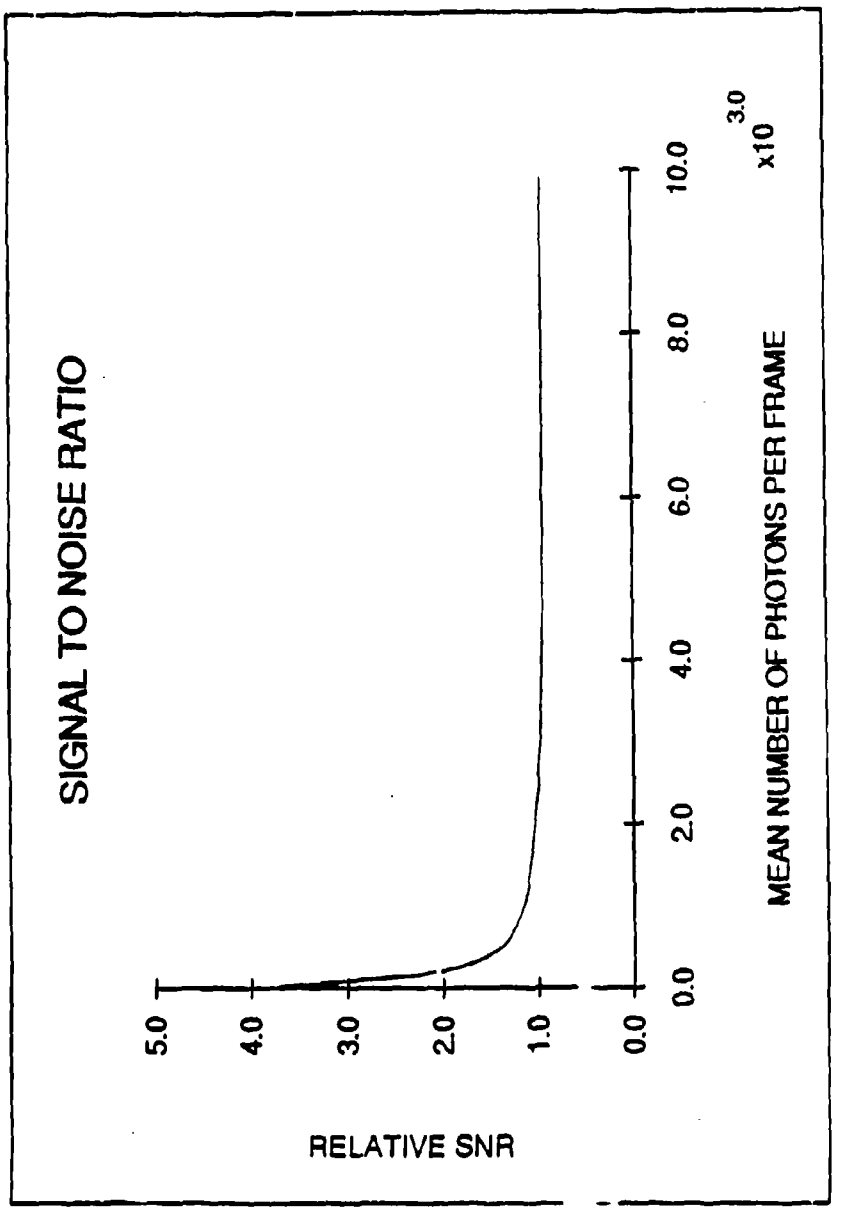
SIGNAL TO NOISE RATIO
RELATIVE SNR
5.0
4.0
3.0
2.0
1.0
0.0
0.0
2.0
4.0
6.0
8.0
10.0
MEAN NUMBER OF PHOTONS PER FRAME
x10^3.0

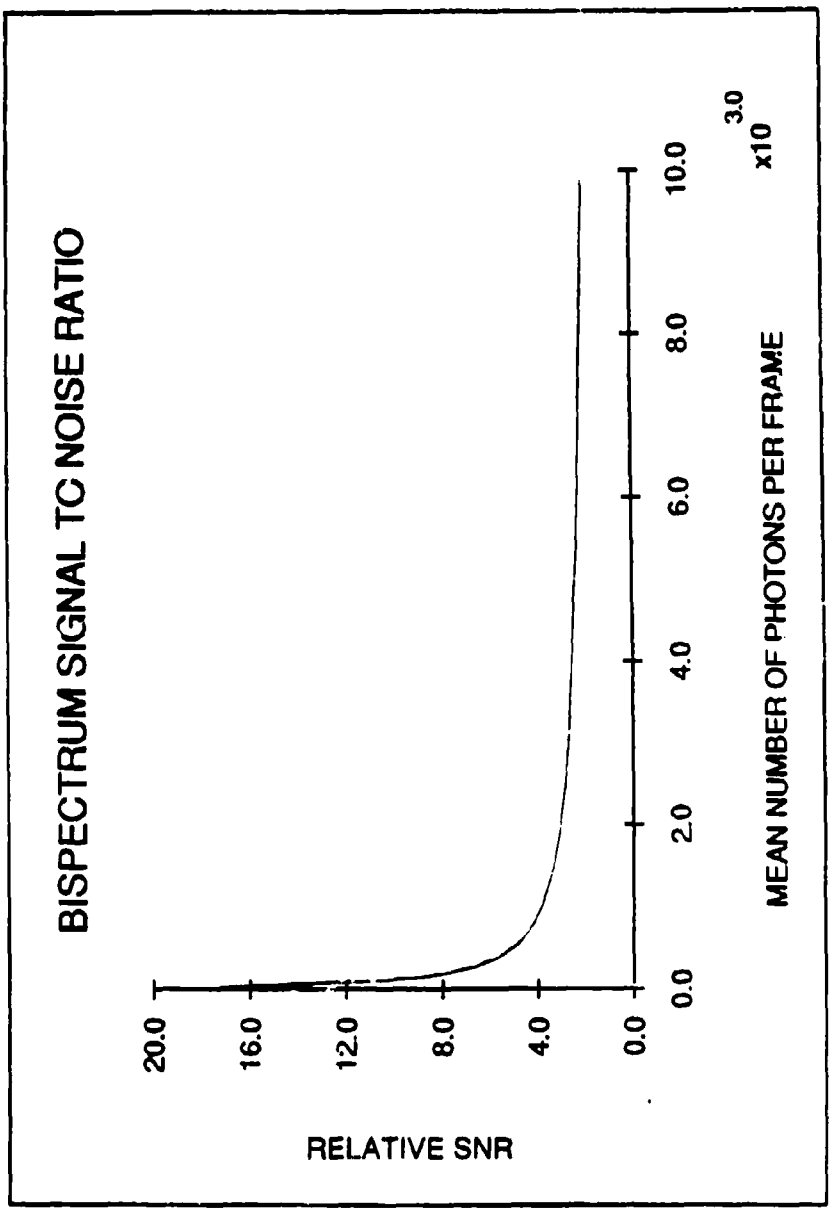
BISPECTRUM SIGNAL TC NOISE RATIO
RELATIVE SNR
20.0
16.0
12.0
8.0
4.0
0.0
0.0
2.0
4.0
6.0
8.0
10.0
3.0
x10
MEAN NUMBER OF PHOTONS PER FRAME

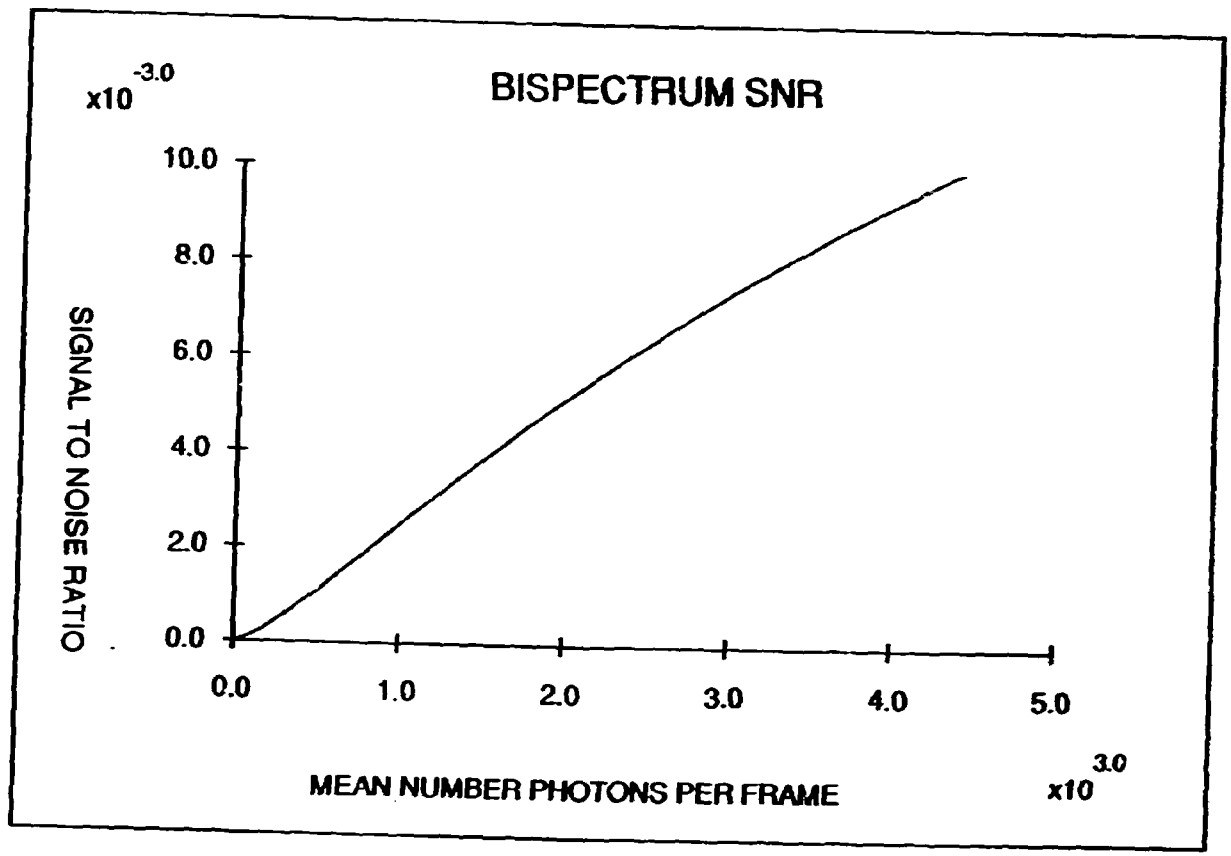
BISPECTRUM SNR
x10 -3.0
10.0
8.0
6.0
4.0
2.0
0.0
SIGNAL TO NOISE RATIO
0.0
1.0
2.0
3.0
4.0
5.0
MEAN NUMBER PHOTONS PER FRAME
x10 3.0

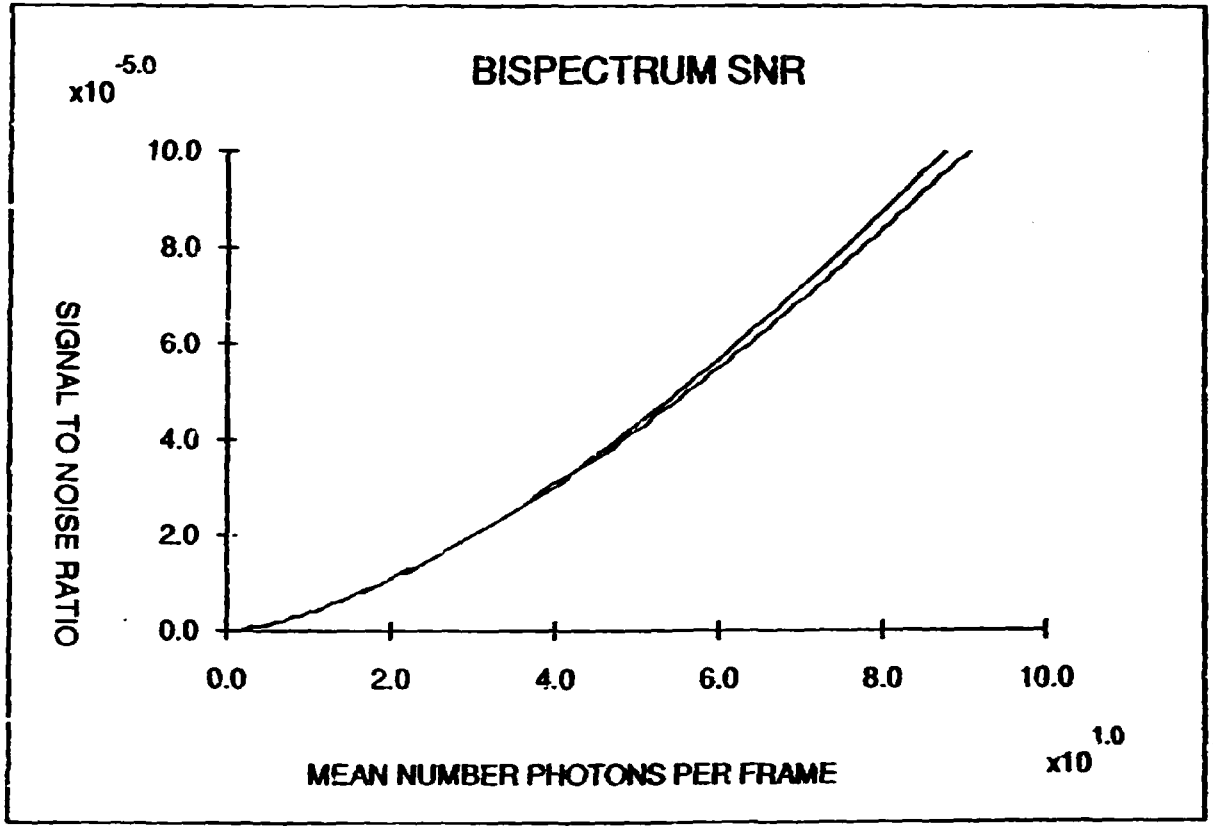
BISPECTRUM SNR
x10 -5.0
10.0
8.0
6.0
4.0
2.0
0.0
SIGNAL TO NOISE RATIO
0.0
2.0
4.0
6.0
8.0
10.0
x10 1.0
MEAN NUMBER PHOTONS PER FRAME

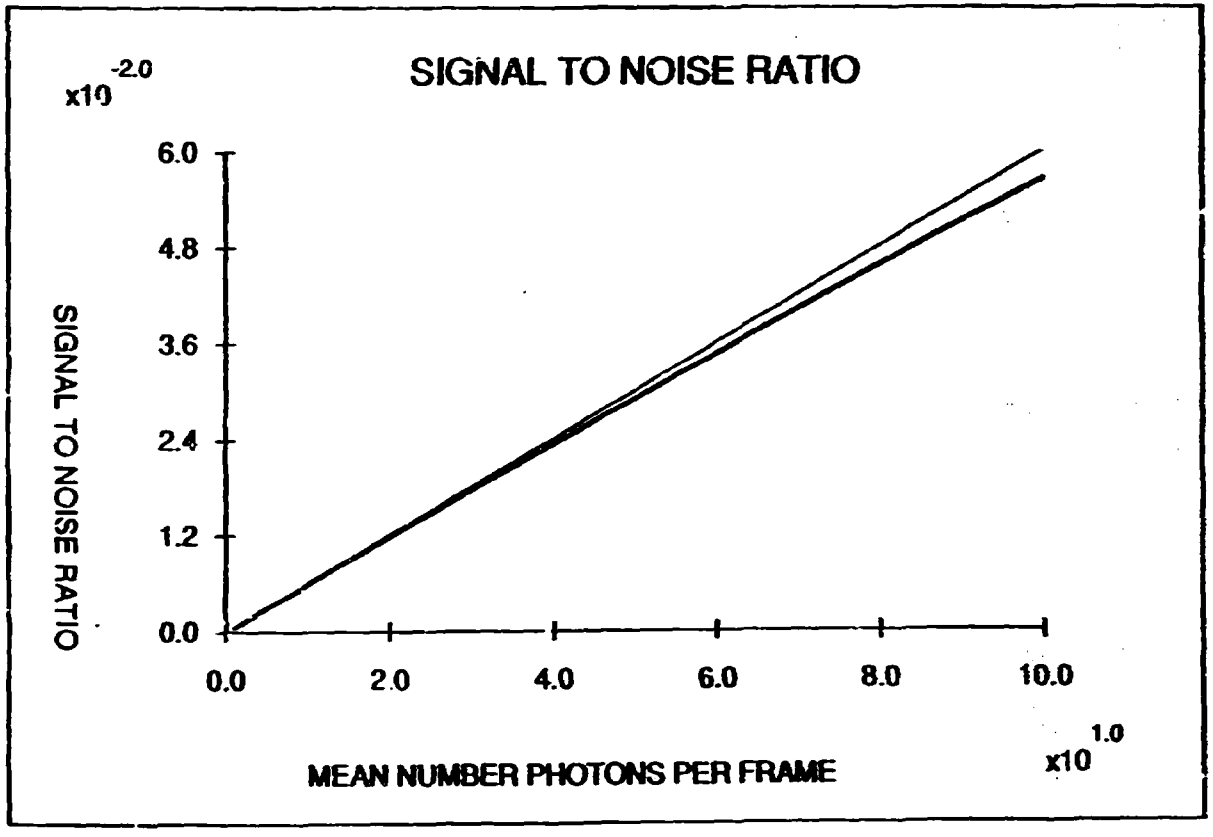
SIGNAL TO NOISE RATIO
x10 -2.0
6.0
4.8
3.6
2.4
1.2
0.0
SIGNAL TO NOISE RATIO
0.0
2.0
4.0
6.0
8.0
10.0
x10 1.0
MEAN NUMBER PHOTONS PER FRAME

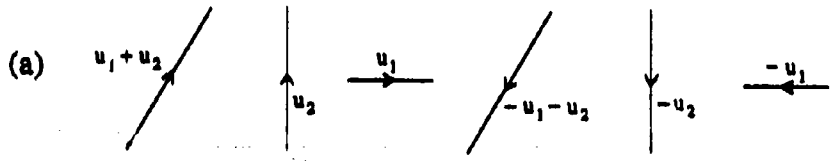
(a)
$u_1 + u_2$
u_2
u_1
$-u_1 - u_2$
$-u_2$
$-u_1$

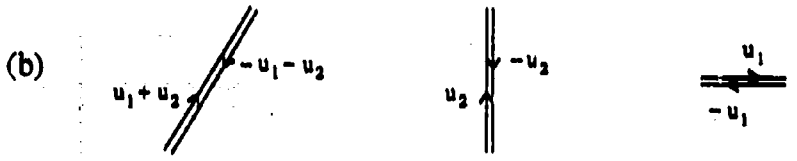
(b)
$u_1 + u_2$
$-u_1 - u_2$
u_2
$-u_2$
u_1
$-u_1$

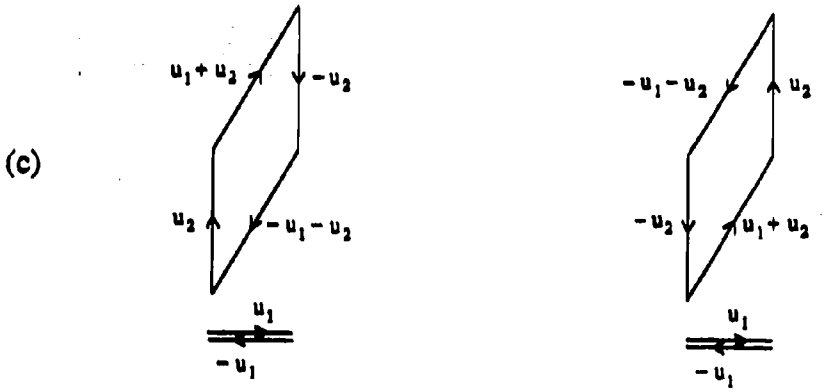
(c)
$u_1 + u_2$
$-u_2$
u_2
$-u_1 - u_2$
u_1
$-u_1$
$-u_1 - u_2$
u_2
$-u_2$
$u_1 + u_2$
u_1
$-u_1$

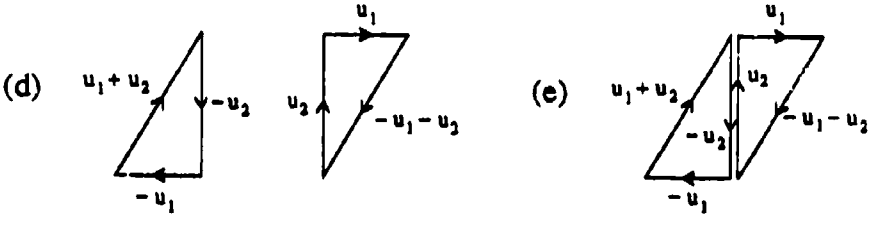
(d)
$u_1 + u_2$
$-u_2$
$-u_1$
u_1
u_2
$-u_1 - u_2$
(e)
u_1
$u_1 + u_2$
u_2
$-u_2$
$-u_1 - u_2$
$-u_1$

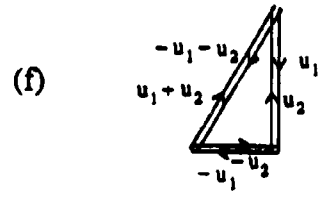
(f)
$-u_1 - u_2$
u_1
$u_1 + u_2$
u_2
$-u_2$
$-u_1$

REF 8

Algorithms for Image Reconstruction from Photon-Limited Data Using The Triple Correlation

M.J.Northcott, G.R.Ayers, J.C.Dainty.

Blackett Laboratory,
Imperial College, London SW7 2BZ.
UK.

ABSTRACT

The triple correlation technique of speckle imaging has been investigated in the low light level regime. Three practical methods for digital triple correlation processing have been developed. Each of these methods has successfully reconstructed images from computer simulated speckle interferograms. In this paper we describe and compare the three algorithms.

October 16, 1987

Algorithms for Image Reconstruction from Photon-Limited Data Using The Triple Correlation

M.J.Northcott, G.R.Ayers, J.C.Dainty.

Blackett Laboratory,
Imperial College, London SW7 2BZ.
UK.

1. Introduction.

The angular resolution of large ground based telescopes is severely limited by atmospheric turbulence. In order to overcome this limitation, some form of speckle interferometry technique may be used. These techniques rely on taking a series of measurements, with sufficiently short exposure times to freeze the effects of atmospheric turbulence. The resulting data is then processed to obtain the required diffraction limited information.

Using the traditional interferometry technique, as suggested by Labeyrie[1 2] we may obtain modulus information on the object of interest. However, with the advent of reasonably cheap digital computing, it is now becoming possible to use more complex methods such as the triple correlation[3 4 5] (in the following referred to as TC) and Knox-Thompson[2 6] techniques. With these techniques we can obtain the phase as well as the modulus, and thus reconstruct an image of the object.

2. Triple correlation processing

The triple correlation $I^{(3)}(x_1,x_2)$ and its Fourier transform, the bispectrum $I^{(3)}(u,v)$ are defined as follows:

$$I^{(3)}(x_1,x_2) = \int_{-\infty}^{\infty} i^*(x)i(x+x_1)i(x+x_2)dx \; . \tag{1}$$

$$I^{(3)}(u,v) = I(u)I(v)I^*(u+v) \; . \tag{2}$$

where $i(x)$ represents the signal and $I(u)$ its Fourier transform.

The basic methodologies of TC and autocorrelation processing are very similar. In both cases we sum the correlation functions of each frame over the complete data set. From Eq. (1) it is apparent that the TC of a two dimensional signal is a four dimensional function which leads to difficulties in computation and manipulation of the triple correlation. In practice we therefore process only a small sub-set of the TC or bispectrum.

In the following we will address specifically the case of photon limited interferograms, in particular the regime of less than one photon, on average, per speckle. In this regime data is most conveniently represented as a series of time tagged photon coordinates. Each photo-event is thus represented by a delta function in x,y,t space, ie

$$\delta(\mathbf{x}-\mathbf{x}_k)\delta(t-t_k)\,.$$

Integrating over a small time interval we obtain a time frame containing, say, N photons which is represented as[7] :

$$I(\mathbf{x}) = \sum_{k=1}^{k=N} \delta(\mathbf{x}-\mathbf{x}_k)\,, \tag{3}$$

Its Fourier transform is,

$$I(\mathbf{u}) = \sum_{k=0}^{k=N} \delta(\mathbf{x}-\mathbf{x}_k)\, e^{-2\pi i \mathbf{u}\mathbf{x}_k}\,, \tag{4}$$

where the product $\mathbf{u}\mathbf{x}_k$ represents the dot product of the two vectors, ($\mathbf{u}\cdot\mathbf{x}_k$). In Eqs. (3) and (4) $\mathbf{x}_k$ is the location of the k^{th} photo-event.

Most current imaging photon counting detectors are "time framed devices" in which typically the light signal is pre-amplified by an image intensifier, then integrated for a "time frame" of several tens of milliseconds on a film or C.C.D. Due to the limited frame rate achievable by such detectors, temporal resolution is is relatively poor. To gain maximum SNR (signal to noise) the frame rate must be adjusted, at recording time, to a rate dependent upon the coherence time of the atmospheric turbulence.

Future generations of imaging photon counters , for example the IPD [8] and PAPA [9 10] detectors, will be of the time tagging type. With these devices, individual photo-events are recorded with a temporal resolution typically of the order of a few micro-seconds. This gain in temporal resolution allows us to make better use of the limited number of photo-events from a faint source. For instance, the processing frame rate could be dynamically varied when processing the data, in an attempt to obtain the optimum trade-off between speckle contrast and signal intensity.

Probably the most important advantage of using time framed data, is that instead of dividing the data stream into time frames, we can look at it through a moving time window. One finds that when using the photon differencing algorithm in a moving time window, it is possible to compute 3 times as many differences or bivectors, than is possible when the data is processed in frames, see Appendix and Fig. 1. The SNR of the bispectrum along its axes, at the low photon levels of interest, scales roughly as $\bar{N}$, the mean number of photons per frame [15]. Equivalently we could say that the SNR scales as $\bar{N}_b^{1/3}$ where $\bar{N}_b$ is the mean number of bivectors calculable, per frame. Thus increasing the number of bivectors calculated from a data-stream by a factor of three, will increase the SNR by the order of $3^{1/3}$ or 1.44.

2.1 Reconstruction from the bispectrum.

The reconstruction algorithms used in the following sections are based on a recursive technique [11 12] . The phase of the bispectrum representation given in Eq. (2) is:

$$\beta^{(3)}(u,v) = \beta(u) + \beta(v) - \beta(u+v), \tag{5}$$

where $\beta^{(3)}(...)$ is the phase of the bispectrum and $\beta(...)$ the phase of the signal transform.

In the case of a one dimensional signal if we put $v = 1$ we get the following equations:

$$\text{for } u=1 \quad \beta(2) = \beta(1) + \beta(1) - \beta^{(3)}(1,1) . \tag{6}$$

$$\text{for } u=2 \quad \beta(3) = \beta(1) + \beta(2) - \beta^{(3)}(1,2) . \tag{7}$$

$$\text{for } u=3 \quad \beta(4) = \beta(1) + \beta(3) - \beta^{(3)}(1,3) . \tag{8}$$

.....

$$\text{for } u=n \quad \beta(n+1) = \beta(1) + \beta(n) - \beta^{(3)}(1,n) . \tag{9}$$

We are free to choose the first two phase values, since the phase at zero frequency is irrelevant, and the first frequency phase merely determines the position of the object. Arbitrarily setting the phase at the first frequency $\beta(1)$ to zero, we are thus able to compute the phase at $\beta(2)$, using Eq. (6) . Similarly Eqs. (7) to (9) allow us to compute all remaining phase values. This reconstruction technique leaves much scope for improvement, since due to its recursive nature it is fairly sensitive to noise. Unfortunately a least squares solution [13] suffers from the fact that the bispectrum phase is determined only modulo 2π . When noise is present this can lead to 2π mismatches in

the multiple phase estimates for each frequency. We avoid this problem in the recursive algorithm by multiplying and dividing complex exponentials, rather than adding and subtracting phases.

3. Algorithms.

3.1 Direct calculation of the Bispectrum.

With this method we calculate directly, from the Fourier transforms of each frame, selected points in the bispectrum. To do this we make use of the triple product relationship represented by Eq. (2).

The processing steps are:

a: Using traditional speckle interferometry techniques, estimate the modulus of the object.

b: Decide which bispectrum values are to be calculated. For maximum flexibility the coordinates of the bispectrum points to be calculated are formed into a list.

c: Calculate the Fourier transform of each frame. From the Fourier transforms calculate the mean value of each of the listed bispectrum points, over the data set.

d: Correct the bispectrum for the effects of photon bias [14].

e: Using the list of bispectrum points as a guide, reconstruct an estimate of the object transform.

Since we are only calculating a limited subset of the total bispectrum, we obviously wish to select those parts with the maximum SNR. Even given a knowledge of the object spectrum, calculation of the bispectrum SNR, allowing for atmospheric and Poisson noise is difficult[15]. In general however we can say that given bispectrum terms of the following form:

$$I^{(3)}(u,\Delta v) = I(u)I(\Delta v)I^{*}(u+\Delta v) .$$

then terms for which Δv is less than Fried's coherence parameter r_0/λ , will have the highest SNR.

With photon limited data, due to poor signal to noise, we do not expect to be able to reconstruct the object transform right out to the diffraction limit of the telescope. In order to conserve computation resources, we estimate the likely frequency cut-off of the phase reconstruction, and compute bispectrum points only out to this limit. Fig 2 shows experimentally determined curves of cut-off frequency vs number of data frames, at various photon levels, for a 2m telescope with r_0/λ of approx 18 cm. These

were derived by attempting to reconstruct the phase of a point source, from simulated speckle data, using the direct bispectrum method. For more complex objects the curves can be used as a upper bound on the reconstruction cut-off frequency. By cut-off frequency we mean, the frequency the maximum frequency to which phase values can be calculated with reasonable accuracy, for example within $\pi/4$

3.2 The Radon Transform.

The central-slice or projection-slice theorem states that if we form a one dimensional projection of a two dimensional function, then the Fourier transform of that projection is a central-slice (ie passing through the origin) of the Fourier transform of the object. We can make use of this theorem to reduce the processing of a two dimensional function to the processing of a number of one dimensional functions. We find that with the relatively simple objects which we have studied, a fairly small number of projection angles (eg 36) is sufficient for a reasonable reconstruction.

The steps in processing are:-

a: Project the two dimensional data onto a number of one dimensional lines at various angles. This is done by rotating the coordinate system by an angle α using the rotation matrix:

$$\begin{bmatrix} \cos(\alpha) & +\sin(\alpha) \\ -\sin(\alpha) & \cos(\alpha) \end{bmatrix}$$

Ignoring the y coordinate effects the projection.

b: For each angle of projection, compute the average triple correlation or bispectrum over the data set. At this step we may use a photon differencing algorithm to compute the triple correlation (Fig. 2).

c: From the mean bispectrum at each angle, reconstruct the corresponding central slice of the object Fourier transform.

d: Combine the various central slices into an estimate of the object Fourier transform, thus arrive at an estimate for the object. If possible object domain constraints such as positivity, should be included in this step.

In practice the object modulus is computed separately using the standard speckle interferometry techniques. The various projection triple correlations can be computed numerically, possibly dividing the calculations among several machines. Alternatively since we are working with one dimensional functions a hybrid opto-electronic processor [16] could be used to compute the correlations.

It should be noted that when reconstructing from the bispectrum one is free to chose the values of the transform phase at the zeroth and first frequencies. To first order it is equivalent to being free to specify the phase gradient at the origin. Since the Fourier transform of the object is analytic, it follows that the phase gradient at any point must be independent of direction. Thus provided we make appropriate choices for the first two frequencies of each reconstruction (eg both zero), we can guarantee there will be no phase errors between the slices. In the image domain this is equivalent to making the centres of gravity of each projection coincident.

3.3 Sub plane calculation.

Both of the previous methods have integrated the bispectrum the series of data-frames. It is of course possible to integrate the TC directly. At low light levels this is most conveniently done by using a photon differencing algorithm.

To see how the photon differencing algorithm is formulated, substitute Eq. (3) representing a photon limited image into the triple correlation Eq. (1):

$$I^{(3)}(x_1,x_2) = \int_{-\infty}^{\infty} dx \sum_{k=0}^{k=N} \delta(x-x_k) \sum_{\substack{l=1 \\ l\neq k}}^{N} \delta(x+x_1-x_l) \sum_{\substack{m=1 \\ m\neq k \\ m\neq l}}^{N} \delta(x+x_2-x_m) \; . \tag{10}$$

The conditions $l\neq k$ and $m\neq k, m\neq l$ are necessary to eliminate the photon bias terms . The bias terms are described in detail by Wirnitzer [14].

The integrand is non zero iff:

$$x_k = x \; . \tag{11}$$

$$x_l = x+x_1 \quad \Longrightarrow \quad x_l = x_k+x_1 \; . \tag{12}$$

$$x_m = x+x_2 \quad \Longrightarrow \quad x_m = x_k+x_2 \; . \tag{13}$$

Using equations (12) and (13), equation (10) can be rewritten as follows.

$$I^{(3)}(x_1,x_2) = \sum_{k=0}^{k=N} \sum_{\substack{l=1 \\ l\neq k}}^{N} \sum_{\substack{m=1 \\ m\neq k \\ m\neq l}}^{N} \delta(x_1-(x_l-x_k)) \, \delta(x_2-(x_m-x_k)). \tag{14}$$

Equation (14) clearly represents a photon differencing process, see Fig 3 .

Unfortunately due to the very large size of the TC for any reasonably dimensioned image, it is not practical to implement the photon differencing TC as it stands. For instance a 128 square image would normally generate a 256×10^6 element TC, which would require about 1Gb of store, or 170Mb if we made full use of the symmetry of the TC.

Fortunately, at the cost of increasing the computational burden, (3 integer ops. → 8 floating point ops.) we can compute a single two dimensional sub-plane of the bispectrum, using a modified photon differencing technique. Essentially we do this by computing two dimensions, of the four dimensional Fourier transform, which transforms the TC to the bispectrum, for some constant Fourier vector V. As already pointed out, the regions closest to the axes of the bispectrum in general have the highest SNR. If we compute these high SNR. regions by the photon differencing sub-plane method, the algorithm turns out, to be similar to the photon differencing method of generating the Knox-Thompson transform [15].

Using Eq. (14) the bispectrum may be written as:

$$I^{(3)}(u,v) = \int_{-\infty}^{\infty}\int_{-\infty}^{\infty} dx_1 dx_2 \; e^{-2\pi i u x_1} e^{-2\pi i v x_2} \times \sum_{k=1}^{N}\sum_{l=1}^{N}\sum_{m=1}^{N} \delta(x_1-(x_l-x_k))\,\delta(x_2-(x_m-x_k)). \tag{15}$$

where to aid clarity, we have omitted the conditions that eliminate the photon bias.

If we now put v equal to a constant, say $v = V$, we may carry out the x_2 integration forthwith.

Since x_2 is non zero only at $x_2 = (x_m - x_k)$:-

$$I^{(3)}(u,V) = \int_{-\infty}^{\infty} dx_1 \, e^{-2\pi i u x_1} \left[\sum_{k=0}^{k=N}\sum_{l=0}^{l=N}\sum_{m=0}^{m=N} \delta(x_1-(x_l-x_k))\, e^{-2\pi i V (x_m-x_k)} \right]. \tag{16}$$

Separating out the summation over m :-

$$I^{(3)}(u,V) = \int_{-\infty}^{\infty} dx_1 e^{-2\pi i u x_1} \left[\sum_{m=0}^{m=N} e^{(-2\pi i V x_m)} \right] \left[\sum_{k=1}^{N}\sum_{l=1}^{N} \delta(x_1-(x_l-x_k))\, e^{(2\pi i V x_k)} \right] \tag{17}$$

Excluding the photon noise bias terms this becomes:

$$I^{(3)}(u,V) = \int_{-\infty}^{\infty} dx_1 e^{-2\pi i u x_1} \left[\sum_{m=1}^{N} (1-\delta_{mk})(1-\delta_{ml}) e^{(-2\pi i V x_m)} \right] \times \left[\sum_{k=1}^{N} \sum_{l=1}^{N} \delta(x_1-(x_l-x_k)) - (1-\delta_{kl}) e^{(2\pi i V x_k)} \right], \quad (18)$$

where δ_{kl} is the kronecker delta.

The quantity inside the second set of large brackets can be calculated using a photon differencing technique, where each vector is given a complex weighting $e^{i(V x_k)} \sum e^{-i(V x_m)}$. After finding the mean value of this quantity over the data set, the integration over x_1 (Fourier transform) is carried out, yielding the bispectrum subplane $I^{(3)}(u,V)$.

We could of course put u and v equal to a constant, this would generate a single bispectum value. It is however more efficient to generate a whole plane at a time, thus replacing two complex multiplications per bivector per point with a final Fourier transform after the averaging is complete.

For a two dimensional signal the minimum requirement for reconstructing an image is to have calculated the two bispectrum subplanes V = (0,1) and V = (1,0) . In this minimal configuration the method is very closely related to the Knox-Thompson method.

4. Results.

Examples of an object reconstructed by all three techniques are shown in Figs 4 to 7. Each of the reconstructions represents roughly the same amount of computing time, taking about 12 seconds per data frame on a Sun 3/160 workstation (Motorola 68020 + 68881 at 16.7 MHz, C language). The direct method clearly produces the best reconstruction. However unlike the other two cases, the program implementing this method makes use of an array processor, which gives about a six fold increase in floating point speed. The relatively poor performance of the Radon transform, can probably be put down to insufficient numbers of slices, and a very poor recombination routine.

If one is fortunate enough to be using time-tagged data, then the method of choice would clearly be a photon differencing method. The reason being that this

method enables full use of the factor of 1.44 improvement in SNR, which comes as a result of time-tagging, as described in the Appendix.

With conventional time-framed data the direct method, which is applicable in both low and high light level regimes would seem to be most appropriate. However of all three algorithms the Radon transform method is the simplest to code, and needs minimal amounts of memory, it would probably be appropriate for a network of small computers. Furthermore it can be implemented as a series of photon differencing processes, and thus benefit from the time-tagging SNR improvement.

Acknowledgements

We are grateful to the UK Science and Enginering Council (GR/D 92332) and the US Army (DAJA45-85-C-0028) for financial support of this research.

References

[1] A. Labeyrie, "Attainment of diffraction-limited resolution in large telescopes by Fourier analysing speckle patterns in star images", Astron. Astrophys., 6 , 85-87 (1970) .

[2] J.C. Dainty in "Laser Speckle and Related Phenomena", ed. J.C. Dainty, Springer–Verlag 2nd edition (1984).

[3] A.W.Lohmann. G.Weigelt, B.Wirnitzer, "Speckle masking in astronomy: triple correlation theory and applications", Appl. Opt., 22 , 4028-4037 (1983) .

[4] G.Weigelt, B.Wirnitzer, "Image reconstruction by the speckle masking method", Opt. Lett., 8 , 389-391 (1983) .

[5] G.Weigelt, J.Ebersberger, " η Carinae resolved by speckle interferometry", JOSA., 68 , 673-683 (1980) .

[6] K.T. Knox, B.J. Thompson , " Recovery of images from atmospherically degraded short-exposure images", Astrophys., 193 , 45-48 (1974) .

[7] J.W.Goodman, J.Belsher, "Fundamental limitations in linear invariant restoration of atmospherically degraded images", Spie Proc., 75 , 141-154 (1976) .

[8] D.Rees, I.McWhirter, P.A.Rounce, F.E. Barlow, "Miniature imaging photon detectors II. Devices with transparent photocathodes", J. Phys. E: Sci. Instrum., 14 , 229-233 (1981).

[9] C.Papaliolios, L.Mertz, "New two-dimensional photon camera", Proc. SPIE, 331 , 360-364 (1982).

[10] C.Papaliolios, P.Nisenson, S.Ebstein, "Speckle imaging with the PAPA detector"' App. Opt., 24 , 287-290 (1985).

[11] H.Bartelt, A.W.Lohmann, and , B.Wirnitzer, "Phase and amplitude recovery from bispectra", Appl. Opt., 23 , 3121-3129 (1984).

[12] J.C.Dainty, M.J.Northcott, "Imaging a randomly translating object at low light levels using the triple correlation", Optics Commun., 58 11-14 (1986).

[13] T.Matsuoka, T.J.Ulrych, Proc. IEEE, "Phase Estimation Using The Bispectrum", 72 , 1403-1411 (1984).

[14] B.Wirnitzer, "Bispectral analysis at low light levels and astronomical speckle masking , JOSA, A/ 2 , 14-21 (1985).

[15] G.R.Ayers, M.J.Northcott, J.C.Dainty, "Knox-Thompson and triple correlation imaging through atmospheric turbulence", Submitted to JOSA A.

[16] A.A.Canas, "The acousto-optic triple product processor and its applications", Opt. & Quantum Elec. 19 , 79-82 (1987).

Appendix A.

In the following we show that the the SNR obtainable by calculating photon differencing correlations by integrating through a moving box-car window is significantly improved over that obtainable using a set of discrete time windows.

The photon differencing spatial auto-correlation algorithm specifies that we form a histogram of all the spatial vector co-ordinate differences between all permutations of two non-identical photons from a data frame. The analogous procedure for the triple correlation is to form a histogram of all spatial bi-vector (see Fig. 3) differences, between all permutations of three non-identical photons from a data-frame.

First let us consider a data-stream consisting of a set of events spaced regularly in time as shown in Fig. 8. The stream is divided up into adjacent time frames labelled (1-4) of length T, with N photons per frame.

If we have calculated the auto-correlation for frame 1, how many additional difference vectors does frame 2 contribute? Using the traditional time-frame approach there are N(N-1)/2 independent difference vectors. In the case of triple correlation there are N(N-1)(N-2)/6 independent bi-vectors and for k^{th} order correlation we get $\frac{N!}{(N-k)!\,k!}$ or ${}^{N}C_{k}$ independent $(k-1)^{th}$ order difference vectors.

Using a moving window approach we select each photon in frame 2 in turn and difference it with the photons in the preceding period of length T. In the case of the auto-correlation, we would get (N-1) independent difference vectors per additional photon, giving a total contribution of N(N-1) independent difference vectors from the frame. For triple correlation we get N(N-1)(N-2)/2 independent bi-vectors and in the case of a k^{th} order correlation we get $\frac{N!}{(N-k)!\,(k-1)!}$ independent $(k-1)^{th}$ order difference vectors. Thus for the auto-correlation we get twice as many difference vectors, for the triple correlation three timer as many bivectors, and for a k^{th} order correlation k times as many difference vectors.

Figure 9 illustrates a stream of photons obeying uniform (ie constant rate) Poisson statistics in time. For a frame containing N photons for a k^{th} ($k \leq N$) order correlation we get $\frac{N!}{(N-k)!\,k!}$ independent $(k-1)^{th}$ order difference vectors, as in the regularly spaced case above. Averaging this over uniform Poisson statistics gives a mean of $\frac{\bar{N}^{k}}{k!}$ independent difference vectors per frame, or $\frac{\bar{N}^{(k-1)}}{k!}$ per photon.

A basic property of a uniform Poisson process is that its statistics are independent of when we choose to start measuring the process. Thus if we measure the number of photons in a time window of length T, the distribution observed will be independent of the positions of the windows, provided they are uniformly distributed throughout time. In particular we may choose to observe the process through windows whose start time is itself a Poisson process.

Using the time window approach on a Poisson process, we move our window along the time axis until its leading edge is coincident with a photon. The resulting set of time frames will be Poisson distributed in time and as pointed out above this will not effect the observed photon statistics. Thus the expectation value of the number of photons in each frame, not including the photon on the leading edge is simply $\bar{N}$. With N photons in a particular frame, differencing the leading photon with the N photons $\frac{N!}{(N-k+1)!\,(k-1)!}$ difference vectors. When we average this quantity over a Poisson process we get $\frac{\bar{N}^{(k-1)}}{(k-1)!}$ difference vectors per observed photon. Thus comparing this to the mean number of independent difference vectors $\frac{\bar{N}^{(k-1)}}{k!}$ per photon given above, we get the same factor k increase in the number of difference vectors as we did with a regular event spacing.

The SNR in the power-spectrum at low photon levels scales as $\bar{N}$ and similarly the SNR of those portions of the bispectrum close to the axes (close to the power-spectrum terms), where the SNR is highest, also scale as $\bar{N}^{1/2}$. Assuming an analogous result holds for higher order spectra, the SNR of a k^{th} spectrum scales as $\bar{V}_k^{1/k}$, where $\bar{V}_k$ is the number of k^{th} order difference vectors per observed photon. Since when calculating a k^{th} order correlation using a continuous time window gives us k times more difference vectors, we can say that the SNR improvement in the k^{th} order spectrum is of the order of $k^{1/k}$. This improvement in SNR is $\sqrt{2}$ for the autocorrelation and $\sqrt[3]{3}$ for the triple correlation.

Figure 1:

Using a continuous time window of length T, we gain the correlation term between the photons C,D,E, which would not arrise when using a more conventional time framed data-stream.

Figure 2:

Cut-off frequency of TC reconstruction vs No. of frames for reconstruction of a point source using the direct method. The diameter of the telescope is 2m, equivalent to 50 bins. Frieds parameter is set to 18cm. The cut off is arbitrarily placed at the radius where the phase variance of the reconstruction becomes greater than /4. Telescope cut-off 50 bins.

Figure 3:

Above figure is a graphical representation of the formation of a bi-vector from three photo-event co-ordinates. One of the bivectors implied by eqn (15) is drawn, both of the componant vectors are shown as arrows between two photo-events. The vector corresponding to $\delta(x(x_l - x_k))$ is shown pointing from photon k to photon l, similarly for the vector corresponding to $\delta(x(x_m - x_k))$. These two vectors would be catenated to form a four vector corresponding to a triple correlation element.

Figure 4:

Diffraction limited object seen through a 2m telescope

Figure 5:

Reconstruction using direct method with 20000 frames at 200 photons per frame.

Figure 6:

Reconstruction using radon transform with 25000 frames at 200 photons per frame, projections every 4 degrees.

Figure 7:

Reconstruction using sub-plane method with 12500 frames at 200 photons per frame, 4 planes used

Figure 8:

A regular temporal process, divided into discrete time frames.

Figure 9:

A temporal Poisson process, divided into discrete time frames.

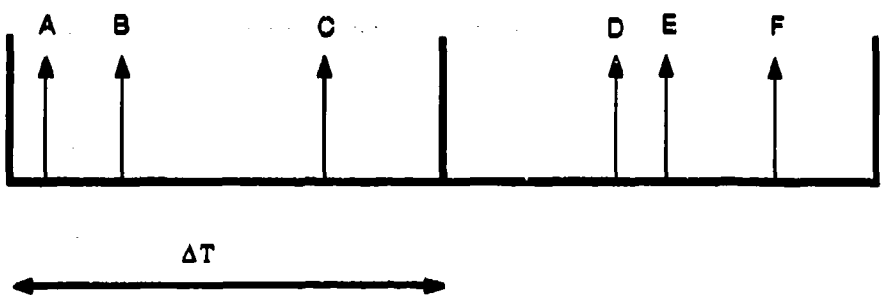

Fig. 1

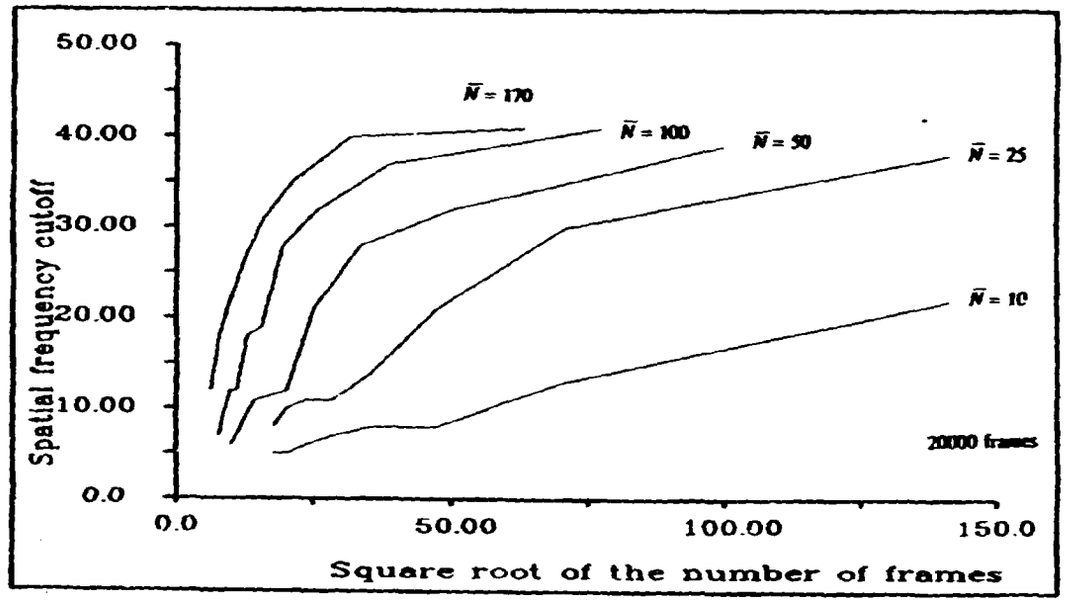
50.00
40.00
30.00
20.00
10.00
0.0
Spatial frequency cutoff
$\bar{N}$ = 170
$\bar{N}$ = 100
$\bar{N}$ = 50
$\bar{N}$ = 25
$\bar{N}$ = 10
20000 frames
0.0
50.00
100.00
150.0
Square root of the number of frames

FIG. 2

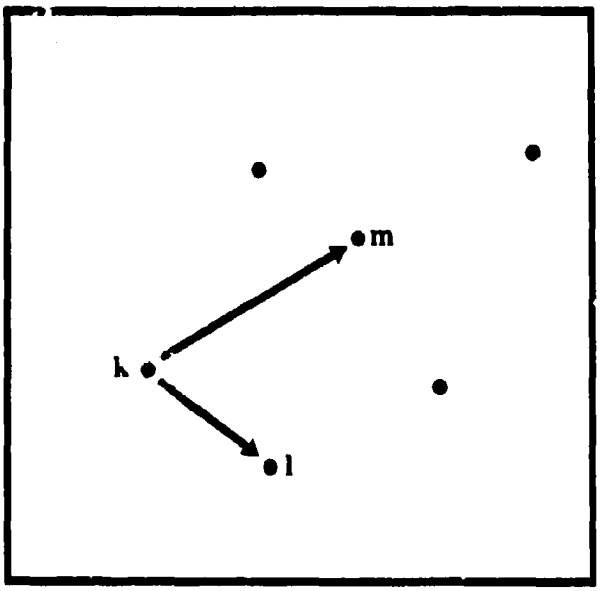
m
k
l

Diffraction limited object seen through a 2m telescope.

Object

Fourier Phase

Fig 4

Reconstruction using direct method.

20000 frames at 200 photons per frame.

Reconstructed Object

Reconstructed Phase

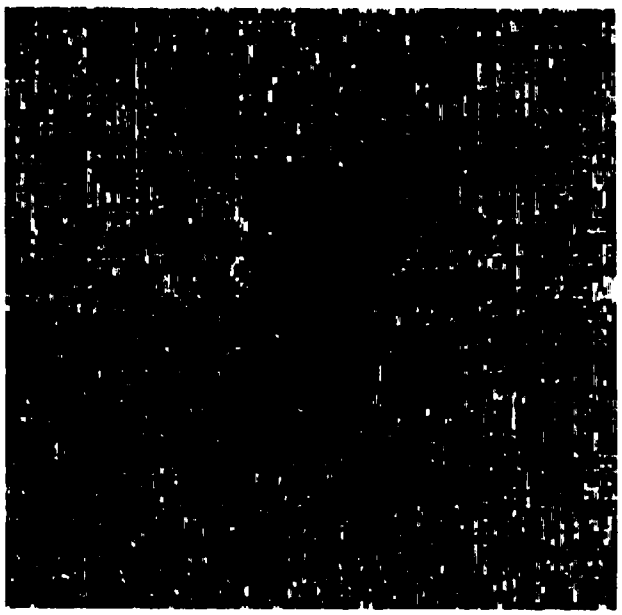

Fig 5

Reconstruction using the Radon method.

25000 frames at 200 photons per frame, Projections every 4 degrees.

Reconstructed Object

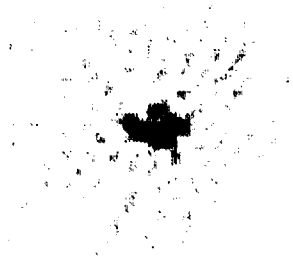

Reconstructed Phase

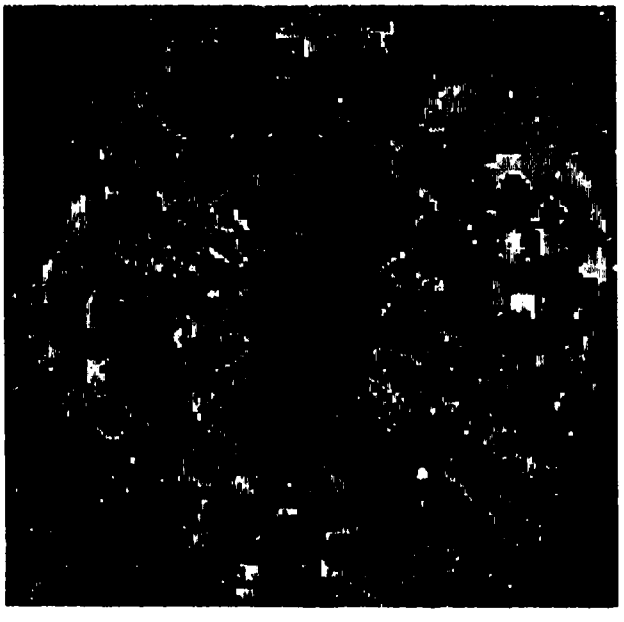

Fig 6

Reconstruction using the Sub-plane method.

12500 frames at 200 photons per frame, 4 planes used.

Reconstructed Object

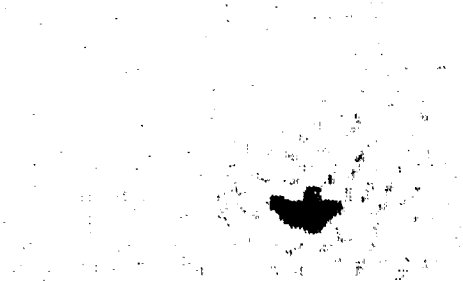

Reconstructed Phase

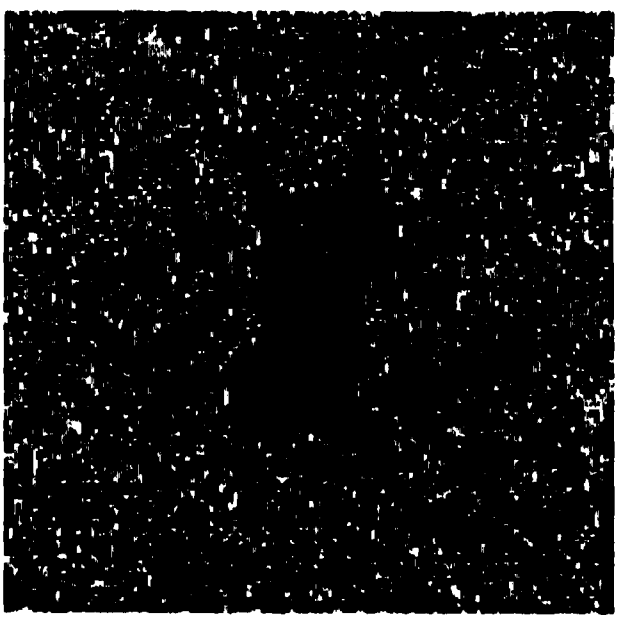

Fig 7

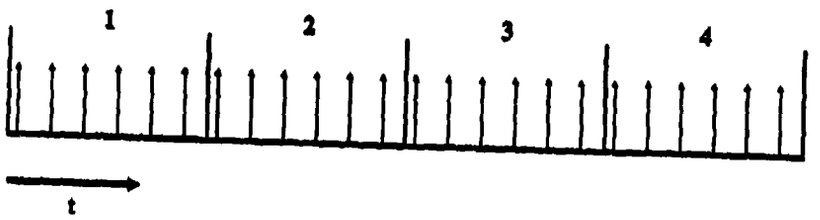

Fig. 8

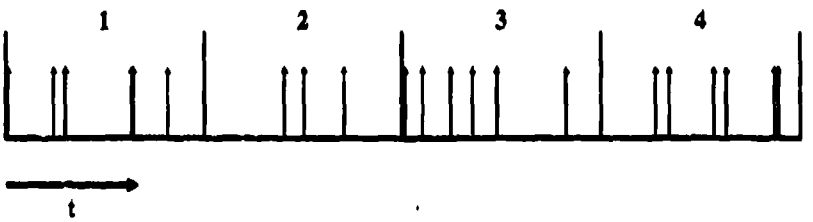

Fig. 9

REF 9

OBJECT RECONSTRUCTION FROM PHOTON-LIMITED CENTROIDED DATA OF RANDOMLY TRANSLATING IMAGES

L.C. de Freitas and J.C. Dainty

Blackett Laboratory
Imperial College - London SW7 2BZ - U.K.

ABSTRACT

Centroiding is investigated as a simple and computationally fast technique of object reconstruction, at low light level, from randomly translating images. A relationship between the spectrum of the average N-photon centroided frame and the object spectrum is presented as well as an algorithm for retrieving the phase in the case of one-dimensional objects. Computer simulated data is used to test the relationship and the reconstruction algorithm.

1 - INTRODUCTION

A number of techniques have been developed to retrieve diffraction-limited astronomical images by recording short-exposure frames of speckle patterns. The SHIFT-AND-ADD (SAA) method[1-5] is one of the proposed techniques. It relies on the proposition that each frame consists of many distorted replicas of the true image and that an improved estimate of the image can be found by superimposing these distorted replicas. At very low light level each of these distorted images may have only a few photons and no "bright" speckle can be chosen in order to implement the SAA technique.

Centroiding is investigated as a new way of circumventing this limitation and for this purpose a relationship between the N-photon averaged centroided images and the stationary normalized image $I(\mathbf{r})$ as well as a phase reconstruction algorithm is presented for the special case of randomly translating images of one-dimensional objects.

2 - THEORY OF CENTROIDING DATA OF RANDOMLY TRANSLATING IMAGES.

To "freeze" a randomly moving image, photons, that are all supposed to be emanated from the same randomly translating image, are detected during a series of short time intervals(frames). To retrieve the stationary image one should, for each frame k, shift the photon vectors by the amount that the true centroid of the image is displaced in respect to the centre of the frame and average(add) over all the frames. The true shift vector $\mathbf{c}_k$ is unknown and as an estimator, the centroid vector $\mathbf{R}_k = \frac{1}{N}\sum_{j=1}^{N}\mathbf{x}_j$ of the detected photons is evaluated and the photon vectors are shifted by this estimator before averaging many such frames.

The relationship between the centroided and the non-centroided spectrum of the N-photon data $d_k(\mathbf{x})$ detected on the k^{th} frame is:

$$\tilde{D}_k^c(\mathbf{u}, \mathbf{x}_1, ..., \mathbf{x}_N) = exp(+i2\pi\mathbf{u}\cdot\mathbf{R}_k)\,\hat{D}_k(\mathbf{u}, \mathbf{x}_1, ..., \mathbf{x}_N) \tag{1}$$

and the average of $\tilde{D}_k^c(\mathbf{u}, \mathbf{x}_1, ..., \mathbf{x}_N)$ over all possible sets of detected N-photon coordinates is performed using the normalized object intensity as the probability density distribution. Thus Eq.(1) leads to a quantity $\tilde{Q}_N(\mathbf{u}) \equiv D^c(\mathbf{u})/N$ related to the normalized object intensity spectrum[6]:

$$\tilde{Q}_N(\mathbf{u}) = \tilde{I}(\mathbf{u}[1 - 1/N]) \quad \left[\tilde{I}(-\mathbf{u}/N)\right]^{N-1} \tag{2}$$

Expression (2) is a translation invariant relationship between the normalized spectrum of the stationary image $\tilde{I}(\mathbf{u})$ and the spectrum $\tilde{Q}_N(\mathbf{u})$ of the centroided average of those frames containing exactly N photons per frame. For instance for $N = 2$ Eq.(2) reduces to

$\tilde{Q}_2(u) = \left|\tilde{I}(\frac{u}{2})\right|^2$ which is the power spectrum of $\hat{I}(u)$ where the variable u is scaled by a factor of 2.

For N=3

$$\tilde{Q}_3(u) = \tilde{I}(\frac{2}{3}u) \quad \tilde{I}(-\frac{u}{3})\,\tilde{I}(-\frac{u}{3}) \tag{3}$$

which is an expression related to the bispectrum[7] when it is evaluated at frequencies $u \rightarrow \frac{2}{3}u$, $v \rightarrow -\frac{1}{3}u$ or when $u \rightarrow -\frac{1}{3}u$, $v \rightarrow \frac{2}{3}u$, both solutions being representations of lines in the bispectrum u, v plane. It can also be seen that in the limiting case of $N \rightarrow \infty$ that $\tilde{Q}_N(u) \rightarrow \tilde{I}(u)$ as one would expected.

3 - OBJECT RETRIEVAL FROM ONE-DIMENSIONAL CENTROIDED IMAGES - $Q_N(r)$.

In Eq.(2) if one changes $u/N \rightarrow u$ and consider the case of real one dimensional intensity ($\tilde{I}(-u) = \tilde{I}^*(u)$) one has:

$$\tilde{Q}_N(Nu) = \tilde{I}([N-1]u) \quad \left[\tilde{I}^*(u)\right]^{N-1} \tag{4}$$

From Eq. (4) follows a recurrence relation linking phases of the object, ϕ, at the discrete frequencies k and $[N-1]k$ with the phase $\Theta_N(Nk)$ of the average quantity $\tilde{Q}_N(Nk)$:

$$\Theta_N(Nk) = \phi([N-1]k) - (N-1)\phi(k) \tag{5}$$

For $N = 2$ photons/frame $\Theta_2(2k) = \phi(k) - \phi(k) = 0$ and therefore no information about the phase can be retrieved. But for N=3 photons/frame Eq.(5) becomes:

$$\Theta_3(3k) = \phi(2k) - 2\,\phi(k) \tag{6}$$

and hence from phase at frequency k one can reconstruct the phase at 2k up to $3k \leq (\mathcal{L}/2)-1$ where $\mathcal{L}$ is the actual number of bins used to sample $Q_3(r)$.

The method can be better understood through an example in which a one dimensional image is sampled at 32 points and therefore $\tilde{Q}_N(Nk)$ is determined only at 32 frequency bins. Due to the fact that $\tilde{I}(-u) = \tilde{I}^*(u)$ one has to find the phases only in half the total number of bins and then reverse their sign. In this particular example one has, therefore, to consider only 16 frequency bins (Figure 1).

For k=0 the phase $\phi(0) = 0$. As $\tilde{Q}_N(Nk)$ is shift-invariant one can always determine $\tilde{I}(k)$ apart from a constant phase shifting factor. By appropriately choosing this factor one can always set the phase at $\phi(1) = 0$.

In general, for a frequency bin k, where k is a prime number, one can only reconstruct its phase by using an average $\tilde{Q}_N(Nk)$ such that N=k+1 photons per frame. In this particular example to reconstruct the phases up to bin 15 one needs averages of frames with N up to 16 photons per frame. The modulus of $\tilde{I}(k)$ is found from the Fourier transform of the auto-correlation function, the power spectrum $\left|\tilde{I}(u)\right|^2$.

Experiments were carried out using simulated one dimensional photon data emitted from the object shown in Fig. 2(a) and in the particular simulation experiment described in this paper, we set the Poisson distribution mean value $\overline{N} = 3$ photons/frame. Frames with 0 or 1 photons/frame are disregarded, because they do not carry any information concerning the intensity distribution of the image, and a total of 80,084 frames of a randomly translating image (of a binary star) containing $N \geq 3$ photons/frame were generated. These frames can be grouped in sets of frames containing a number of photons ranging from N=3 up to N=13 photons/frame in this case.

Figure 3 depicts $Q_N(\mathbf{r})$ for N=2 and N=3 photons/frame. For N=2 it can be seen that $Q_2(\mathbf{r})$ exhibits the same shape as the autocorrelation of the binary but distributed in a smaller region of space.

Figure 2(b) shows the reconstructed image obtained using this method with $\mathcal{L} = 128$ bins and using frames with N only up to 13 photons/frame i.e. not all the frequencies were reconstructed. Despite the fact that no other image processing technique has been used, e.g. enforcing positivity, Fig. 2(b), nevertheless, gives a good estimate of the image and in this particular case also a good estimate of the relative brightness of the stars.

4 - ACKNOWLEDGMENTS

LCF is funded by The British Council and CNPq - Brazil on leave from Departamento de Fisica - Univ. Fed. Mato Grosso do Sul - P.O. Box 649 - 79.100 - Campo Grande - MS - Brazil. The authors wishes to thank G. Ayers for providing the simulation program and also to acknowledge the contributions of M.J. Northcott and G. Ayers in the early stages of this work. The research was supported by the U.K. Science and Engineering Research Council - S.E.R.C. under grant GR/D 92332 and the U.S. Army under Contract DAJA 45-85-C-0028.

5 - REFERENCES

1 - C.R. Lynds, S.P. Worden and J.W. Harvey, Ap. J., 207, 174(1976).

2 - S.P. Worden, C.R. Lynds and J.W. Harvey, JOSA, 66, 1243(1976).

3 - R.H.T. Bates, M.O. Milner, G.I. Lund and A.D. Seagar, Opt. Comm., 26, 22(1978).

4 - R.H.T. Bates and F.M. Cady, Opt. Comm., 32, 365(1980).

5 - F.M. Cady and R.H.T. Bates, Opt. Lett., 5, 438(1980).

6 - L.C. de Freitas, M.J. Northcott, B.J. Brames and J.C. Dainty, Proc. SPIE, 828, 1987(in press).

7 - A.W. Lohmann, G. Weigelt and B. Wirnitzer, Appl. Opt., 22, 4028(1983).

Fig. 1 - Pictorial representation of the phase reconstruction algorithm for N=3 and N=4 photons/frame

Fig. 2 - (a) - Stationary Object Intensity; (b) - Reconstruction with N ranging from 3 up to 13 photons/frame

Fig. 3 - (a) - Centroided frames with N=2 photons/frame and (b) - Centroided frames with N=3 photons/frame

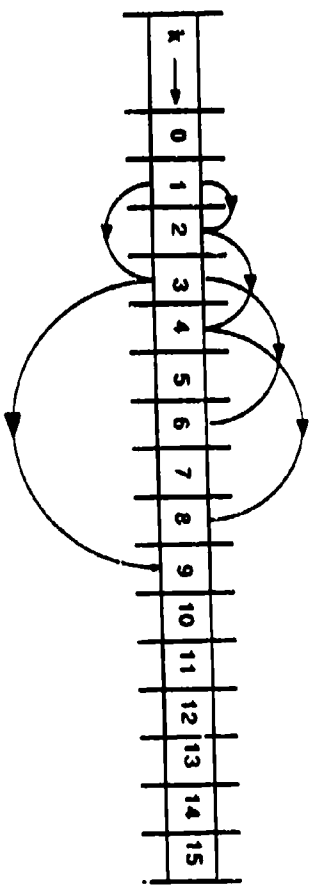
k
0
1
2
3
4
5
6
7
8
9
10
11
12
13
14
15

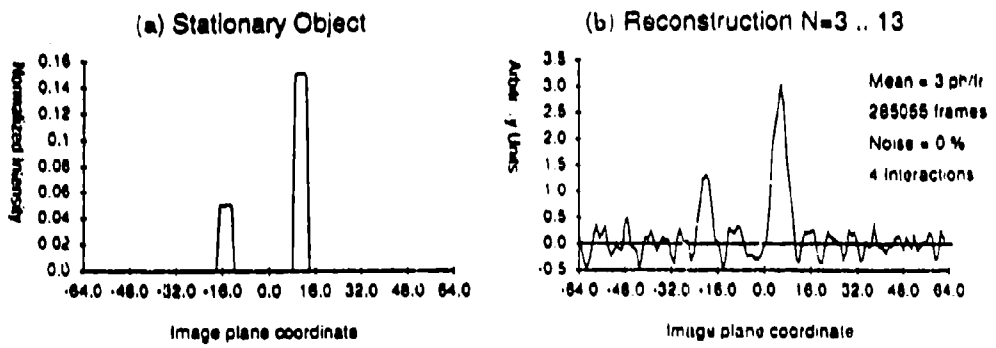
(a) Stationary Object
Normalized Intensity
0.16
0.14
0.12
0.1
0.08
0.06
0.04
0.02
0.0
-64.0 -48.0 -32.0 -16.0 0.0 16.0 32.0 48.0 64.0
Image plane coordinate
(b) Reconstruction N=3 .. 13
Angle / Lines
3.5
3.0
2.5
2.0
1.5
1.0
0.5
0.0
-0.5
-64.0 -48.0 -32.0 -16.0 0.0 16.0 32.0 48.0 64.0
Image plane coordinate
Mean = 3 ph/ir
265055 frames
Noise = 0 %
4 Interactions

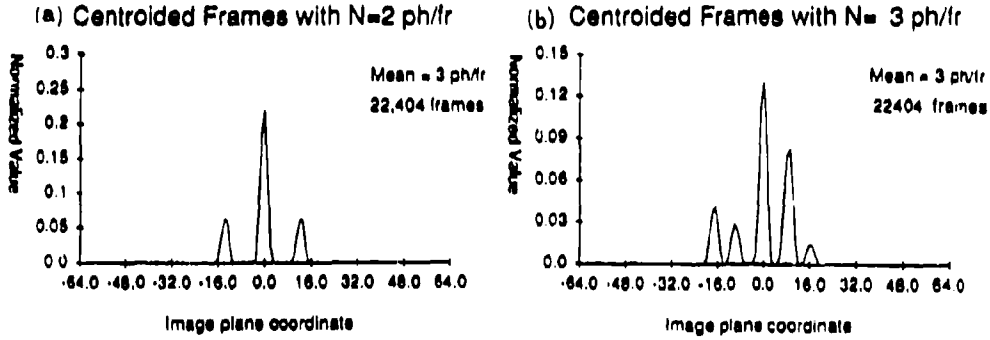
(a) Centroided Frames with N=2 ph/fr
Normalized Value
0.3
0.25
0.2
0.15
0.1
0.05
0.0
Mean = 3 ph/fr
22,404 frames
-64.0 -48.0 -32.0 -16.0 0.0 16.0 32.0 48.0 64.0
Image plane coordinate
(b) Centroided Frames with N= 3 ph/fr
Normalized Value
0.15
0.12
0.09
0.06
0.03
0.0
Mean = 3 ph/fr
22404 frames
-64.0 -48.0 -32.0 -16.0 0.0 16.0 32.0 48.0 64.0
Image plane coordinate